Transverse single spin asymmetries for the production of neutral pions in proton collisions at √s = 200 GeV

Poljak, Nikola

Transverse single spin asymmetries for the production of neutral pions in proton collisions at $\sqrt{s} = 200$ GeV

Nikola Poljak

A dissertation submitted in partial fulfillment of the requirements for the degree

Doctor of science

Department of physics
Faculty of sciences and mathematics
University of Zagreb, Croatia

November 29, 2010

BASIC DOCUMENTATION CARD

University of Zagreb
Faculty of Science
Physics Department

Dissertation

Transverse single spin asymmetries for the production of neutral pions in proton collisions at $\sqrt{s} = 200$ GeV

NIKOLA POLJAK
University of Zagreb
Faculty of Science, Physics Department
Bijenička 32, 10 000 Zagreb, Republic of Croatia

Dissertation contains:	179 pages, 102 pictures, 12 tables and 56 references
Original language:	English
Dissertation deposited:	Central library for physics, PMF, Croatia
Supervisors:	Prof.dr.sc. Mirko Planinić (PMF) Dr. Leslie Carlisle Bland (BNL)
Reviewers:	Dr.sc. Krešo Kadija (IRB) Prof.dr.sc. Mirko Planinić (PMF) Dr.sc. Leslie Carlisle Bland (BNL) Prof.dr.sc. Miroslav Furić (PMF) Prof.dr.sc. Ivica Picek (PMF)
Dissertation accepted:	Nov 29, 2010.

Dedicated to Maritere

Acknowledgments

It is a pleasure to thank those who made this thesis possible.

First and foremost, I would like to thank dr. Les Bland, who led me through the process of envisioning and building the experiment, as well as analyzing and interpreting the data it collected. Les always had an inexhaustible set of ideas that have shown me the way forward. Further, I owe my deepest gratitude to prof. Mirko Planinić, my supervisor at the University of Zagreb, who always helped me and motivated me with physical discussions.

I would also like to thank all the physicists who engaged actively in conversations regarding my work and helped a lot with their questions, comments and advice. This thanks goes to the STAR FMS group, most notably Akio Ogawa and Larisa Nogach, my group in Zagreb lead by prof. Miroslav Furić, and the entire STAR collaboration.

My parents and my family were a moral support during the work, who, although at times not understanding completely what I am doing, were always proud of me and were interested in every aspect of my work. Special thanks goes to my wife Maritere, who supported me during my graduate years in every possible way, enduring at times weeks filled only with my work. Throughout the years, she has always been pushing me forward and has given me her unconditional love.

At last, but by far not at least, my friends were always with me during times of leisure, providing always needed moral support and relaxation.

Thank you all.

These materials are based on work financed by the National Foundation for Science, Higher Education and Technological Development of the Republic of Croatia. Any opinions, findings, and conclusions or recommendations expressed in this material are those of the author(s) and do not necessarily reflect the views of The National Foundation for Science, Higher Education and Technological Development of the Republic of Croatia.

Abstract

The STAR collaboration has reported precision measurements on the transverse single spin asymmetries for the production of forward π^0 mesons from polarized proton collisions at $\sqrt{s} = 200\,\mathrm{GeV}$. To disentangle the contributions to forward asymmetries, one has to look beyond inclusive π^0 production to the production of forward jets or direct photons. Present forward detector capabilities are not well matched to the complete reconstruction of forward jets, but do have sufficient acceptance for "jet-like" events. "Jet-like" events are the clustered response of an electromagnetic calorimeter that is primarily sensitive to incident photons, electrons and positrons.

During the RHIC running in the year 2006, STAR with the Forward Pion Detector (FPD++) in place collected 6.8 pb^{-1} of data with an average polarization of 60%. FPD++ was a modular detector prototype of the Forward Meson Spectrometer (FMS) that consisted of two detectors placed symmetrically with respect to the beam line at a distance of 7.4 m from the interaction point. Readout of the FPD++ was triggered when the sum of energies in the central module of the calorimeter used for π^0 measurements was larger than a threshold. This trigger minimizes the bias for "jet-like" events, making it appropriate to disentangling contributions to the forward transverse spin asymmetries.

This thesis reports on the analysis, giving in specific detail all the calibration and analysis steps, as well as the final results. It has been demonstrated that the calibration procedures used earlier to calibrate the previous versions of the detector can be extended to the current setup. Results from earlier analyses were successfully reproduced and extended as well. It has been shown that the parts of the detector that were not used earlier have no systematic influence on the results. After the extraction of the "jet-like" events, their properties were carefully explored. The final result shows that the neutral pion asymmetry shows no dependence on the angle with respect to the "jet-like" event axis, thus showing that there is no net Collins contribution to the neutral pion asymmetries.

Contents

List of Figures

List of Tables

Chapter 1.

Introduction

Understanding the structure of the proton has been one of the goals of the physics community for over 50 years. To really understand it, one must also know how the proton constituents contribute to the overall proton spin of 1/2.

After the unpolarized deep inelastic scattering experiments (UDIS) have revealed the spatial structure of the proton, polarized deep inelastic scattering (PDIS) experiments tried to reveal its spin structure. These experiments [1, 2, 3] had shown that quarks and antiquarks account for only a small fraction of the entire spin of the proton ($\approx$ 20-30%). So, the remaining part has to come from either the gluons or the orbital motions of the proton constituents.

In unpolarized DIS experiments the probe of the proton is a lepton, typically an electron or a muon. In polarized DIS, both the lepton and the target proton are polarized. More generally, spin structure is addressed in polarized hard scattering experiments, that include a variety of probes where the scattering can be treated by perturbative QCD. So, experiments doing this research will also be pp experiments. The first greatly unexpected result from a polarized hard scattering experiment came from the Fermilab E704 experiment [4] where polarized protons were hitting a polarized fixed target. In this experiment, large values of analyzing power, defined as the difference of inclusive cross sections for a production of a particle divided by their sum, were observed for pion production at the center of mass energy of 20 GeV. The E704 experiment also measured A_{LL}, a longitudinal spin asymmetry

nominally sensitive to gluon polarization. Although their statistics were never that great, they found zero for A_{LL}.

The result of the E704 experiment did not at all agree with the naive perturbative Quantum Chromodynamical (pQCD) prediction, which claimed the asymmetry should be very small. Still, it was not clear whether this was a misprediction of the theory, since the energy and p_T (transverse momentum of the outgoing particle) range at which the experiment was done may not be within the kinematical range of the theory. After the results were published, several theories emerged in an attempt to explain the seen effect. Even though the mechanisms these theories propose greatly differ, as described later in the text, the net result they produce is the same for inclusive meson production.

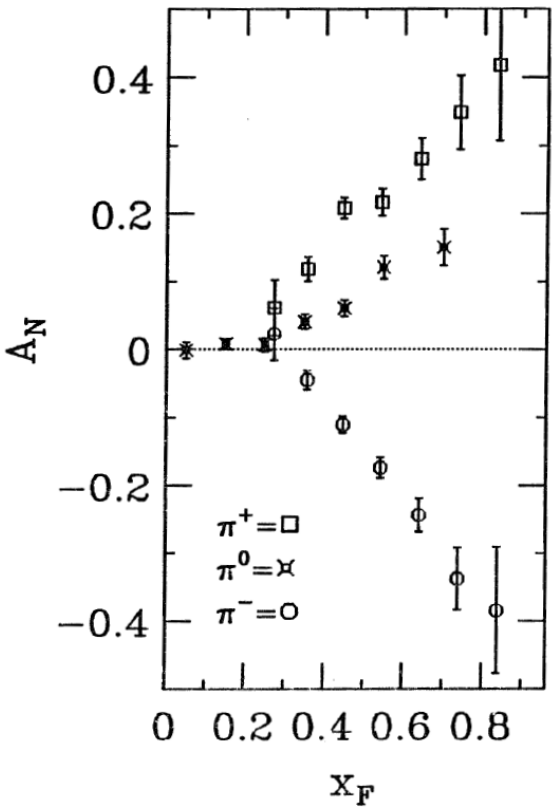

Figure 1.1: The FermiLab E704 experimental result. Shown on the plot are pions, both neutral and charged, produced at $\sqrt{s} = 20$ GeV at $p_T = 0.5 - 2.0$ GeV. A_N stands for single spin asymmetry, defined later in the text. [4]

Two steps were in place now: first one is to go to higher energy, where one can be sure of the pQCD predictions, and the other to try to differentiate the theories by means of experiments.

The first step was completed at RHIC at the center of mass energy of $\sqrt{s} = 200$ GeV. This experiment was the first to use polarized proton beams using a new magnet technology called "Siberian snakes" [5]. By using the proton beams, center of mass energy was substantially larger than in the previous experiments that used fixed polarized targets. Obtaining the polarized proton beam is not simple since protons are heavy particles. Lighter particles can develop their polarization due to Sokolov-Ternov effect [6], but the protons are not light and they will not develop practically any polarization in this way. Polarized protons, once prepared, have to be stored in the rings and their polarization has to be maintained. The "Siberian snakes" flip the polarization of protons, keeping them polarized in one direction half of the accelerator ring, and in the other direction the other half. In the experiment, at $\sqrt{s} = 200$ GeV, it has been shown that the invariant differential cross section for inclusive π^0 production is in agreement with the next to leading order (NLO) pQCD [7].

Further experiments were then conducted, at RHIC as well at many other sites, at both higher and lower energies. One of the most notable published results from RHIC came from a part of the detector this thesis aims to describe. This is a high precision result showing the single spin asymmetry of the neutral pions [8]. The experiment was also conducted at $\sqrt{s} = 200$ GeV, so one can claim that the underlying theory describing it is NLO pQCD. The result only confirms what has been seen earlier: a strong rise of the π^0 asymmetry with rising Feynman x (x_{F}); a quantity proportional with the forward momentum of the π^0. This is a clear and concrete proof of the existence of asymmetry at both lower and higher energies; the question remaining is its origin.

Further efforts were undertaken in both theory and experiment trying to explain single spin asymmetry. The effort to separate the two leading concurrent models, the Sivers effect [9, 10] and the Collins effect [11] is still on way. This thesis aims to partially resolve the question.

Chapter 2.

Theoretical background

Presented at the beginning of this chapter are the single spin asymmetry and its measurements. After that, I explain the definitions of quantities relevant to the following sections. For a general review, refer to [12]. After the definitions, the proton collisions in perturbative QCD will be described.

2.1. Single spin asymmetries and measurements

To start off with the definition of measurements, we will introduce a coordinate system and place the beam and the detector in it. Let the polarized proton beam come along the positive z axis. Since the polarization is transverse, the spin will point in what we will call $\pm y$ direction. The positive sign polarization is called "up" and the negative "down". The detector faces are perpendicular to the direction of the motion of the proton, and span their own $x - y$ systems. Another way of describing the system is by using cardinal directions. Putting the proton motion towards W (west), one detector will be N (north) relative to it, and one will be S (south) relative to it. The north detector is called "right" and the south "left", relative to the polarized beam with momentum $p_z > 0$.

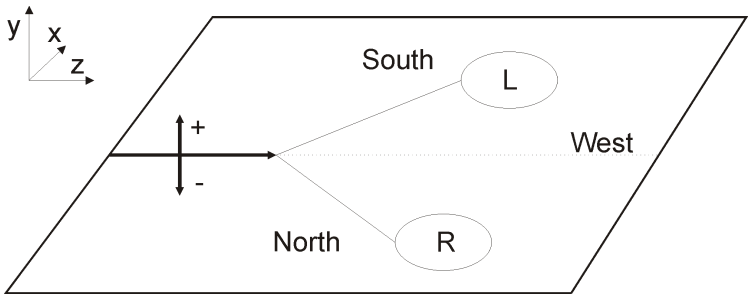

Figure 2.1: The schematic of the defined coordinate system.

2.1.1. Single spin asymmetry

The single spin asymmetry is defined in terms of "analyzing power", which is equal to:

$$A_{\mathrm{N}} = \frac{\sigma_+ - \sigma-}{\sigma_+ + \sigma_-}\,, \tag{2.1}$$

where the $\sigma_\pm$ are the cross sections for protons with spin up(down). "Cross section" is proportional to the rate of production of any specified particle, for example the pion or the eta meson. At this point, it is useful to define a polar coordinate system with the help of STAR coordinates. With the polarized proton coming along the positive z axis, θ is defined as the polar angle with respect to that axis, and ϕ as the azimuthal angle around the axis. For unpolarized collisions, inclusive particle production in general depends on θ, but must be independent of ϕ.

The single spin asymmetry ϵ is the product of the analyzing power A_{N} and the average polarization of the incoming beam $P_{\mathrm{av.}}$. In principle, ϵ can be measured by a single detector at a fixed θ relative to the transversely polarized beam, by counting the number of particles that hit it for spin up and spin down polarization states. A measurement with a single detector would give:

$$\epsilon = \frac{N_+/L_+ - N_-/L_-}{N_+/L_+ + N_-/L_-}\,. \tag{2.2}$$

Here, N stands for the number of detected particles and the factor of luminosity (L) is added since there may be different luminosities for the beam with polarization + vs. the beam with polarization -.

Now let's see why making a measurement with two detectors, places symmetrically around the beam, proves to be more useful. Let these detectors be called L and R, as in the convention described above. One thing to consider is that these detectors can not be perfectly equal, so they will have different acceptance factors and efficiencies. To each of them we have to assign a factor Ω describing that. Looking at the detectors separately, the asymmetry now becomes:

$$\epsilon = \frac{N_+^{L(R)}/(\Omega_{L(R)}L_+) - N_-^{L(R)}/(\Omega_{L(R)}L_-)}{N_+^{L(R)}/(\Omega_{L(R)}L_+) + N_-^{L(R)}/(\Omega_{L(R)}L_-)}\,. \tag{2.3}$$

Equation (2.3) is in fact two equations, one corresponding to the left detector (L) and one to the right detector (R). If we now consider rotational invariance, then it has to be true that $N_\mp^L/(\Omega_L L_\mp) = N_\pm^R/(\Omega_R L_\pm)$ and this equation can be reduced to:

$$\epsilon = \frac{N_+^L/\Omega_L - N_+^R/\Omega_R}{N_+^L/\Omega_L + N_+^R/\Omega_R} = \frac{N_-^R/\Omega_R - N_-^L/\Omega_L}{N_-^R/\Omega_R + N_-^L/\Omega_L}\,. \tag{2.4}$$

In this expression the luminosities cancel out so no error arising from the measurement of luminosity enters in the error of the result. It would be good if one could cancel out the acceptance and efficiency factors as well. If one looks at the last equation (which is actually a set of two equations) it becomes apparent that we can solve this set for the Ω factors and then place them back in the analyzing power, thus removing it from the expression. However, it turns out that these equations are linearly dependent and only one of the factors can be removed in this way. Still, there is a way to remove the other acceptance factor as well by forming a "cross ratio" asymmetry. This is the asymmetry defined by:

$$\epsilon' = \frac{\sqrt{N_+^L N_-^R} - \sqrt{N_-^L N_+^R}}{\sqrt{N_+^L N_-^R} + \sqrt{N_-^L N_+^R}}\,. \tag{2.5}$$

When calculated, this is exactly equal to ϵ. This asymmetry has two benefits; first, it removes the systematic error arising from the efficiency of the detectors, and second, it effectively doubles the number of events recorded (assuming the detectors record and approximately equal number or events) thus doubling the statistics.

A natural question arises at what angle with respect to the polarization vector should one place the detectors? The beam momentum vector and the detected particle momentum form a plane. It is only the component of the polarization vector that is perpendicular to this plane that can give rise to ϵ. Hence, to observe the largest asymmetry, the detectors are best placed in a plane that is perpendicular to the polarization vector.

2.1.2. Differential cross section

The measurement of the cross section, although not directly included in the asymmetry, is very important since it proves that one understands (or does not) the processes he is observing. The differential cross section for the initial state of two hadrons is explicitly equal to [13]:

$$\mathrm{d}\sigma(\alpha \to \beta) = (2\pi)^4 u^{-1} |\mathcal{M}|^2 \delta^4(p_\beta - p_\alpha)\mathrm{d}\beta\,. \tag{2.6}$$

Here, α is the set of two initial states (hadrons), β is the set of final states, u is the relative speed of the initial states and $\mathcal{M}$ is the transition amplitude from states α to states β. In the experiment, one can not directly measure these quantities, or even directly the cross section, but only deduce the collected energy or the number of reconstructed particles. This quantity should be directly proportional to the integrated luminosity of the delivered beam. One has to take into account many factors, which are summarized in this equation:

$$E\frac{\mathrm{d}^3\sigma}{\mathrm{d}\phi\mathrm{d}y p_T \mathrm{d}p_T} = \frac{1}{L}\frac{C_{\mathrm{rc.}} N_{\pi^0}}{f_{\pi^0}}\frac{1}{p_T^{\mathrm{av}\cdot}\Delta p_T \Delta\phi\Delta y}\,. \tag{2.7}$$

In this equation, L stands for delivered luminosity, $C_{\mathrm{rc.}}N_{\pi^0}$ is the number of reconstructed particles (here chosen to be pions), which also takes into account the factors for loss on reconstruction of particles, $p_T^{\mathrm{av}\cdot}$ is the value of p_T for which the cross section value equals its

average over the Δp_T bin, and $\Delta\phi$ and Δy are the acceptance factors of the detector (angle and rapidity). The rapidity, in our specific case, which is at high energies and small polar angles, is almost equal to the pseudorapidity.

2.2. Spin density matrix

The most important quantities we are dealing with in this work are spin and polarization. The polarization vector of a single free spin 1/2 particle of momentum $P^\mu = (P^0, \vec{P}) = (E, \vec{P})$ is given by:

$$s^\mu = \left(\frac{\lambda |P|}{m}, \frac{P_0 \lambda}{m|P|} \vec{P} + \vec{s}_\perp \right) . \tag{2.8}$$

λ is twice the helicity of a particle, so in the case of spin 1/2 particles, $\lambda = 1$, and $\vec{s}_\perp$ are the components of the spin vector perpendicular to the axis of movement of the particle.

The high energy limit, which we are mostly interested in, produces:

$$s^\mu = \lambda \frac{p^\mu}{m} + s^\mu_\perp \, , \tag{2.9}$$

A matrix that describes the spin structure of the system and is valid even when the system is not in a pure state, which is most often the case, is called the spin density matrix and is given by:

$$\rho = \frac{1}{2}(1 + \vec{\sigma} \cdot \vec{s}) = \frac{1}{2} \begin{pmatrix} 1 + s_z & s_x - i s_y \\ s_x + i s_y & 1 - s_z \end{pmatrix} , \tag{2.10}$$

where σ is the set of usual Pauli matrices.

2.3. Parton distribution functions (PDFs) - collinear case

Basically, parton distribution functions are functions that tell us how the quarks are distributed within a hadron in momentum space. In the case where the hadron constituents are assumed to move collinearly with the hadron, the probability of finding a quark with a certain fraction of longitudinal momentum x (regardless of polarization) in a hadron specified

with impulse and spin P and S is given by:

$$f(x) = \int \frac{d\zeta^-}{4\pi} \mathrm{e}^{iP^+x\zeta^-} < PS|\overline{\Psi}(0)\gamma^+\Psi(0,\zeta^-,0_\perp)|PS>, \tag{2.11}$$

which is a form of the more general formal expression for the quark distribution functions; the light-cone Fourier transformations of the connected matrix of certain quark field bilinears [14].

$$Tr(\Gamma\Phi) = \int \mathrm{d}^4\zeta \mathrm{e}^{ik\cdot\zeta} < PS|\overline{\Psi}(0)\Gamma\Psi(\zeta)|PS> . \tag{2.12}$$

In these equations γ and Γ are general operators involving products of Dirac matrices, specific to the observable of interest. There are only two Lorentz vectors describing each state denoted by Ψ, the momentum of the hadron P and S, where S stands for the spin of the hadron. One might think that the quark momenta are independent of these quantities, but in the collinear model, their momenta are proportional to the hadron momentum P, since they move in the same direction as the hadron. Two more distributions can be inferred from the previous relation that are useful for this thesis:

$$\Delta f(x) = \int \frac{d\zeta^-}{4\pi} \mathrm{e}^{iP^+x\zeta^-} < PS|\overline{\Psi}(0)\gamma^+\gamma_5\Psi(0,\zeta^-,0_\perp)|PS>, \tag{2.13}$$

$$\Delta_T f(x) = \int \frac{d\zeta^-}{4\pi} \mathrm{e}^{iP^+x\zeta^-} < PS|\overline{\Psi}(0)\gamma^+\gamma^1\gamma_5\Psi(0,\zeta^-,0_\perp)|PS>, \tag{2.14}$$

Δf is the difference between the number density of quarks with helicites + and -, and $\Delta_T f$ is the difference of number densities of quarks with polarization $\uparrow$ and polarization $\downarrow$ when the parent hadron has an $\uparrow$ polarization. These will be closely connected to the spin asymmetries.

2.4. PDFs - beyond the collinear case

Going beyond the collinear terms, one can add transverse motion to the quarks. Now the quark momentum is not just proportional to hadron momentum, but becomes:

$$k^\mu = xP^\mu + k_\perp^\mu \,, \tag{2.15}$$

where $k_\perp^\mu$ is the added transverse momentum of the quarks. A very illustrative way to imagine this is figure 2.2. On the left is a simple proton model with three valence quarks, whereas on the right there is a more realistic model including valence quarks, some sea quarks, gluons and orbital momenta of the quarks. In this case there are three independent 4-vectors: the hadron momentum P, the transverse quark momenta $k_\perp$ and the spin S. For a transversely polarized hadron, P is perpendicular both to $k_\perp$ and S, which make a 2D basis of their own. With the hadron momentum placed in the z direction, one can define angle between the other two vectors to be $\phi_k - \phi_S$. This is depicted in figure 2.3.

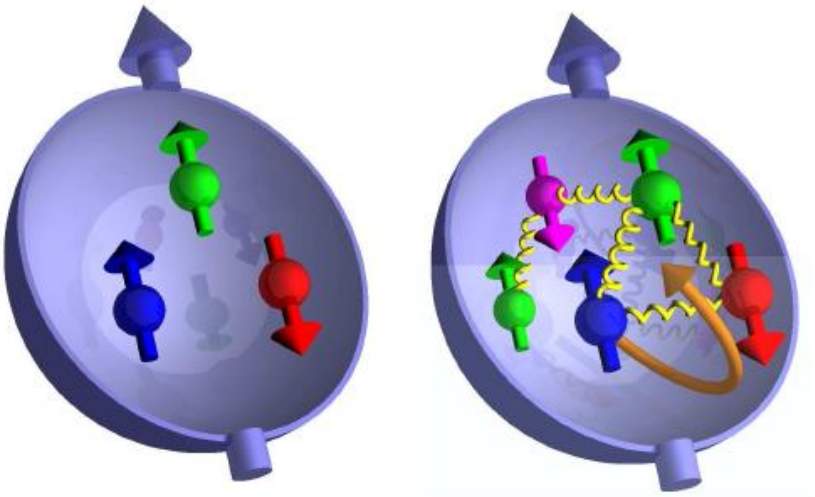

Figure 2.2: Schematic view of the proton in a simple model and a more general model. On the left is a simple proton model with three valence quarks, whereas on the right there a more realistic model including valence quarks, some sea quarks, gluons and orbital momenta of the quarks.

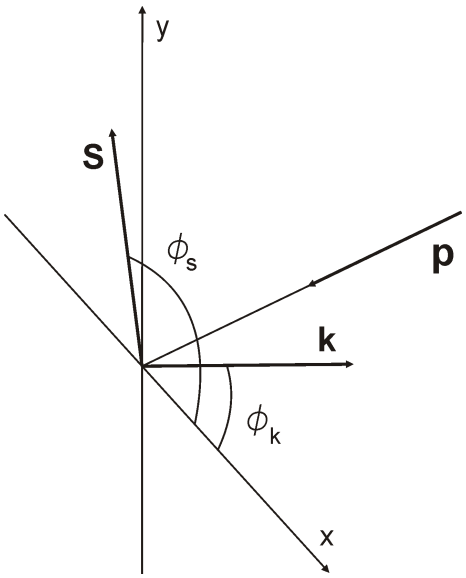

Figure 2.3: Definition of the azimuthal angles for the non-collinear case.

The probability distributions that were written down in the collinear case now have to be modified by the inclusion of the perpendicular quark momenta. Without going into details of all the distributions, the one important to this work is the one connected to the asymmetry in the $\uparrow$ vs. $\downarrow$ polarized hadron. This is equal to:

$$f_{qN\uparrow}(x,k_\perp) - f_{qN\downarrow}(x,k_\perp) = f_{qN\uparrow}(x,k_\perp) - f_{qN\uparrow}(x,-k_\perp) = \Delta_0^T f(x,k_\perp^2)\sin(\phi_k - \phi_S)\,. \quad (2.16)$$

In this notation, $\Delta_0^T f(x,k_\perp^2)$ is directly related to the number density of unpolarized quarks in a polarized nucleon.

2.5. Twist expansion

To get non-zero single spin asymmetries, one can either take into account the transverse motion of quarks inside hadrons, or consider what are called higher twist terms. "Twist" of an operator is defined by its "mass dimension"-"Lorentz spin" [15]. Since the matrix element relevant to collision of hadrons contains an operator product, one can make the usual operator product expansion (OPE). Normally ordered operators in such an expansion can be classified in more than one way, and classifying them by twist proves useful. So, the utility of twist lies in finding the dominant contributions of operators to specific observables.

One can produce higher twist terms, for example, by including a gluon interaction in the quark correlation matrix. Schematically, one can draw the leading twist case and this case (called twist-3) with the help of a diagram, such as figure 2.4.

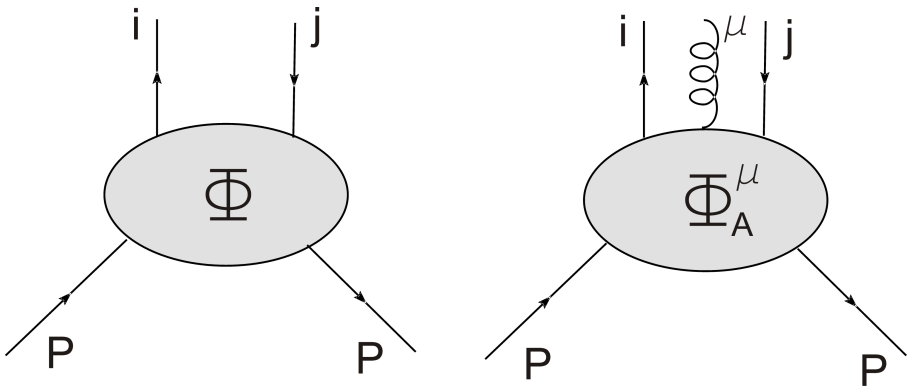

Figure 2.4: The correlation matrices for the leading twist and the twist-3 case. The twist-3 case, as can be seen, holds an interaction with a gluon.

The probabilistic distribution function now changes and is connected to:

$$F(k,k',P,S) = \int \mathrm{d}^4\zeta \int \mathrm{d}^4 z \mathrm{e}^{ik'\cdot\zeta}\mathrm{e}^{i(k-k')\cdot z} < PS|\overline{\phi}_j(0)gA(z)\phi_i(\zeta)|PS> \ . \tag{2.17}$$

2.6. Fragmentation functions

Just as the distribution functions were correlated to the quark correlation matrix, the fragmentation functions are correlated to the decay matrix:

$$Tr[\Gamma\Xi] = \sum_X \int \mathrm{d}^4\zeta \mathrm{e}^{ik\cdot\zeta} Tr < 0|\Psi_i(\zeta)|P_h S_h, X >< P_h S_H, X|\overline{\Psi}_f(0)\Gamma|0 > \ . \tag{2.18}$$

Also, just like in the distribution functions, one can define three leading-twist fragmentation functions. Introducing intrinsic transverse momentum in the produced hadron, one can reach an expression similar to the one in the last section:

$$\mathcal{N}_{hq\uparrow}(z,\kappa_T) - \mathcal{N}_{hq\downarrow}(z,\kappa_T) = z\Delta_T^0(z,\kappa_\perp^2)\sin(\phi_\kappa - \phi_{s'})\,. \tag{2.19}$$

In this equation $\mathcal{N}_{hq\uparrow,\downarrow}$ stand for fragmentation functions of a quark polarized in $\uparrow$ or $\downarrow$ direction fragmenting into a hadron h and z is the momentum fraction of the hadron in the quark. Here, again, three independent vectors form a basis: the produced hadron momentum P_h, the quark momentum κ and its polarization s'. The angular factor is defined through a new quantity, the Collins angle:

$$\sin(\phi_\kappa - \phi_{s'}) \equiv \sin(\phi_C) = \frac{(\kappa \times P_h)\cdot s'}{|\kappa \times P_h||s'|}\,. \tag{2.20}$$

This is the azimuthal angle between the spin vector of the fragmenting quark and the momentum of the produced hadron.

2.7. Collision of protons in perturbative QCD

One of the components of the Standard Model is Quantum Chromodynamics, the components of which are the building blocks of protons. Some of the fascinating features of QCD are confinement and asymptotic freedom. This is directly related to the coupling constant of QCD, α_{strong}, which becomes larger at smaller energies, thus confining quarks and gluons

(partons) into hadrons, and smaller at higher energies, making the particles close to each other virtually free of interaction. So, just as in Quantum Electrodynamics (QED), at higher energies in QCD, one can make perturbative expansions and claim it is a good approximation of reality. The question one should ask is what is the exact energy where you can make such a claim?

In the experiment, due to confinement, one actually collides hadrons, and not quarks or gluons. The final states of elementary interactions between quarks and gluons will eventually have to fragment into hadrons, and this is a process that can not be described well perturbatively. Due to the fact that at high energies the particles are virtually interaction free, a QCD factorization theorem may be applicable (eq. 2.21). This is a claim that states that our measurement will be a convolution of three parts:

- parton distribution functions for the particles in the initial state $f(x)$,
- hard scattering cross sections for partons in the elementary q-q, q-g and g-g processes, which can be described perturbatively and
- fragmentation functions F, which describe how partons fragment into final state hadrons.

So, a differential cross section for a collision of two partons "a" and "b" into a parton "c" that fragments into a hadron "h" can be written as:

$$\mathrm{d}\sigma = \sum_{\mathrm{abc}} f_{\mathrm{a}}(x_{\mathrm{a}}) \otimes f_{\mathrm{b}}(x_{\mathrm{b}}) \otimes \mathrm{d}\sigma_{\mathrm{part.}} \otimes F_{c\to h}\,. \tag{2.21}$$

Here x denotes the Bjorken x, representing the fraction of proton momenta carried by partons a,b into the hard scattering. The partonic cross section is given by:

$$\frac{\mathrm{d}\sigma}{\mathrm{d}t} = \frac{1}{32\pi^2 s^2}\mathcal{M}_{\mathrm{abcd}}\mathcal{M}^*_{\mathrm{abcd}}\,, \tag{2.22}$$

with $\mathcal{M}_{\mathrm{abcd}}$ being the amplitude of the elementary ab $\to$ cd process. Factorization theorems, such as equation (2.22), have been proven for "collinear QCD" at leading twist. However, for the production of hadrons by proton collisions, there is no proof of factorization when using

transverse momentum dependent distribution or fragmentation functions. Factorization, and hence the possibility of universality of transverse momentum dependent distribution functions for calculation of the production of hadrons, appears to be broken because there is no clean separation of "soft" and "hard" processes. So, equation (2.21) is a model statement that has had phenomenological success in the interrelation of results from SIDIS with inclusive pion measurements at RHIC, but remains unproven. The work by Collins, Soper and Sterman [16] is a proof of factorization for transverse momentum dependent distribution functions for the Drell-Yan process. The key difference between Drell-Yan and the production of hadrons is whether color charge is in the hard-scattering final state. For Drell-Yan, there is no color charge in the hard-scattering final state.

A view of two protons colliding and an elementary quark-gluon scattering process, alongside with fragmentation is illustrated on figure 2.5.

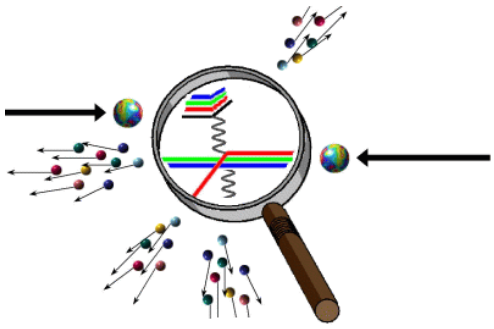

Figure 2.5: Schematic view of a quark-gluon collision from within two protons. Also visible is the fragmentation process of the scattered partons into hadrons. The colored lines represent quarks and the black lines the force mediators.

Two jets produced directly from the quark gluon scattering, which carry momenta $x_q P$ and $x_g P$ of the parent nucleon are usually described by variables suitable for the detector system: the pseudorapidity ($\eta = -\ln(\tan(\theta/2))$) and the transverse momentum p_T. Here, θ stands for the polar angle with respect to the interaction point when the beam line is placed in z direction. Based purely on kinematical factors and assuming the collision is collinear and elastic, it follows due to conservation of momentum that $p_{t1} = p_{t2} = p_T$. It then follows

that the fractions of the momenta carried by the quark and the gluon are:

$$x_q = \frac{p_T}{\sqrt{s}}(\mathrm{e}^{\eta_1} + \mathrm{e}^{\eta_1})\,,$$

$$x_g = \frac{p_T}{\sqrt{s}}(\mathrm{e}^{-\eta_1} + \mathrm{e}^{-\eta_1})\,. \tag{2.23}$$

Obviously, these numbers have a completely different behavior for different regions of pseudorapidity. Naturally, the model is not so simple, and one can find exact calculations for the NLO case scattering regime [17, 18]. Still, for the region of interest to this work, which is large η for the neutral pion production, x_g will go to zero, while x_q will be large. The dominant sources of pion production, which is of great importance to us, are primarily

$$q + g \to q + g(2 \to 2) \to \pi^0 + X\,,$$

$$q + g \to q + g + g(2 \to 3) \to \pi^0 + X\,. \tag{2.24}$$

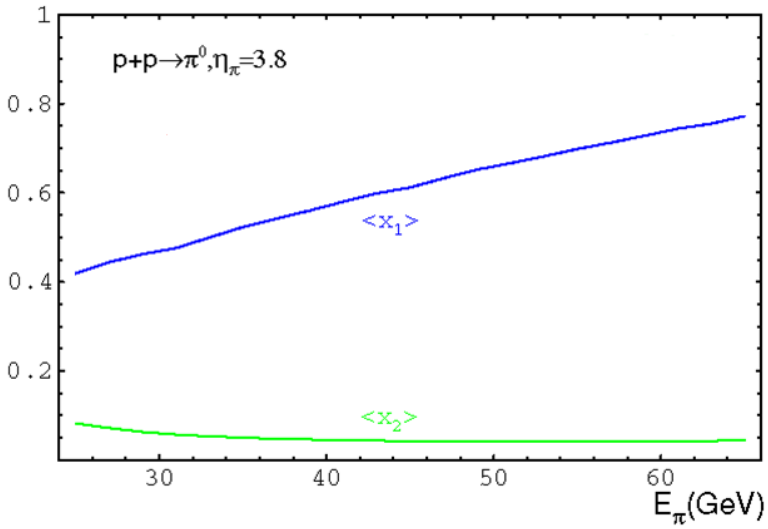

Figure 2.6: The dependence of Feynman x for the quark and gluon at high pseudorapidity vs. the produced pion energy. In this figure the quark is denoted by "1" and the gluon by "2". Figure is a portion of a plot from [19].

Looking at figure 2.6, one can see that at high pseudorapidities one will mostly see results of collisions of valence quarks (high x) and sea gluons (low x). This has a twofold advantage: first, the polarization of the quark will be high since the valence quarks carry most of the proton polarization, and second, the cross section will be large due to the large number density of gluons at low x.

Formally adding polarization in the initial state, things have to be rewritten with extra indices allowing for initial and final polarizations:

$$\mathrm{d}\sigma = \sum_{\mathrm{abc}} \sum_{\alpha\alpha'\beta\beta'} \rho^{\mathrm{a}}_{\alpha\alpha'} f_{\mathrm{a}}(x_{\mathrm{a}}) \otimes f_{\mathrm{b}}(x_{\mathrm{b}}) \otimes \mathrm{d}\sigma_{\alpha\alpha'\beta\beta'} \otimes F^{\beta\beta'}_{c\to h} \,. \tag{2.25}$$

Compare this with equation (2.21). Here, the indices α and β refer to the helicity of the initial (final) state and ρ stands for the spin density matrix of parton "a". The partonic cross section is now equal to:

$$\left(\frac{\mathrm{d}\sigma}{\mathrm{d}t}\right)_{\alpha\alpha'\beta\beta'} = \frac{1}{32\pi^2 s^2} \sum_{\gamma\delta} \mathcal{M}_{\alpha\gamma\delta\beta} \mathcal{M}^*_{\alpha'\gamma\delta\beta'} \,. \tag{2.26}$$

If the produced hadron turns out to be unpolarized, the collinear case expectation is that the factor $F^{\beta\beta'}_{c\to h}$ is diagonal, i.e. $\beta = \beta'$, so $F^{\beta\beta'}_{c\to h}$ is equal to $F_{c\to h}$ from the unpolarized case. If one adds the helicity conservation in all the partonic subprocesses, it turns out that there is no spin dependence on the spin of the initially polarized hadron and any spin asymmetry would be exactly equal to zero. Spin observables such as single spin asymmetry could be present, but very small due to the fact they would be suppressed by a factor of $\alpha m_q / p_T$, where α is the strong force coupling constant and m_q is the mass of a quark. So, if one gets results that are larger than this, one should look beyond the collinear terms in the leading twist.

2.8. Collisions of protons with TMD distributions

To produce single spin asymmetries, one can either add transverse motion of partons inside hadrons [20] or consider higher twist terms [21, 22, 23, 24, 25]. Taking into account transverse motion of quarks inside hadrons, a factorized expression for the cross section can be written as:

$$E_{\mathrm{h}}\frac{\mathrm{d}^3\sigma}{\mathrm{d}^3P_{\mathrm{h}}} = \sum_{abc}\sum_{\alpha\alpha'\beta\beta'\gamma\gamma'}\int \mathrm{d}x_{\mathrm{a}}\int \mathrm{d}x_{\mathrm{b}}\int \mathrm{d}^2k_{\mathrm{T}}\int \mathrm{d}^2k'_{\mathrm{T}}\int \mathrm{d}^2\kappa_{\mathrm{T}}$$

$$\frac{1}{\pi z}\otimes \mathcal{P}_{\mathrm{a}}(x_{\mathrm{a}},k_{\mathrm{T}})\rho^{\mathrm{a}}_{\alpha\alpha'}\otimes \mathcal{P}_{\mathrm{b}}(x_{\mathrm{b}},k'_{\mathrm{T}})\rho^{\mathrm{b}}_{\beta\beta'}\otimes\left(\frac{\mathrm{d}\sigma}{\mathrm{d}t}\right)_{\alpha\alpha'\beta\beta'\gamma\gamma'}\otimes F^{\gamma\gamma'}_{c\to h}(z,\kappa_T)\,. \tag{2.27}$$

Here, E_{h} and P_{h} stand for the energy and the momentum of the hadron. Alongside the usual indices, transverse variables, denoted by T, have been introduced, referring to intrinsic transverse momentum of partons in hadrons (k_T,k'_T) or of the hadron relative to the fragmenting quarks (κ_T). The functions $\mathcal{P}$ are generalized spin density matrices (called ρ in the leading twist case) that can contain transverse momentum dependence. Finally, a new spin index γ was added allowing for the difference in spin of the produced hadron with respect the colliding partons. The following two models taking into account the transverse motion are described here:

1. The Sivers effect [9].

   This model allows for the intrinsic transverse motion of the quarks in one of the mother hadrons. The equation for the differential cross section (omitting product signs) turns into:

   $$E_{\mathrm{h}}\frac{\mathrm{d}^3\sigma}{\mathrm{d}^3P_{\mathrm{h}}} = \sum_{abc}\sum_{\alpha\alpha'\gamma\gamma'}\int \mathrm{d}x_{\mathrm{a}}\int \mathrm{d}x_{\mathrm{b}}\int \frac{\mathrm{d}^2k_{\mathrm{T}}}{\pi z}\mathcal{P}_{\mathrm{a}}(x_{\mathrm{a}},k_{\mathrm{T}})\rho^{\mathrm{a}}_{\alpha\alpha'}f_b(x_b)\left(\frac{\mathrm{d}\sigma}{\mathrm{d}t}\right)_{\alpha\alpha'\gamma\gamma'}F_{c\to h}(z)\,. \tag{2.28}$$

   Compare this with equation (2.27). From definition of our measurement, one can see that we are mostly interested in the difference of cross section with the hadron having spin $\uparrow$ vs. it having the spin $\downarrow$. This will be equal to difference of the cross section written above for the case when the hadron has spin S_T and spin $-S_T$. One can show

[26, 27, 28] that eq. (2.28) reduces to:

$$E_{\mathrm{h}}\frac{\mathrm{d}^3(\sigma(S_T)-\sigma(-S_T))}{d^3P_{\mathrm{h}}}=$$

$$|S_T|\sum_{abc}\int \mathrm{d}x_a\int \mathrm{d}x_b\int \frac{\mathrm{d}^2k_T}{\pi z}\Delta_0^T f_a(x_a,k_T^2)f_b(x_b)\frac{\mathrm{d}\sigma}{\mathrm{d}t}(x_a,x_b,k_T)F_{c\to h}(z) \tag{2.29}$$

So, the Sivers effect relies on the T-odd Δ_0^T distribution (defined earlier in the text) to give rise to the asymmetry. The kinematical variables relevant to the Sivers effect are given on figure 2.7.

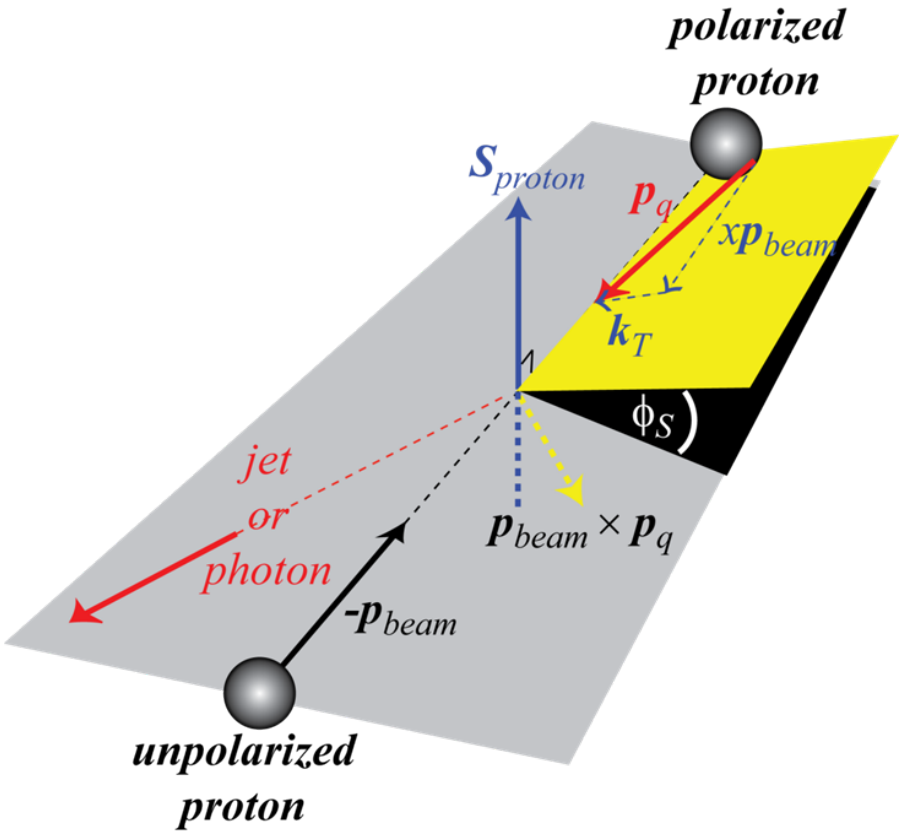

Figure 2.7: The schematic view of the Sivers variables. The Sivers angle, given earlier in the text, is the angle the quark impulse closes with the hadron collision plane perpendicular to the spin of the proton.

2. The Collins effect [11].

   Here, intrinsic transverse motion of the produced hadron h is considered, while the transverse momenta of quarks in the initial state are considered to be zero. The equation for the cross section becomes:

$$E_{\mathrm{h}}\frac{\mathrm{d}^3\sigma}{\mathrm{d}^3P_{\mathrm{h}}} = \sum_{abc}\sum_{\alpha\alpha'\gamma\gamma'}\int \mathrm{d}x_{\mathrm{a}}\int \mathrm{d}x_{\mathrm{b}}\int \frac{\mathrm{d}^2\kappa_{\mathrm{T}}}{\pi z} f_{\mathrm{a}}(x_{\mathrm{a}})\rho^{\mathrm{a}}_{\alpha\alpha'} f_{\mathrm{b}}(x_{\mathrm{b}})\left(\frac{\mathrm{d}\sigma}{\mathrm{d}t}\right)_{\alpha\alpha'\gamma\gamma'} F^{\gamma\gamma'}_{c\to h}(z,\kappa_T)\,. \tag{2.30}$$

   Compare this equation to (2.28). Just as in the previous case, the quantity of interest is the difference of cross sections for mother hadron having spin S_T vs. spin $-S_T$. Again, similar to the previous case, this reduces to:

$$E_{\mathrm{h}}\frac{\mathrm{d}^3(\sigma(S_T)-\sigma(-S_T))}{d^3P_{\mathrm{h}}} =$$

$$-2|S_T|\sum_{abc}\int \mathrm{d}x_a\int \mathrm{d}x_b\int \frac{\mathrm{d}^2\kappa_T}{\pi z}\Delta_T f_a(x_a) f_b(x_b)\Delta\sigma\Delta^0_T F_{c\to h}(z,\kappa_T^2)\,. \tag{2.31}$$

   Here, the still undefined quantity is:

$$\Delta\sigma = \left(\frac{\mathrm{d}\sigma}{\mathrm{d}t}\right)_{+-+-}\sin(\phi_k+\phi_s) + \left(\frac{\mathrm{d}\sigma}{\mathrm{d}t}\right)_{+--+}\sin(\phi_k-\phi_s)\,. \tag{2.32}$$

   This factor arises from the following fact: since the motions of quarks inside the mother hadrons are neglected, the spin density matrix elements contributing to the asymmetry section are only the off diagonal terms in the spin density matrix (++ and – don't give any asymmetry). So, the contributing cross sections are $\mathrm{d}\sigma_x$, where $x = (+-+-, -+-+, +--+, -++-)$. Further, the first two and the second two are equal, which leaves only the two mentioned in the formula. Further, if one knows the direction of the spin of the mother hadron, ϕ_s is immediately known (here set to $\pi/2$), and the equation simplifies even more:

$$E_{\mathrm{h}}\frac{\mathrm{d}^3(\sigma(S_T)-\sigma(-S_T))}{d^3P_{\mathrm{h}}} =$$

$$-2|S_T|\sum_{abc}\int \mathrm{d}x_a \int \mathrm{d}x_b \int \frac{\mathrm{d}^2\kappa_T}{\pi z}\Delta_T f_a(x_a) f_b(x_b)\Delta_{\mathrm{TT}}\sigma(x_a, x_b, \kappa_T)\cos\phi_k \Delta_T^0 F_{c\to h}(z, \kappa_T^2)\,. \tag{2.33}$$

The cross section factor in terms of partons is equal to:

$$\Delta_{TT}\sigma = \frac{\mathrm{d}\sigma(a^\uparrow b \to c^\uparrow d) - \sigma(a^\uparrow b \to c^\downarrow d)}{\mathrm{d}t}\,. \tag{2.34}$$

The Collins effect relies on the T-odd fragmentation function to give rise to the asymmetry. This is the key difference between the two effects that gives the possibility to separate them. The schematic view of the Collins variables is give on figure 2.8.

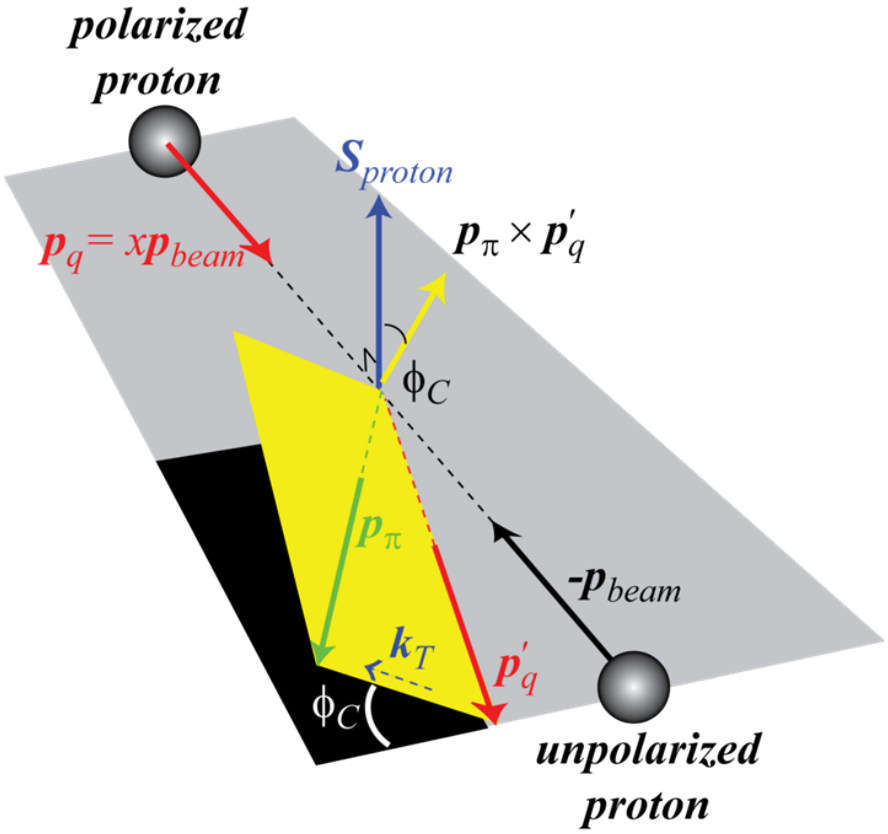

Figure 2.8: The schematic view of the Collins variables. The Collins angle is seen to be the angle the outgoing particle closes with the hadron collision plane perpendicular to the spin of the proton.

Finally, one can make an extension beyond leading twist not by including transverse motion, but adding a gluon to the quark correlation matrix. This case is known as the twist-3 case. This can be investigated in [21, 22, 23, 24, 25]. In principle, the twist-3 cross section is rewritten with the inclusion of the gluon term and a twist-3 fragmentation function is defined. There are three important terms in this new expression, the initial state twist-3 effect, the transversity dependent term and the final state twist-3 effect. It turns out that the transversity dependent term is negligible [25] and that the first and the third term can give rise to the asymmetries. In fact, it is proven that moments of transverse momentum dependent distribution functions (specifically the Sivers function) are interrelated with the matrix elements of the quark-gluon correlators [29]. Also, there are other possibilities for structure functions and fragmentation functions that can give rise to the asymmetries. The field is large, and a nice experimental and theoretical overview can be found in [30].

Chapter 3.

Experiment

3.1. Relativistic heavy ion collider

The Relativistic Heavy Ion Collider (RHIC) [5] is a part of the Brookhaven National Laboratory (BNL) located in Upton, New York. RHIC can essentially accelerate and collide all positive ions. It is an accelerator with two-fold purpose; one is to collide polarized proton beams with variable center of mass energy (currently up to 500 GeV), the other to collide heavy ions, like copper or gold. The second mode is intended for research of phenomena such as the quark gluon plasma (QGP), which is a high temperature, high density quantum chromodynamic phase. This mode of research goes beyond the scope of this thesis and will not be discussed here.

The design parameters of the polarized proton-proton (pp) mode are the luminosity of 2×10^{32} $\mathrm{cm}^{-2}\mathrm{s}^{-1}$ at center of mass energy of 500 GeV with the polarization of 70%. The goal of this mode of running is primarily to understand the origin and the behavior of the proton spin. The actual parameters that RHIC is running with change on a yearly basis and will be given later. The layout of the RHIC detector is given in figure 3.1.

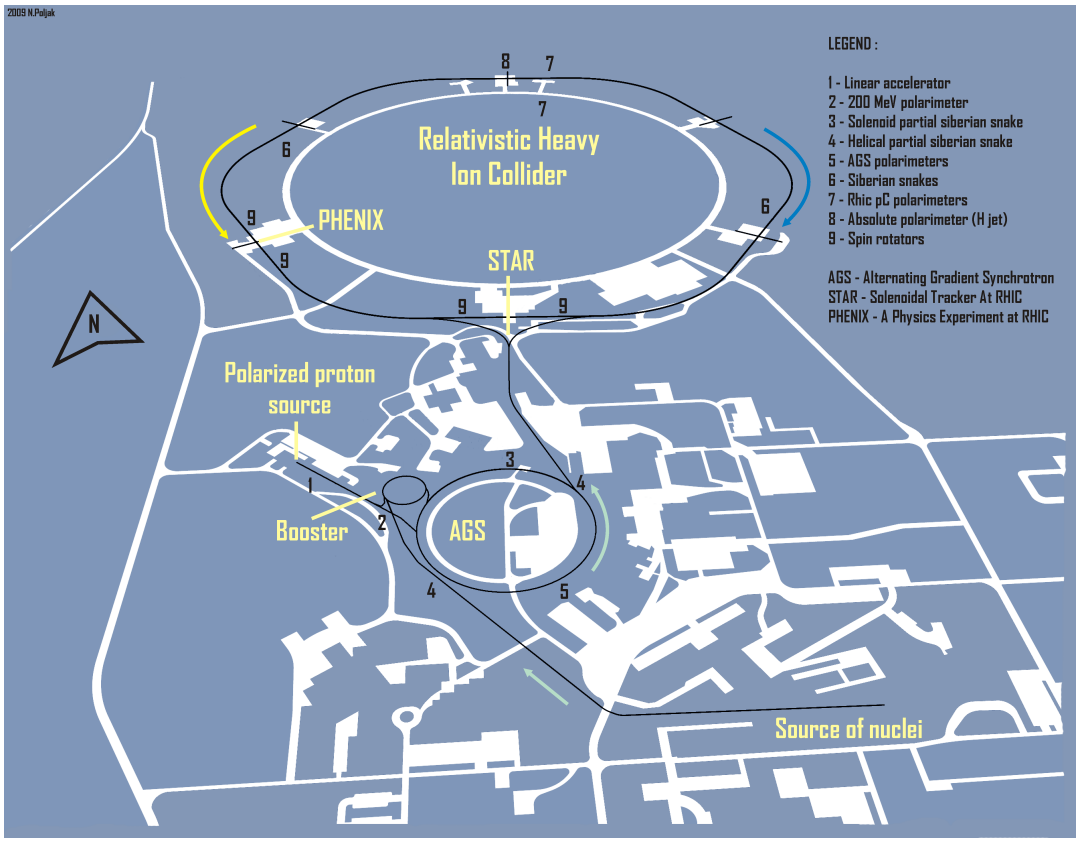

Figure 3.1: The Relativistic heavy ion collider layout. The blind map on the figure shows in white the location of supporting facilities needed to operate the collider. The black line represents the path of the accelerated particles.

3.2. An overview of RHIC pp Runs

The construction of the RHIC began in 1991 after a proposal made in 1984. It was a significant upgrade to an already existing accelerator at BNL, the Alternating Gradient Synchrotron. The new collider was built in part in an already existing tunnel dug to hold the ISABELLE collider. This project got cancelled since the magnets for it could not be produced. It then became the RHIC project. First operations began in 2001 by colliding gold ions. The same year a test run of polarized protons was done at particle energies of 24.3 GeV and 25.1 GeV. [31] A year after that, called Run 2, collisions of polarized protons at the particle energy of 100 GeV first took place. This thesis in particular deals with data

from Run 6, details of which will be specified later. Throughout the Runs, RHIC increased both the luminosity of the beam, as well as its average polarization. [32, 33, 34, 35, 36] In the table, FOM stands for Figure of Merit, which is a number that is equal to P^2L, where P is the average polarization over all Run segments and L is the integrated luminosity delivered to a detector. This number gives a measure of how useful the dataset is. One can see improvements in the FOM when we go from Run 2 to Run 6.

Run	$\sqrt{s}$ [GeV]	$L_{\text{int.}}$ at STAR [pb^{-1}]	Av. polarization (%)	100 ×FOM
Run 1	200	0.15	15	0.3
Run 2	200	0.15	15	0.3
Run 3	200	0.25	30	2.3
Run 5	200	0.1	45-50	2.5
Run 6	200	6.8	60	244.8
Run 8	200	7.8	50-55	235.9

Table 3.1: Operational parameters of the RHIC pp Runs. $\sqrt{s}$ stands for the center of mass energy and $L_{\text{int.}}$ the delivered integrated luminosity to the STAR detector.

3.3. The polarized proton beam

The RHIC tunnel is made up of two 3833 m long rings, approximately circular in shape, with six crossing point called interaction points (IPs). Two main interaction points hold detectors called Solenoidal Tracker at RHIC (STAR) and A Physics Experiment at RHIC (PHENIX), as drawn on the blind map. The two rings are called "Yellow" and "Blue" and the beam circulates counterclockwise in the Yellow ring and clockwise in the Blue ring. Figure 3.1 on the previous page shows the location of the STAR (Solenoidal Tracker at RHIC) detector.

The beam path of the polarized protons is as follows. In the OPPIS (Optically pumped polarized ion source) [37] protons are passed through an optically pumped alkali-metal vapor where they capture polarized electrons. In a weak magnetic field the protons themselves become polarized by interacting with the already polarized electrons. Finally, they are once again passed through the alkali-metal vapor to catch another electron and become H^- ions. The final result is 500 μA current of polarized ions in a 300 μs pulse.

The pulse is then accelerated to the energy of 200 MeV by a 200 MHz Linear Accelerator (LINAC) and focused by a Radio Frequency Quadrupole (RFQ) magnet. After there is no more need to keep the ions, they are stripped of their electrons and fed in the Alternating Gradient Synchrotron (AGS) booster. The stripping of the electrons from H^- ions is done at the injection point to the Booster synchrotron by a carbon foil. "Stripping injection" is a method of filling the Booster synchrotron, and is why H^- ions are required from OPPIS. The "RF injection" (so-called "bucket-to-bucket" transfers) is how beam is injected into the AGS and then transferred into the RHIC rings. In the AGS booster the beam reaches the energy of 2.465 GeV/proton. Continuing from the booster, the beam enters the AGS and is further accelerated to 24.3 GeV/proton. Finally, at this energy, the beam is forwarded in the RHIC rings where it reaches its final energy and is collided.

The beam consists of bunches which are stored in Radio-frequency (RF) buckets. In Run 6, 120 of them were used, numbered 0-119. During Run 6, the first Yellow bunch crossed with the first Blue bunch at 4 o'clock position, so that at the 6 o'clock position, where STAR is, Yellow bunch 0 crossed with Blue bunch 80. In STAR, bunch crossings are ordered starting from this crossing, called bunch crossing 0. The order of the crossings is dictated by the Yellow beam bunch number. Further, the bunch structure is such that the bunches 111-119, called abort gaps, were left empty and were used for beam abortion. There are other empty buckets, called kicked bunches, which were kicked after injection in order to better diagnose beam characteristics.

RHIC effectively uses only one radio-frequency clock source for the colliding beams and the readout electronics. The frequency of this clock is 9.38 MHz, meaning the time between successive bunch crossings is 107 ns. A bunch (e.g., Blue bunch 1) takes 120 ticks of this clock to complete one revolution of the ring (i.e., the revolution frequency of the bunch is 77.9 kHz). The readout electronics again uses this same clock. Phase delays and "duty factor" (how long the electronics gates are open within the 107 ns frame) are the adjustments made for the electronics. The "bunch crossing" number is measured with the help of a "clock counter" readout (48-bit datum) for each event. Given the 77.9 kHz revolution frequency

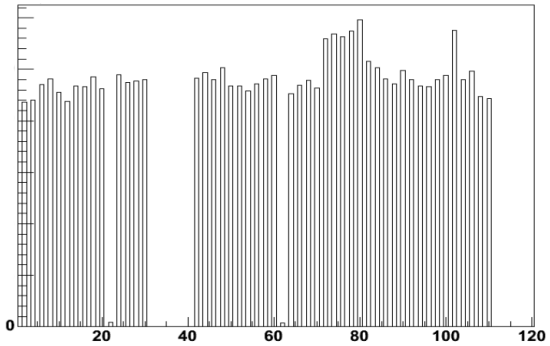

Figure 3.2: A typical beam bunch structure. One can see the abort gaps from bunches 31-39, which were blue beam abort gaps as well as the abort gaps from bunches 111-119, which were yellow beam abort gaps. Also visible are some kicked bunches (21 and 61). The y-axis here is unimportant and so it is not marked.

of a bunch in the ring, the clock counter datum, modulo 120, yields the "bunch crossing" number. These are the numbers quoted on the x axis in figure 3.2.

3.4. Beam polarization

The initial beam polarization of 89-90% is sustained by magnets known as Siberian Snakes [38]. There are two of such magnets in each RHIC ring and one Partial Siberian Snake [39] in the AGS ring. These magnets act in a way that rotates the spin orientation of the protons so that the depolarizing conditions are never fulfilled. When produced, the protons are transversely polarized. To enable measurements with longitudinally polarized protons, both STAR and PHENIX detectors are equipped with spin rotators at both sides or their IPs.

The measurements of beam polarization are done with two types of polarimeters. The proton-Carbon Coulomb Nuclear Interference (pC CNI) polarimeter measures the polarization in short time intervals several times within a single fill. The duration of a fill is typically measured in hours and a single measurement takes about 2 minutes. The statistical precision of any such measurements is about 2%. Located next to these polarimeters is the polarized Hydrogen jet polarimeter [40]. With the gas jet target (GJT), the measured polarization

of the target is effectively transferred to absolute polarization of the beams, using identical particle symmetries for p+p elastic scattering. Sorting p+p elastic scattering data by GJT polarization direction enables a measurement of asymmetries for p+p elastic scattering events, from the measured polarized analyzing power and the measured GJT polarization [41]. Sorting the same data by beam polarization and using the measured value of the analyzing power, as well as using identical particle symmetries, enables determination of the beam polarization.

The orientation of the polarization varies in both blue and yellow rings, so measurements with all four possible combinations of polarization can be gathered in a single run. This is important since it reduces run related systematic errors. A pattern of bunches with different polarization directions is injected into each ring, with the ring dipoles at their injection current values. This is called a RHIC "fill". The polarization pattern of the fill is communicated to the experiments via CDEV (this is a TCP/IP "socket" connection between a computer at RHIC main control and a computer in the STAR counting house). A data block is transferred from RHIC to STAR on a regular basis. The STAR computer running CDEV listens on its socket connection, and then stores the data block into a database.

After filling the rings, a sequence of operations takes place: (1) acceleration ramp - this is literally a current ramp of the magnets in the RHIC ring. In some cases higher order multipoles have a complex ramp, to allow control of the betatron tunes during acceleration; (2) cogging of the beams - this locks the RF systems of the two rings, which is an essential step for initiating collisions between the beams and (3) background reduction - there are beam collimators that get inserted after the first two steps to reduce single beam backgrounds.

The time dependence of rates that demonstrate the aspects of a fill are given on figure 3.3. The "in-time" BBC east-west coincidences are proportional to luminosity and the "out-of-time" BBC east-west coincidences are dominated by single-beam backgrounds. The luminosity of the beam decays with time and single-beam backgrounds can be time dependent. When the backgrounds are low enough, one can actually see in the "background monitors" the insertion of the carbon fiber targets from the pC CNI polarimeter.

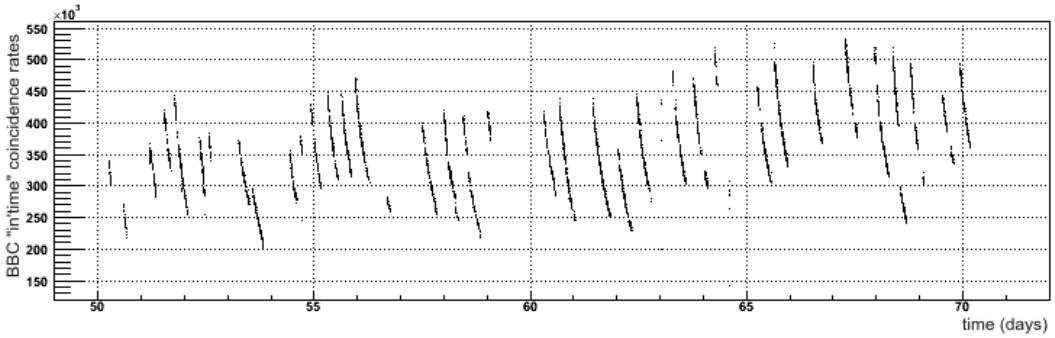

Figure 3.3: The BBC "in-time" coincidence rates. The image here shows the counts of "in-time" coincidence rates for one of the later RHIC Runs. One can note that the image has the same form as image 3.18, also showing BBC coincidence rates for entire Run 6.

3.5. The STAR detector

The Solenoidal Tracker At RHIC (STAR) [42, 43] was built in order to measure nuclear interactions and polarized particle phenomena. It is located at the 6 o'clock interaction point on the RHIC ring in a hall named Wide Angle Hall (WAH). The "Yellow" beam comes from the west looking in the negative z axis of the local coordinate system. The center of the local (STAR) coordinate system is placed at the interaction point with the x axis pointing south and the y axis pointing up. The view of the midrapidity section of the STAR detector is shown in the figure 3.4.

The detector consist of ≈20 subsystems (the number varies on a yearly basis), many of which are not relevant for this thesis. The largest detector, providing tracking information for the particles, is called the Time Projection Chamber (TPC) and takes most of the STAR detector volume. Aside from the detectors on figure 3.4, which are all in the midrapidity section, STAR includes forward angle detectors. Some of these are relevant to the thesis and will be described here. Of all the forward angle detectors, Beam-Beam Counters (BBC), Forward Pion Detector (FPD), Forward Pion Detector++ (FPD++) and the Zero Degree Calorimeters (ZDC), two are of crucial importance: FPD++, and less so, the BBC. None of the forward detectors can not be seen on the figure 3.4, but are visible in the larger scale top view.

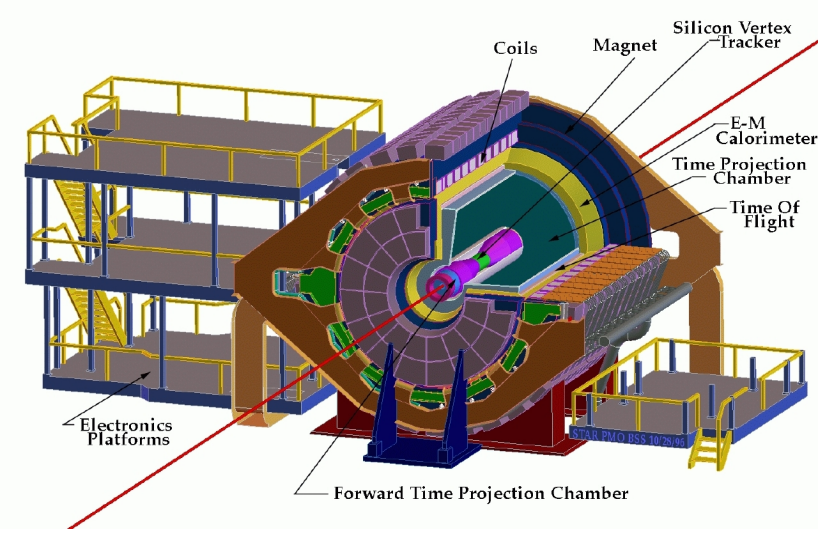

Figure 3.4: View of the midrapidity section of the STAR detector. In the cross-section one can see the basic parts of the detector. The FPD++ detector is located "outside" of this picture.

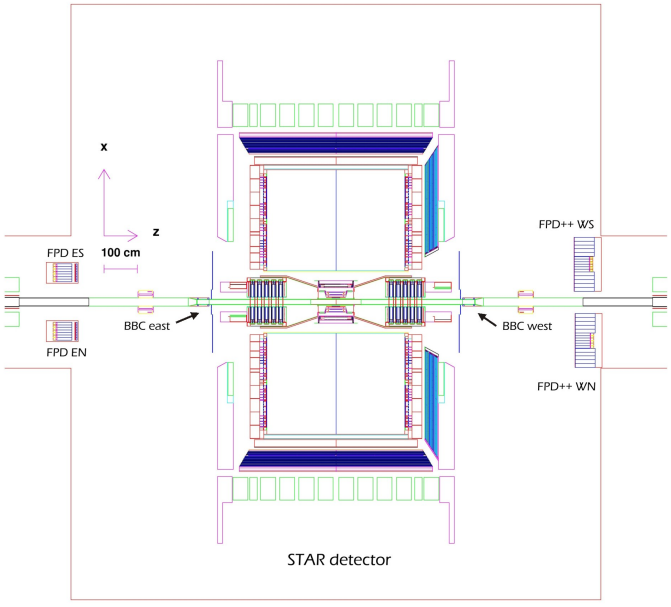

Figure 3.5: Top view of STAR detector. Noted in the figure are the BBC and FPD++ detectors. "W" stands for west, "E"' for east, "N" for north and "S" for south.

A very important part of the STAR detector is its magnet [44]. It is 7.32 m in diameter, 7.25 m long and operates with a field set from 0.25 T to 0.5 T. It is a large solenoid magnet capable of producing a field uniformity better than 1000 ppm over a portion of its interior region encompassing the entire Time Projection Chamber volume.

Although the STAR detector coordinate system is well defined and operational, a more common and useful way of describing the placement of a detector is with pseudorapidity. This is a variable defined by:

$$\eta = -\ln\left(\tan\frac{\theta}{2}\right), \tag{3.1}$$

where θ is the polar angle measured from the interaction point. This naturally assumes a static interaction point in the center of the STAR detector. Since the only vital variables to the interaction are the angles of the outgoing particles, this is a good description of any detector system. The approximate range of pseudorapidity the detectors fall in is given in table 3.2.

Detector	Lower η bound	Upper η bound
Time Projection Chamber (TPC)	-1.2	1.2
Barrel Electromagnetic Calorimeter (BEMC)	-1	1
Endcap Electromagnetic Calorimeter (EEMC)	1.07	2
West Forward Time Projection Chamber (wFTPC)	2.8	3.8
East Forward Time Projection Chamber (eFTPC)	-3.8	-2.8
Beam-Beam Counters (BBC) (small tiles)	3.5	5
Beam-Beam Counters (BBC) (large tiles)	2	3.5
Forward Pion Detector (FPD)	movable -3.3-4.1	
Forward Pion Detector++ (FPD++)	2.7	4.0
Zero Degree Calorimeter	6.5	7.5

Table 3.2: Pseudorapidity ranges of some STAR detectors

3.5.1. Beam-Beam counters

The STAR beam-beam counters (BBC) are hexagonal scintillator annuli mounted on the outside of the STAR magnet. There are two annuli tiled by small and large hexagonal cells, the large cells having exactly four times larger dimensions than the small cells. In the center of each is a small hexagon marked "B" which is reserved for the beam pipe. The size is such

that the small regular hexagons can be inscribed in a circle of diameter 9.64 cm.

The scintillators were cut from 1 cm thick Kuraray SCSN-81 by F.Pompei. After machining, the sides of the hexagons were covered with white reflecting paint to trap scintillation light within each tile. Each scintillator surface was then covered with 1 μm thick aluminized mylar, taped to the painted scintillator edges. The reflectors were then covered by 10 μm thick black construction paper and black electrician's tape, to make the assembly light tight. The final placement of the detectors along the beam is at the distance of 3.7 m from the IP, which places them in the pseudorapidity range of $3.3 < |\eta| < 5.0$. This, and the front view of the detectors are seen on the figure 3.6.

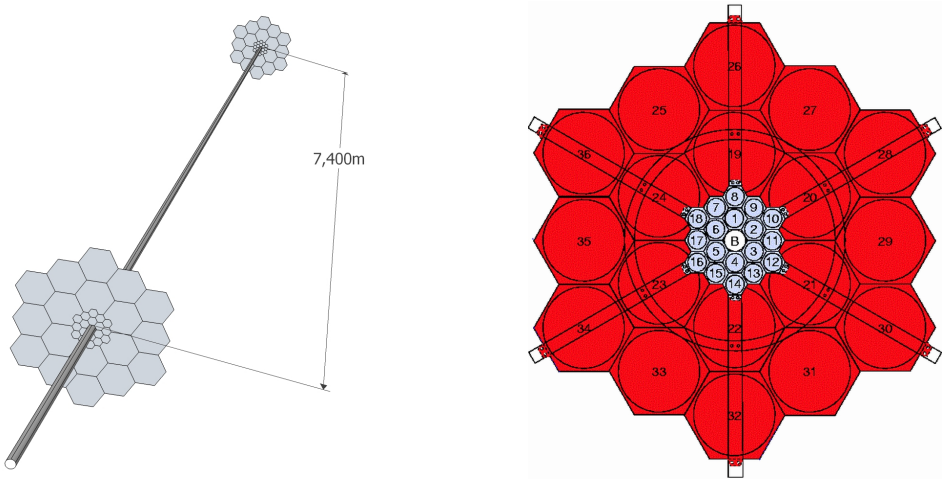

Figure 3.6: A perspective and a front view of the BBC modules. The small hexagon marked "B" is reserved for the beam pipe. The size is such that the small regular hexagons can be inscribed in a circle of diameter 9.64 cm.

The BBC is used for many purposes, among which are measurement of relative spin-dependent luminosity, providing the minimum bias (MINB) trigger to the STAR detector and local polarimetry. The relative spin-dependent luminosity is measured as the ratio of luminosities for different polarization directions for the colliding bunches. Since an average event has ≈ 4 BBC phototubes per side occupied and the topology of that occupation is spin dependent, the BBC serves as a local polarimeter.

The minimum bias trigger is a condition of coincidence between both BBC modules within an allowed time period. There are "time-to-amplitude" (TAC) converters installed that are started by a east (or any west) small tile crossing a discriminator threshold, and stopped by the RHIC clock. Essentially, TACs are switched current sources. A single TAC is switched on at one time, and switched off at a second time. The current from the TAC is encoded by an ADC and the ADC count is proportional to the time between start and stop of the TAC. For RHIC Run 6, 8-bit ADC were used to encode the TAC data and the charge information from each BBC photomultiplier tube. The difference between the largest TAC datum from east (i.e, the earliest hit) and the largest TAC datum from the west is then computed. This time difference is directly proportional to the z position of the vertex.

The counts within an event are used as a measure of relative and absolute luminosity. Obviously, the ratio of number of recorded events for two runs will equal the ratio of recorded luminosities for those runs. The absolute luminosity at STAR is obtained by measuring the spatial profile of the colliding beams and the number of protons in each beam. Specifically, for two bunches containing n_1 and n_2 particles that collide with an average frequency of f, the luminosity is defined by:

$$\mathcal{L} = \frac{n_1 n_2 f}{4\pi\sigma_x\sigma_y}\,, \tag{3.2}$$

where $\sigma_{x(y)}$ stand for the Gaussian transverse beam profiles in x and y directions, given that the beams are moving along the z direction. The numbers of colliding particles are measured by wall-current monitors and the frequency of the collisions can be calculated from the energy of the beam and the number of bunches. The transverse beam profiles are measured by the BBC during the so-called vernier scan [45]. The cross section for the BBC is then determined as $\sigma_{\mathrm{BBC}} = \mathcal{R}/\mathcal{L}$, with $\mathcal{R}$ being the reaction rate observed by the BBC. The BBC cross section, measured in this way, is equal to $\sigma_{\mathrm{minb.}} = 26.1 \pm 2.0$ mb, consistent with simulation [46, 47]. Once the cross section is determined, the luminosity can be determined by measuring BBC interaction rates.

3.5.2. FPD++ – general description of the detector system

The Forward Pion Detector ++ (FPD++) is a modular detector consisting of two equal detectors as shown on the figure 3.7 (faces of the detectors as viewed from the beam). These detectors are placed on the west platform of the STAR detector at the approximate distance of 720 cm away from the interaction point. Also shown on the plot is the local detector coordinate system, which is inverse of the star system and the range of covered pseudorapidity. For each of the modules the row/column designation is noted. The points marked on the face of the detectors are survey measurements given in the table 3.3.

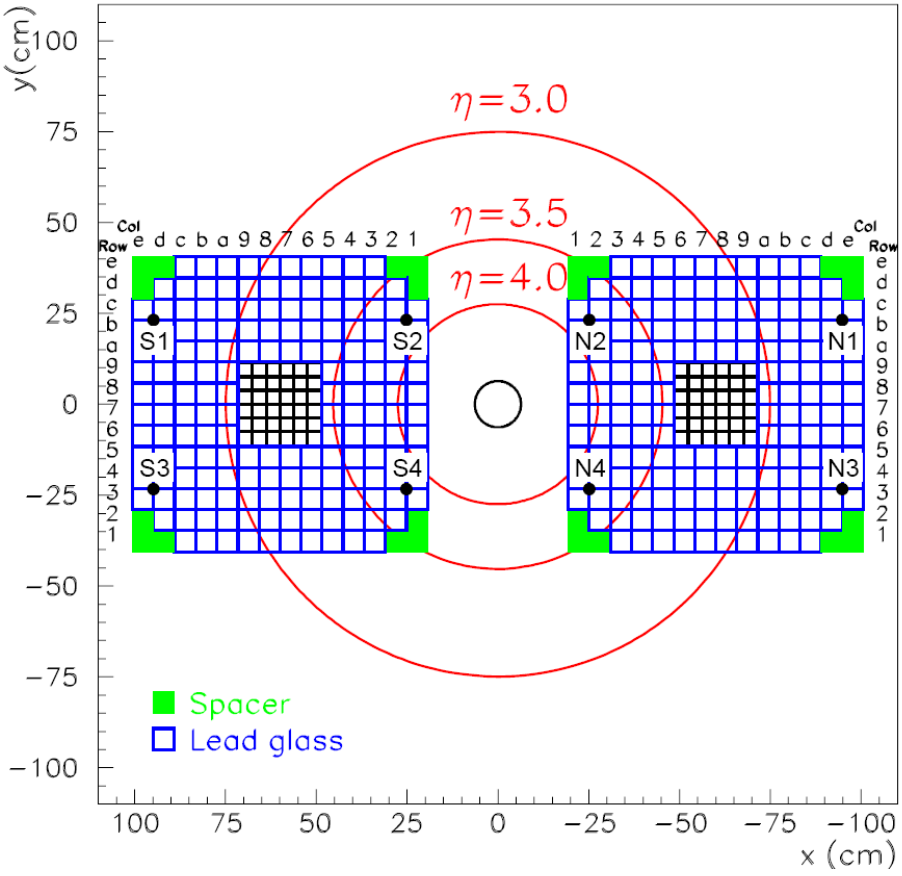

Figure 3.7: Beam view of the Forward Pion Detector ++.

Mark	x(m)	y(m)	z(m)	Mark	x(m)	y(m)	z(m)
S1	0.926	0.236	7.185	N1	-0.934	0.243	7.226
S2	0.220	0.244	7.201	N2	-0.235	0.243	7.210
S3	0.917	-0.230	7.185	N3	-0.928	-0.221	7.223
S4	0.218	-0.222	7.199	N4	-0.236	-0.225	7.209

Table 3.3: Survey point measurements of the detector placement.

Given this geometry, the geometrical acceptance of a single module can be easily calculated in the η–ϕ space. The acceptance of the calorimeters is given on figure 3.8. The spacers and the dead cells are not taken into account while plotting. The black line inside the acceptance is the border of the inner and outer modules.

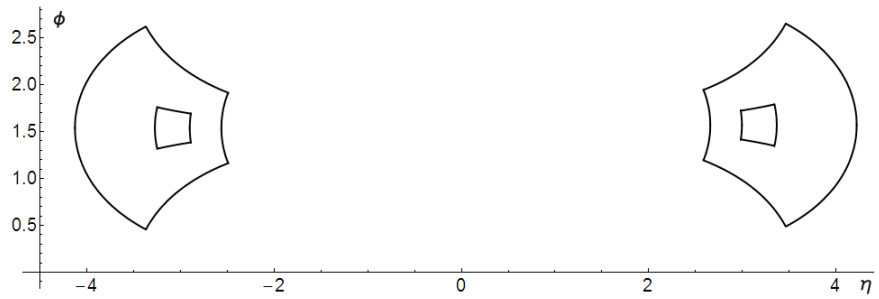

Figure 3.8: Acceptance of the the FPD++ in η–ϕ space. Spacers and dead cells are not taken into account while plotting this figure. The inner line represents the border of the inner and outer module.

3.5.3. FPD++ – Description of individual detector cells

Each module consists of two types of lead glass detectors. Lead glass allows one to detect energetic electromagnetic showers. For an incoming particle (photon, electron, positron) there are several mechanisms to produce electromagnetic showers. The main contributions to showers come from "pair creation" (the conversion of the energy of a photon into an electron/positron pair near a large-Z nucleus) and "brehmssthralung" (the radiation of a photon by an electron or positron as it gets accelerated by the Coulomb field of a large-Z nucleus). Further, within the glass, the electrons and positrons in the electromagnetic shower

that have speeds larger than c/n, where n is the index of refraction of the glass, will emit Čerenkov radiation. A more complete overview of the electromagnetic showers is given in the appendix. All the photons from the shower are transported through the glass to the photocathode. The overlap of the power spectrum of the radiation (growing power with photon frequency) and the quantum efficiency of the photocathode (decreasing at higher photon energies) provides a window of operation for a leadglass detector.

Type A cells (36/calorimeter)

- lead glass of dimensions 3.6 cm x 3.6 cm x 45 cm, each weighting 2.5 kg.
- FEU-84 12 stage photomultipliers (PMTs)
- 1400 V / 0.2 mA resistive dividers

Type B cells (168 / calorimeter)

- lead glass of dimensions 5.8 cm x 5.8 cm x 60.2 cm, each weighting 10 kg
- Amperex XP2202 10 stage photomultiplier
- 1200 V / 1 mA resistive divider

Type A lead glass array was taken from the previous versions of the Forward Pion Detector. The blocks are of type TF101 with a radiation length of $X_0 = 2.5\,\text{cm}$. This type of glass is composed of 51% lead oxide, 41.5% silicon oxide and 7% potassium oxide. Each block is 45cm long, and hence, is 18 X_0 long. Each detector is wrapped by aluminized mylar reflector.

Type B lead glass array was obtained from the University of Chicago which used it in the E731 experiment at Fermilab. Before coming to BNL, they were refurbished at U. Colorado by a group headed by John Cumulat for the FNAL E831 experiment. The blocks were cast by Schott and are of type F-2 with a radiation length of $X_0 = 3.21\,\text{cm}$. This type of glass is composed of 45% silica, 45% lead oxide, 5% sodium oxide and 5% potassium oxide. Each block is 60.2 cm long, and hence, is 18.75 X_0 long.

After bringing the cells from Fermilab, they were carefully inspected, tested and repaired if needed. All of the cells were unwrapped from the mylar, possibly had the optical coupling to the phototube removed from the face, and were cleaned with an ammonia solution. On some cells, the glass was decoupled from the phototubes due to imperfections such as ripples or bubbles in the silicone "cookies" used to couple the phototube to the lead glass. To be more precise, the ultraviolet filters were that were included in the coupling would typically have the ripples and the bubbles were imperfections in the silicone cookies. Next, a 25.2 cm x 61.2 cm mylar foil was cut and was taped on the cell at the PMT coupling and wrapped safely around the cell. The front face of the cells was left without mylar.

A quantity that raised initial concern was the dimensions of the blocks. The process of measuring was very important as roughly 10% of the blocks (on arrival) were smaller than the rest. This variation in block size is shown in the lego plot on figure 3.9. It is quite evident that the blocks were fabricated in two clusters. Still, this was a small fraction of the blocks and the cell size was measured before cell wrapping. Best effort was done in the wrapping of the cells to cancel this effect in case some cells that are evidently smaller should be used in part of the calorimeter.

The photomultiplier tubes used for type A cells were FEU-84. The bases have resistive voltage dividers with a total resistance of 9.2 MΩ that provide the voltage differences to the twelve dynode stages of the FEU-84. The dividers typically operated at a voltage of about -1600 V. Originally, the Pb glass, PMT's and dividers were taken from old detector array built at IHEP, Protvino for the E704 experiment at Fermilab.

The photomultiplier tubes for type B cells are of type Amperex XP2202 FL/B. The FL stands for flying leads. The tubes are 10 stage with a bialkali photocathode. They have a maximum external diameter of 51.5 mm and an active photocathode area sensitivity of 44 mm. Tubes were chosen to have as large an active area glued onto the glass as possible. The base was soldered onto the leads of the tube and then potted onto the tube. The voltage on the base is typically 1200 V with an average gain of $1.2 \cdot 10^5$. The maximum and minimum voltage for good operating conditions are 1600 V and 1100 V. The phototubes are fitted with

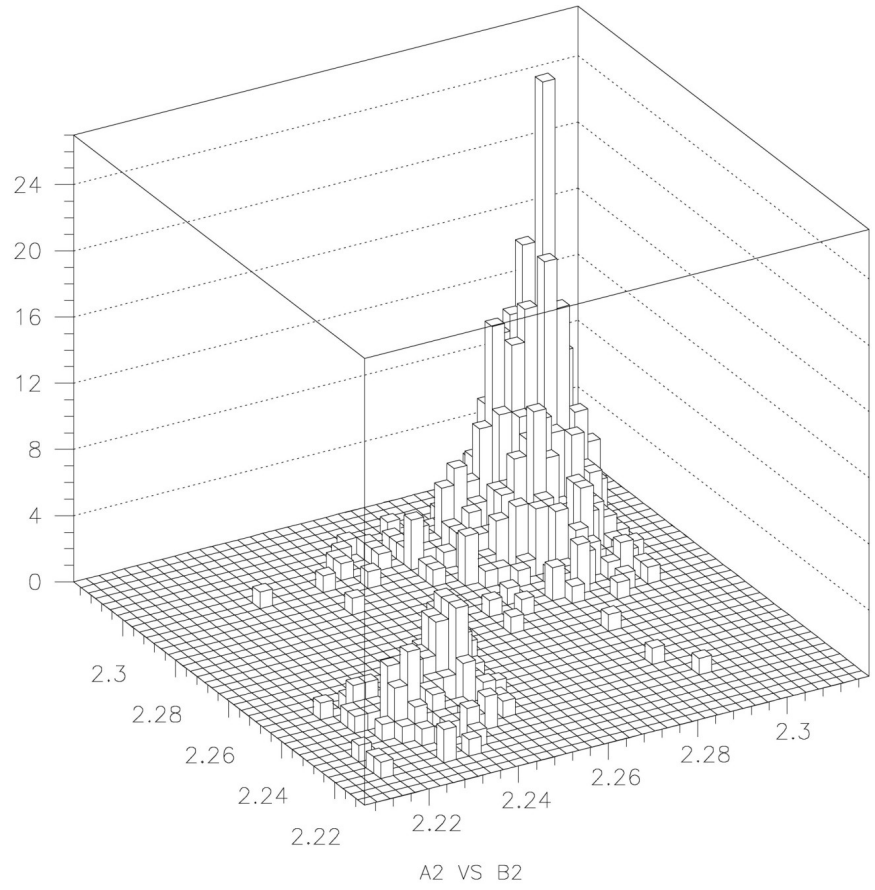

Figure 3.9: Correlation between the transverse dimensions of the E-831 lead-glass cells. Units of measurement are inches. Two distinct groups of cells are apparent.

a layer of optical gel, a mixture (by volume) of approximately 1:2:.3 of GE RTV615A, GE SF9650 silicone fluid, and GE RTV615B curing agent. A Wratten 2A filter is embedded in the gel to reduce the sensitivity to variations in shower depth. Optical contact between the block and phototube is thus provided by the silicone gel with an index of refraction of 1.45, which lays between that of the glass and the phototube face.

A test stand was prepared to ensure all the cells were functional. Cells were placed in a blackbox containing an LED light source whose frequency was possible to change. The PMTs were powered by an external high voltage supply. Gain of the cell versus the applied

voltage on the phototube as well as versus the frequency of the source was tested. A typical set of curves is given on figure 3.10.

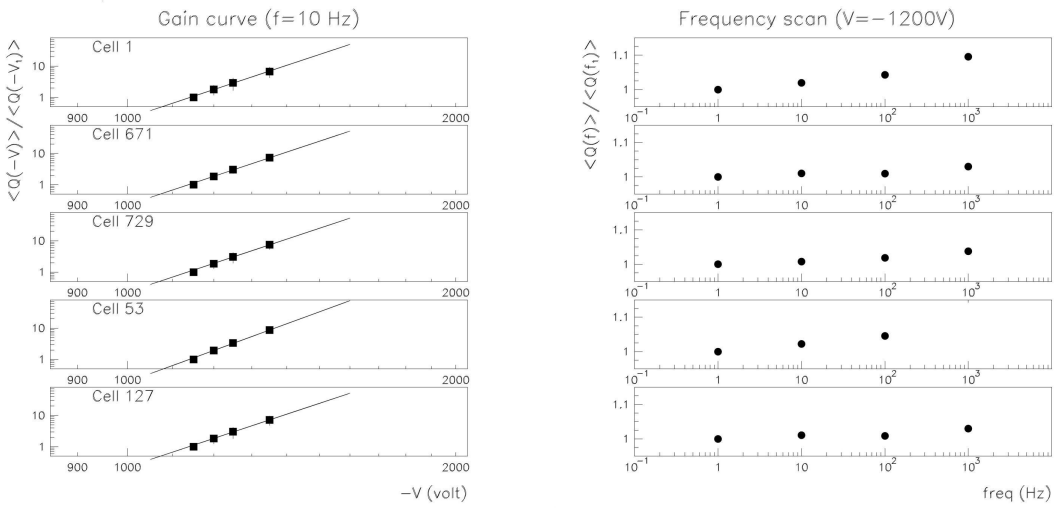

Figure 3.10: Gain curves for the tested cells. Shown are the dependencies of gain vs. applied voltage and vs. frequency of the source.

The phototubes were also tested for afterpulsing and in-set gain variations. Afterpulsing arises from feedback in a photon detector. The "feedback" typically comes from the ionized gas in the phototube, with the positive ions slowly drifting back to the photocathode. Upon impact, the positive ions knock off electrons from the photocathode, that give rise to the afterpulse. In practice, this means that each real signal pulse can be followed by an afterpulse at a later time, and this afterpulse can last undesirably long time. To test it, the voltage on the tubes was set at -1500 V, the LED was operating at a frequency of 1.01 kHz, and the oscilloscope was running with a persist time of 5 seconds.

Type A cells had no visible afterpulse. Measurements showed that the afterpulse was less than 1 percent of the original signal. Type B cells had an afterpulse that lasted on average about 10 microseconds. At about two microseconds, the afterpulse peak is about 1% of the main peak from the LED. The gain for the different cells in the whole set was found to vary, although not significantly. The gains of type A cells were on the order of 10 times smaller

than the gains of type B cells. The variations in gain of type A cells were smaller than in type B.

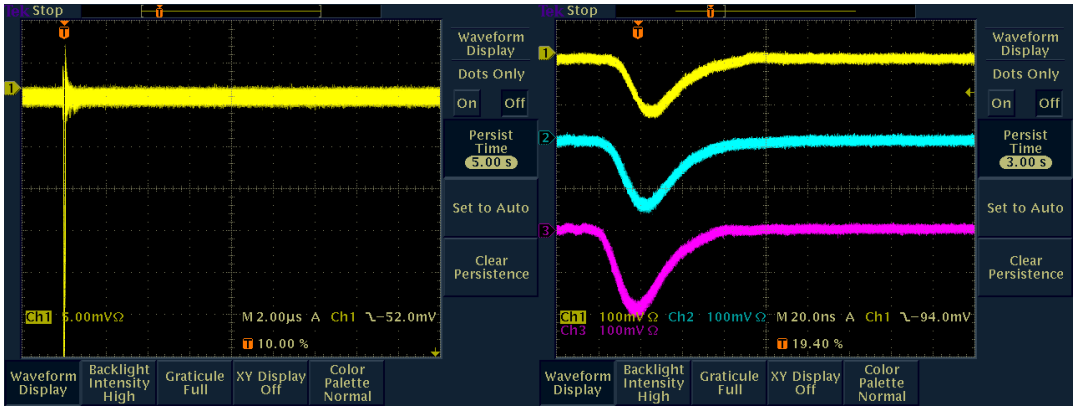

Figure 3.11: FEU-84 phototube afterpulse and in-set gain variations. In the left side of the figure is the view of the afterpulse, which falls to about 1% of the main peak in very short time(not visible on the graph). The gain variations on the same applied voltages for three randomly chosen cells are visible from the right image.

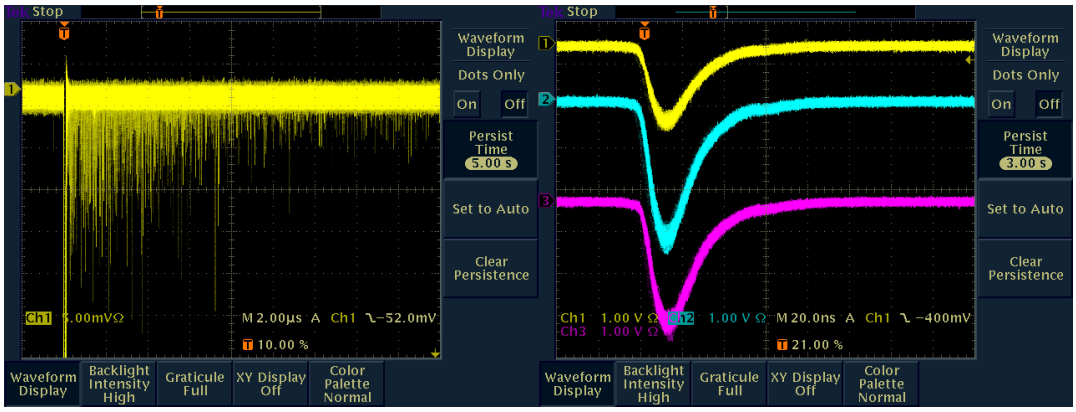

Figure 3.12: XP2202 phototube afterpulse and in-set gain variations. In an average 10 microsecond afterpulse, the afterpulse peak falls to about 1% of the main peak in 2 microseconds. The gain variations on same applied voltages are visible from the right image.

Once the detectors were in place, a Light Emitting Diode (LED) system was put in place to monitor the stability of individual detectors. The system consisted of two boards, each containing two LED pulse drivers that were sending light signals through a set of fibers to

individual cells. The system flashed on a regular basis to measure the stability of detectors vs. time. The energy delivered in a single flash was greater than the energy of a typical event, so there was no interference between the two. The panel can be seen on figure 3.13.

Figure 3.13: The LED panel used to monitor the cell stability. The panel was installed in front of the face of each detector, providing light pulses that would allow monitoring cell stability. One can see the two driver modules and four fiber bunches.

3.5.4. FPD++ Detector enclosure

The cross section of the final stack of one of the modules is on the figure 3.14. Visible on the picture is the placement of the phototubes, large and small cells and spacers. Two identical enclosures were made to hold the detectors and part of the signal / high voltage cables. The enclosures were aluminum boxes with Delrin glass supports. Not seen on any of the two pictures is the LED fiber panel that goes between the detectors and the front face of the enclosure. The final look of the completed detector, without the LED panels and the front enclosure is given in figure 3.16.

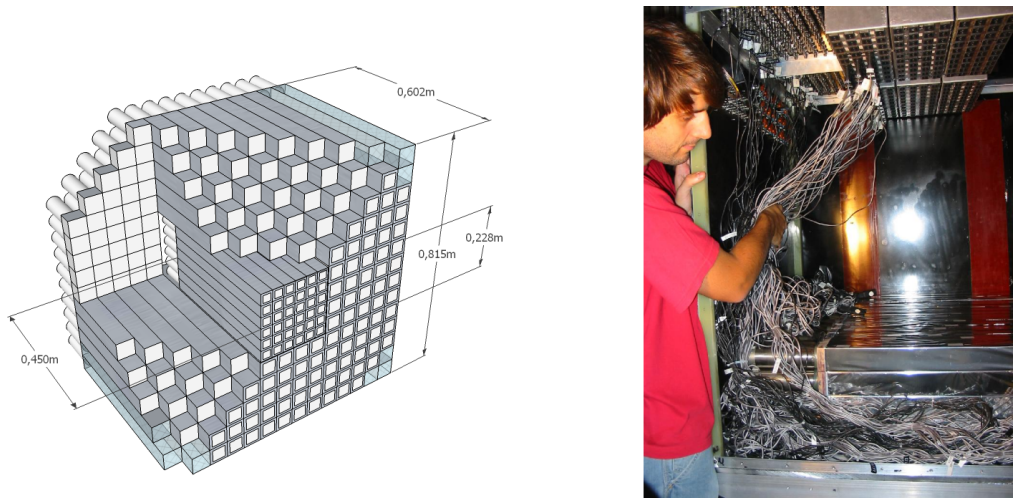

Figure 3.14: Left: Diagonal cross section view of the FPD++. One can see the placement of all the components and their dimensions. The openings on the front faces of the detectors are not identical on every cell, as indicated here, but vary slightly. In reality all cells are of same length, figure only for demonstration purposes. Right: inside view of a module while assembling. Visible is the enclosure along with the cables and cable connecting patches (top).

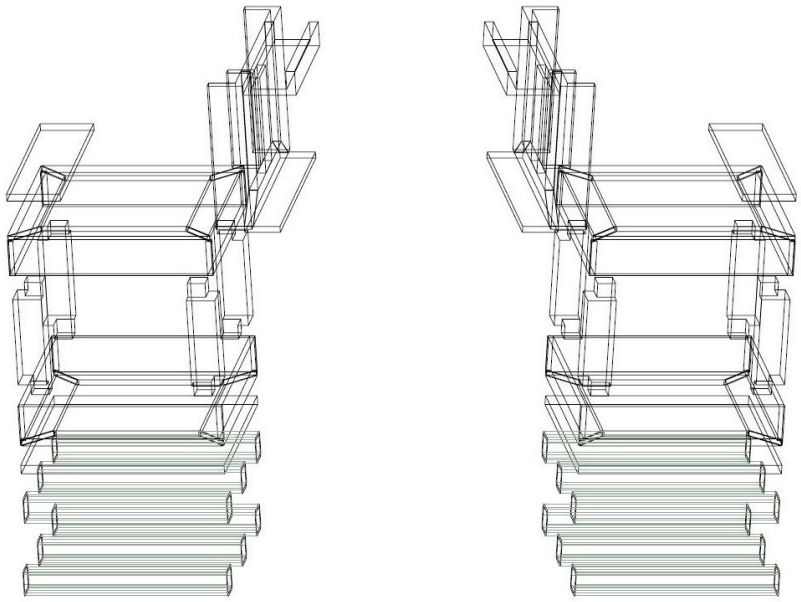

Figure 3.15: Schematic view of the enclosure for the entire FPD++. The scale is roughly 1.35 m front face of a single side diagonal.

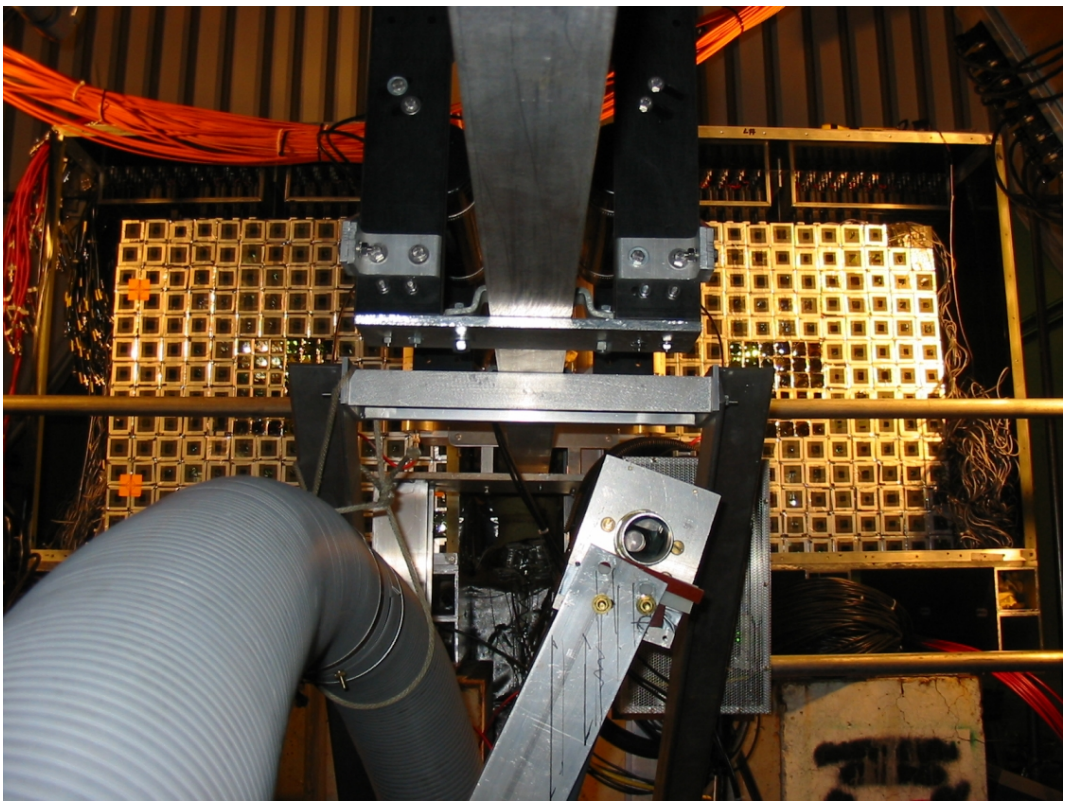

Figure 3.16: The final look of the completed detector without the LED panels and the front enclosure.

3.5.5. FPD++ Readout electronics

The first proposal for readout electronics for the FPD++ was to use a hybrid system of CDB (Central-trigger-barrel Digitizer Boards) / DSM (Data Storage Module) boards and CAMAC (Computer Automated Measurement And Control) ADCs (Analog Digital Converters). Available from the previous detector (FPD west) readout were:

- eleven 16-channel 8-bit digitizer boards
- eleven 128-bit layer-0 DSM boards
- two 128-bit layer-1 DSM boards

- twelve 16-channel CAMAC gated ADCs (LeCroy 4300B)
- one 64-channel CAMAC logic module (LeCroy 4564)
- NIM electronics to form pretrigger-gate; fast clear (no event); and readout trigger (good event) for gated ADCs
- Coincidence register to latch trigger token

The planned implementation of FPD++ readout electronics is given on figure 3.17.

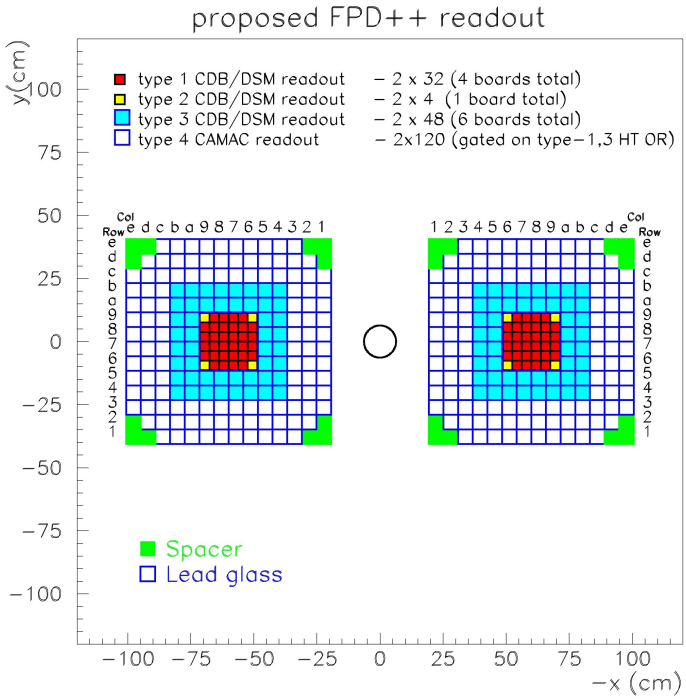

Figure 3.17: Proposed readout electronics for the FPD++.

This plan, however, was found to have noise-related issues with the CDBs during the first stages of the Run. There was extensive testing of the CDB readout of the FPD++ prior to the Run, and many things were found/fixed during these tests, most having to do with the leading-edge discriminators. However, during the Run, essentially all "trigger clock distribution boards" (TCD) for the many different subsystems of STAR are utilized. Hence,

different behavior of the electronics during a Run relative to electronics performance during tests prior to when a Run begins can easily appear. Among other things, the TCD for the detector supplies the gate to the CDB, which impacts the "during the Run" performance.

Different approaches were taken to eliminate the electronic noise found in the CDB. It was most likely associated with the CDB gate, sourced by the FPD-TCD, specifically by some interaction in the crate housing all the different TCDs, thereby impacting the clocking signal that was the gate source for the FPD++ CDB. The best solution found was to reduce the number of CDB boards used for the readout. Hence, a switch from CDB to CAMAC readout was implemented. This eliminated the noise, making it possible to operate the FPD++ during Run 6, but it also eliminated the possibility of triggering on the "blue cells" given in the figure 3.17. The result of all these changes was effectively replacing the blue cells in figure 3.17 with white cells.

3.6. Event selection

3.6.1. RHIC Run 6

The data presented here were all collected during RHIC Run6 [35] which started on February 6, 2006 and lasted until June 26 of the same year. This Run only focused on polarized proton collisions, both in the data collection mode and in the machine development mode. Four different beam energies were used; two of them only for machine development. A table and a figure with an overview are given here.

$\sqrt{s}$ [GeV]	Experiments taking data	Begin date	End date
200	STAR / PHENIX	07/02/06	05/06/06
22.5	—	05/06/06	06/06/06
62.4	STAR / PHENIX / BRAHMS	06/06/06	20/06/06
500	STAR / PHENIX (participated)	20/06/06	26/06/06

Table 3.4: Run 6 breakdown - energies, experiments and dates.

Out of the all the transverse data, a subset taken from 31 RHIC fills was used for the analysis. This data were taken during the time period which fell in between what was

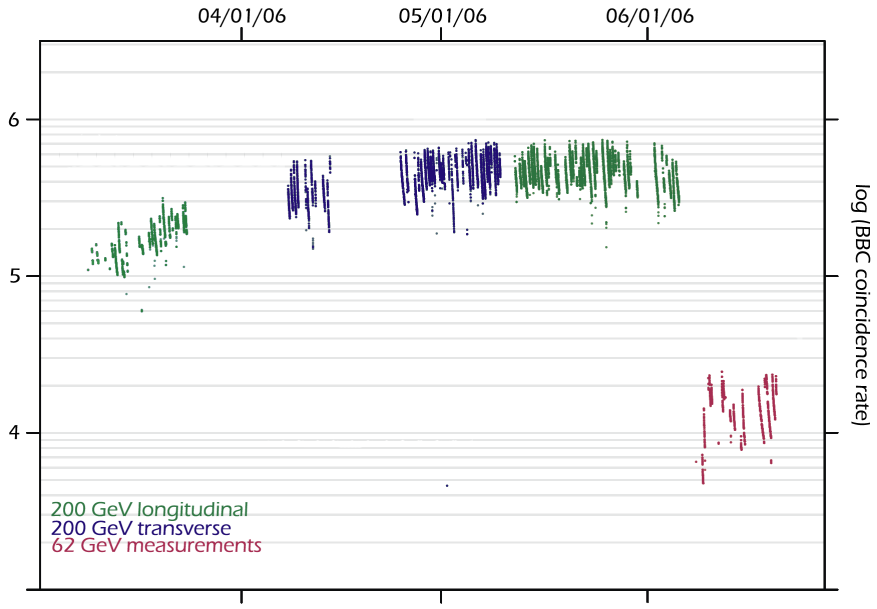

Figure 3.18: Run 6 data collection at STAR. Each dot is a STAR run. The set of dots colored blue is the only one relevant to this thesis.

called "Day 7116" and "Day 7129", lasting 2 weeks. Not all of the STAR runs taken during this time were used; out of a total of 1207 runs, 659 were marked bad by either the shift leader or the RTS or were not saved, leaving 548 runs. Further, during the reconstruction of the data, runs got excluded on basis of various reasons. These were typically disagreement between spin pattern and the spin bit, missing data or segments during the run, bad run-stop synchronization, runs with no local DAQ events, very short runs etc. In total, this excluded another 206 runs, leaving a clean dataset of 342 runs.

3.6.2. Detector level event selection

Several triggers were proposed, but given the changes that had to be made to the readout electronics, mentioned earlier in the text, a trigger that emulates the FPD trigger had to be selected. This decision makes calibrating the cells that have CAMAC readout much more difficult, as will be seen later.

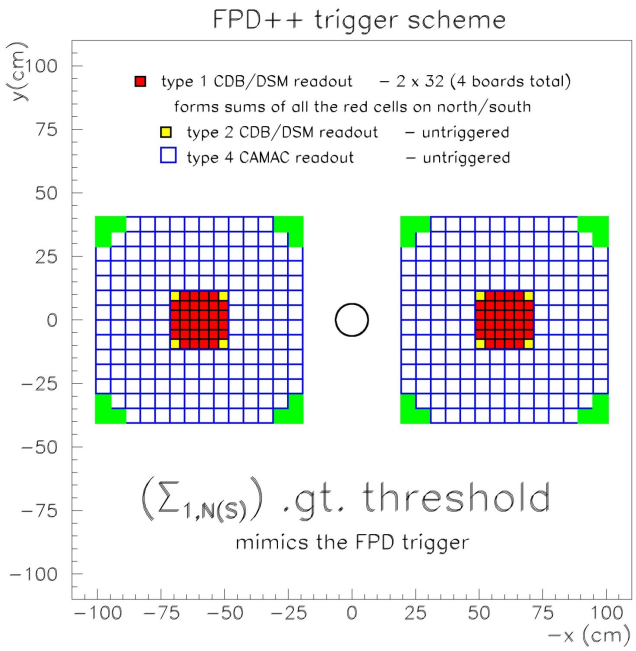

Figure 3.19: Final trigger scheme used in the FPD++ during Run 6.

The threshold value that mimics the FPD trigger was set to 75 ADC counts. This approximately equals 15 GeV of deposited energy per module, since a single count is found to be produced by a 0.2 GeV photon. Given this configuration, FPD++ had a trigger that was essentially decoupled from STAR. During running in physics mode, FPD++ would take data when this trigger was satisfied, sometimes regardless whether the BBC minimum bias condition was also present.

Some study was made of the events that satisfied the FPD++ summed energy threshold, but failed to satisfy the minimum bias condition. Bunch counter distributions for this class of events showed the presence of single-beam backgrounds (i.e., events in abort gaps). Consequently, the software was set up to include a minimum bias condition, as had been done in prior years at the trigger level. The trigger was thus set in the software to represent a combination of these two independent triggers.

3.6.3. Analysis level event selection

The analysis level event selection depends on the type of analysis considered. Separate sets of cuts were put in place for the calibration, single pion asymmetries and multiphoton events.

The calibration procedure uses the known characteristics of the neutral pion. So, events from the sample were filtered out that most likely originated from single neutral pions. More on the particle characteristics is given in the Appendix. The characteristics of a neutral pion with an energy of 30 GeV suggest that it will travel an average of 60 nm before it decays, so the origin of decay can be considered to be at the primary vertex. Further on, one can restrict the kinematical parameters of the two outgoing photons. A typical set of cuts for calibration looks like:

- Minimal energy deposited in a single calorimeter module
- A cut not allowing any of the LED events to enter in the event sample
- The number of reconstructed photons within a calorimeter module
- A fiducial volume cut, restraining the photons to be within a certain space
- Cut on the energy sharing between the two photons reconstructed as pion daughters
- Cut on the invariant mass of the two photons reconstructed as pion daughters
- A cut on the position of the reconstructed vertex point

The set of cuts imposed for the multiphoton analysis is significantly different:

- Minimal energy deposited in both the small cell calorimeter and in the same side large cell calorimeter
- Total minimal number of cells with an energy above a threshold energy within a calorimeter (small + large)
- Total weighted minimal number of cells with an energy above a threshold energy within a calorimeter (small + large)

- Total maximal number of cells with an energy above a threshold energy within a calorimeter (small + large)
- A cut not allowing any of the LED events to enter in the event sample
- A fiducial volume cut, restraining the reconstructed multiphoton event to be within a certain space
- Minimal transverse momentum of the reconstructed multiphoton event
- Cut on the size of the cone of the multiphoton event in the η–ϕ space

The parameters in these sets of cuts were changed continually to observe their influence on the results. Finally, for the analyses, optimal sets of cuts were chosen which minimally bias the event samples.

Chapter 4.

Data analysis

4.1. Monte Carlo simulation sample

The simulation sample was generated for this analysis to give guidance on many aspects, such as calibration, determination of the quality of the results, determination of possible biases the trigger could introduce, jet reconstruction on more levels than just the detector level etc.

The events were generated by the PYTHIA 6.222 event generator [46] and the detector responses were modeled with a GEANT [47] based STAR program. The PYTHIA events were generated from simulated pp collisions at $\sqrt{s} = 200\,\mathrm{GeV}$, allowing for the minimum bias processes. The processes were allowed the entire range of p_T values for hard $2 \to 2$ processes, and given a lower cut-off on p_T of 1 GeV for processes that are singular in the $p_T \to 0$ limit. The cross section of the processes depends on p_T, and as it was shown earlier, for example on figure 2.6, the forward production will mostly be sensitive to high x quark + low x gluon interactions. The interaction point (z vertex) was a Gaussian randomized function with a mean of 0 cm and a variance of $(60\ \mathrm{cm})^2$. The parameters of this distribution are chosen in such a way to approximate the vertex distribution of the minimum bias events in the data.

In this way, 90 000 files were created, with each file containing 100 000 PYTHIA events. This sample corresponds about 4% of the Run 6 data. The events were then passed through a GEANT [47] model of STAR. The GEANT model accounts for the most important materials

in the STAR Wide Angle Hall, and accounts for magnetic field from the solenoid. Interactions of particles with all the material are simulated and a timeline of the event can be obtained. The simulated FPD++ detector was placed at the exact location given in figure 3.7, which would ensure largest possible resemblance of the simulated and the real detector. The cell width, cell wrap width and the distance between cells was kept constant in the simulations, unlike it was in the real detector, as can be seen from figure 3.9. This was done so since these effects are negligible.

On the 100 000 simulated PYTHIA events in a single file, an energy cut was imposed before passing the event to GEANT. If the energy of the events would pass a threshold of 15 GeV, the event would be passed on the reconstruction and otherwise the event would be discarded. In this way, all the low energy events which don't contribute to the soft trigger are discarded immediately and the GEANT calculating time is greatly decreased. Since the cross section for these events is a rapidly falling function with energy, the fraction of the events left in this way is small and turns out to be on the order of 0.5% of the total number of simulated events. Hence, 1 000 GEANT reconstructions per file were found to be enough to ensure all the events would pass through the STAR reconstruction and yet the computing time per file isn't too long. Finally, in our case, events were only saved if they satisfied a soft trigger, which was a simulated small cell module summed energy threshold set to 15 GeV. This trigger was set up to mimic the original hardware trigger used for obtaining the data.

4.2. General analysis steps

Analysis of the data taken with FPD++ can be divided in several steps:

1. Determination of pedestals and pedestal subtraction. This is due to the fact that the readout electronics will produce non-zero signals in the absence of any events or, for that matter, the beam itself. Important issues to understand here are the sizes of the pedestals as well as their behavior over time. The pedestals, naturally, after determined, have to be subtracted from the data.

2. Calibration of the detector. Different methodologies can be employed here, and the usual one, if possible to do, relies on the reconstruction of neutral pion events. Individual detector gains are adjusted in such a way that the reconstructed values for the π^0 mass is correct. Again, one should be careful of the time dependence, deposited energy dependence etc. Another methodology, if the π^0 event method does not satisfy, is calibration by matching energy deposition slopes.

3. Using the results of the calibration to make an event selection specific for each analysis. This will give first physical observables from recorded data.

4. Spin-sorting the obtained results and calculating the asymmetries. This step is common to all the analyses in question here.

4.3. Determination of pedestals and pedestal subtraction

The readout electronics will always, in general, produce non-zero signals. This, in a general event, means that the recorded number of counts in a single ADC module will be different than what we would have predicted based on the assumption that the detector response is uniform. The first analysis step is to determine these pedestals and subtract them from the data. There are different methods of pedestal determination, and the simplest one is to select an event set that is mostly "collision-free". There is also the possibility to look at the events that were recorded when there was no beam present. These are routinely taken during the STAR Run and are called pedestal runs.

Pedestal subtraction has to be done for both small and large cells, and, in principle, these two procedures are very similar. The small cells were used for an analysis published earlier and are well understood [8]. The large cells still needed their pedestal determined and subtracted. The event selection for large cell "pedestal events" is 10<sumQ<10000, where sumQ is the sum of the mapped ADC data (excluding pedestal correction) for a large-cell module.

The sumQ condition is then used to sort individual detector ADC distributions. Although they contain collision events, since the large cells are untriggered and their occupancy is small, the sumQ condition above is mostly sensitive to the pedestal, with a small tail from showers in the detectors. The tail effects the Root-Mean-Square (RMS) of the distribution far more than the mean value. The moments of the individual detector ADC distributions are then formed, and the mean charge is equal to the pedestal value for a given channel. There is a possibility that the pedestals are subtracted from the signal on the hardware level. This possibility was not employed until day 121 of the Run 6, after which the pedestals were subtracted automatically.

One important thing to check is the stability of the pedestal and continuity of it at the point where it gets subtracted automatically. To ensure continuity, one can use the LED data in the runs that bridge the boundary where pedestal corrections are enabled in the electronics.

First, the centroids of LED distributions were produced versus the run number for all available data that does not require pedestal correction. This was the first check of the stability of the cell gains which could discover run dependent changes of gains of any other large gain changes. Next, the centroids of LED distributions were produced versus run number for the runs that needed pedestal subtraction. One could check for the continuity of the LED centroid value at the point where the electronic pedestal suppression was introduced. This was done for both calorimeters and example of such a procedure is plotted on figure 4.1.

One can see from this example figure that the pedestals tend to be stable and that the change to electronic pedestal suppression works, based on the continuity of the run dependence. Within each cell are two numbers. The first number is the detector number, and the second number is the run-averaged LED response. Operationally, for each run and for each detector, the average ADC value is computed for LED events. An important feature of figure 4.1 worth mentioning is that the lower the LED centroid value is, the larger the fluctuations will look, as can be seen from the definition of the y-axis. Here μ_{i} represents the mean moment of the ADC distribution for a single channel, while $< \mu >$ is the average mean moment of the ADC distribution for all runs.

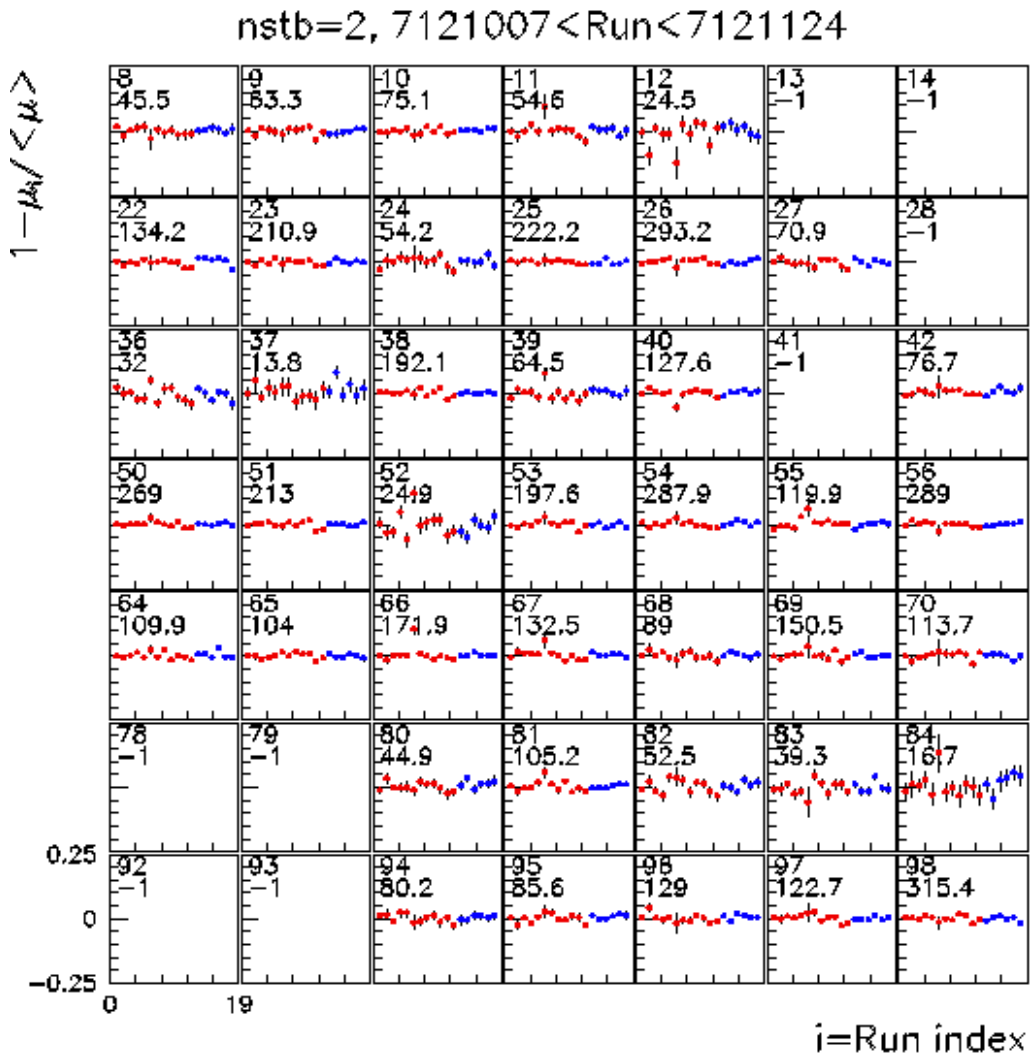

Figure 4.1: Stability of LED centroid values for a part of the calorimeter. Each dot represents a run. The red dots are runs that don't have automatic pedestal subtraction, the blue dots are the ones that do. In all but one case where -1 is present, there are no detectors in that location (four cases correspond to locations for the small cells, three cases correspond to corners of the matrix that were not active detectors by design. There is one example (3^{rd} row from top, 6^{th} column from left) of a missing detector, due to a hole. The value of the run-averages LED response for all runs is written in each cell under the cell number.

Shown here is a part of the calorimeter, for which one can see that the continuity on the red-blue border is satisfied for all cells. In this way, some slow run dependent effects in the data were observed. The run dependent features were found to have multiple sources,

including clouding of the glass for cells closest to the beam, zener diode instabilities and intervals where selected LED pulse generators were not firing. Wherever possible, this effects were corrected for.

After the pedestals and their possible run dependence get determined, they get written in a file and subtracted from the ADC count recorded in the data for each event. This subtraction has to be run dependent since there are two sets of files as mentioned earlier. Also, this gives the possibility to model a pedestal drift or pedestal changes when necessary.

4.4. Detector calibration

4.4.1. Small cell calibration

After the pedestals have been subtracted, a first look at the data can be made. There still remains the issue if what one recorded as the energy deposition in a cell corresponds to reality. Here, cell calibration comes into place. There are different methods one can use to do this, two of which were employed here. Both the small and large cell calibrations were done by reconstructing single π^0 events, but the large cells had the additional step of energy slope matching. The π^0 event method will be described in this section, while the slope matching in the next.

π^0 has a mean lifetime of $\tau = (8.4 \pm 0.6) \cdot 10^{-17}\,\mathrm{s}$, which corresponds to a length of $\approx 10^{-8}\,\mathrm{m}$. So, the highest energy pions, which travel very near the speed of light, will only traverse a length shorter than a micron. This, given the fact that the calorimeters are more than 7 m away from the average interaction point, gives reason to consider the pion decay instantaneous.

The most likely decay channel for a π^0 is to two photons, which is described in detail in the Appendix. The kinematic factors of the decay are also given in the Appendix and give information on the most likely trajectories of the two photons for a forward-decaying pion. To reconstruct a π^0 particle, we have to detect both its daughter photons. One can then

evaluate the mass of the di-photon pair with the help of this formula:

$$M_{\gamma\gamma} = E_{\gamma\gamma}\sqrt{1 - z_{\gamma\gamma}^2}\sin\left(\frac{\phi_{\gamma\gamma}}{2}\right) . \tag{4.1}$$

Here $E_{\gamma\gamma}$ is the summed energy of the two photons, $z_{\gamma\gamma}$ is the energy sharing factor (difference of energies of photons divided by their sum) and $\phi_{\gamma\gamma}$ is the opening angle of the two photons. Several questions come to mind here. First, can this equation be put in a simpler form, i.e. can some of the variables be simplified? Second, what are the exact definitions of the parameters in equation in terms of what the detector records? And third, what cuts on the variables should one impose to extract mostly single pion events with minimal background?

To answer these questions, the knowledge of the geometry of the detector is essential. Since the FPD++ is located far from the interaction point, the sine of the opening angle is small and it can be approximated with the angle itself, which can, in turn, be described in terms of detector variables. The definition of the energy can also be done in several ways: first, one can take the energy of the entire calorimeter to be equal to the energy of the di-photon if it is true that there is no background in the sample. Second, one can take the sum of energy deposited in clusters of cells that correspond to photons, and third, one can take the sum of fitted photon energies. For the small cells, we chose the first option since we basically have no background. For the large cells, we chose the fitted photon energy because it represents the energy of the incoming photon with a higher degree of accuracy across a larger photon energy range. The equation for determining the invariant mass now becomes:

$$M_{\gamma\gamma} \approx E_{\gamma\gamma}^{\text{rec.}}\sqrt{1 - z_{\gamma\gamma}^2}\frac{d_{\gamma\gamma}}{2z_v} , \tag{4.2}$$

where $d_{\gamma\gamma}$ stands for the distance between reconstructed photons and z_v the reconstructed location of the vertex point.

Next, one has to get the reconstructed photon energies. For a detailed analysis of the reconstruction of photon variables, including energy and position, refer to [48]. Basically, the energy recorded in a calorimeter gets separated into clusters (if any), and each cluster

gets split into what is called "category-1", "category-2" or "category-0" event. "Category-1" events are those that (with a high degree of probability) contain a single photon for a single cluster, "category-2" events contain two photons in a single cluster and "category-0" are inconclusive. Two "category-1" clusters represent clearest di-photon events and are the best to use in the calibration of the detector. The calibration procedure now goes as follows:

1. Start with a set of gains = 1 for all towers.
2. Read out an event and find the deposited energy for each tower (cell).
3. From the readout, form clusters and reconstruct possible photons.
4. Select only events that satisfy a certain set of cuts; these were listed in the previous chapter. The specific set of cuts used to calibrate the small cells was:
   - A multiplicity cut not allowing the LED events to enter in the event sample
   - Minimal energy deposited in a single calorimeter module equal to 15 GeV
   - Exactly two reconstructed photons in a small cell module
   - A cut restraining the photons to be within half a cell perimeter in the module
   - Energy sharing between the two photons less than 0.7
   - Invariant mass of the two photons less than 0.7 GeV/c^2
   - The reconstructed vertex point can not be more than 90 cm away from the IP
5. For the two photons determine the invariant mass and associate it with the highest energy tower.
6. After summing through all the runs, determine the new gain via means of iterative procedure; in every next step the gain correction factor is calculated like this:

$$g_{\text{new}} = \frac{m_{\pi^0}}{m_{\text{peak}}} g_{\text{old}} \tag{4.3}$$

7. Iterate the process until the gains stop changing significantly (order of a few percent).

In equation (4.3) there is a variable called m_{peak} which is obtained by an analysis package which fits the distribution of the invariant mass to a predefined function. This is done on a cell-by-cell basis, since each cells has its' own correction factor. The function used to fit the distributions is sum of a Gaussian function, used to describe the neutral pion mass peak, and a generalized gamma function, used to describe the background in the histograms. More specifically, the function is given by:

$$\frac{\mathrm{d}f}{\mathrm{d}m} = \frac{S}{\sigma\sqrt{2\pi}}\exp\left(-\frac{(m-\mu)^2}{2\sigma^2}\right) + B\left(\frac{\beta^2}{t_1 - t_2}\right)(m - m_0)\exp\left(-\beta(m - m_0)\right) , \tag{4.4}$$

where $m_0 = \mu - x_p - 1/\beta$ and t_i result from:

$$t_i = (\beta(m_i - m_0) + 1)\exp\left(-\beta(x_i - x_0)\right) \tag{4.5}$$

by integrating the background term of $\mathrm{d}f/\mathrm{d}m$ for $|m_i - m_0| < 3\sigma$. So, the fit has 6 free parameters, which physically correspond to the following:

- S: Gaussian peak integral
- μ: Gaussian peak centroid
- σ: Gaussian width
- B: integral of the background function for $|m_i - m_0| < 3\sigma$
- x_p: background peak position
- β: background exponential falloff parameter

By making this fit, one can determine the position of the peak for a cell and then proceed to find the new correction factor. This procedure was found to converge fast and 5-10 iterations were more than enough to calibrate the whole detector. Given on figure 4.2 is the plot of the gain correction value vs. iteration number for the WN small cells and on figures 4.3 and 4.4 is the summed invariant mass of the di-photon sample after this set of iterations. One of the cells looks like it is not stable (second row, fourth cell from the left). This cell

(and other similar to it) can be looked at manually to ensure that the di-photon mass peak falls on the value of the π^0 mass peak. The summed result for the WS detector is given in figure 4.5 to demonstrate the goodness of the calibration.

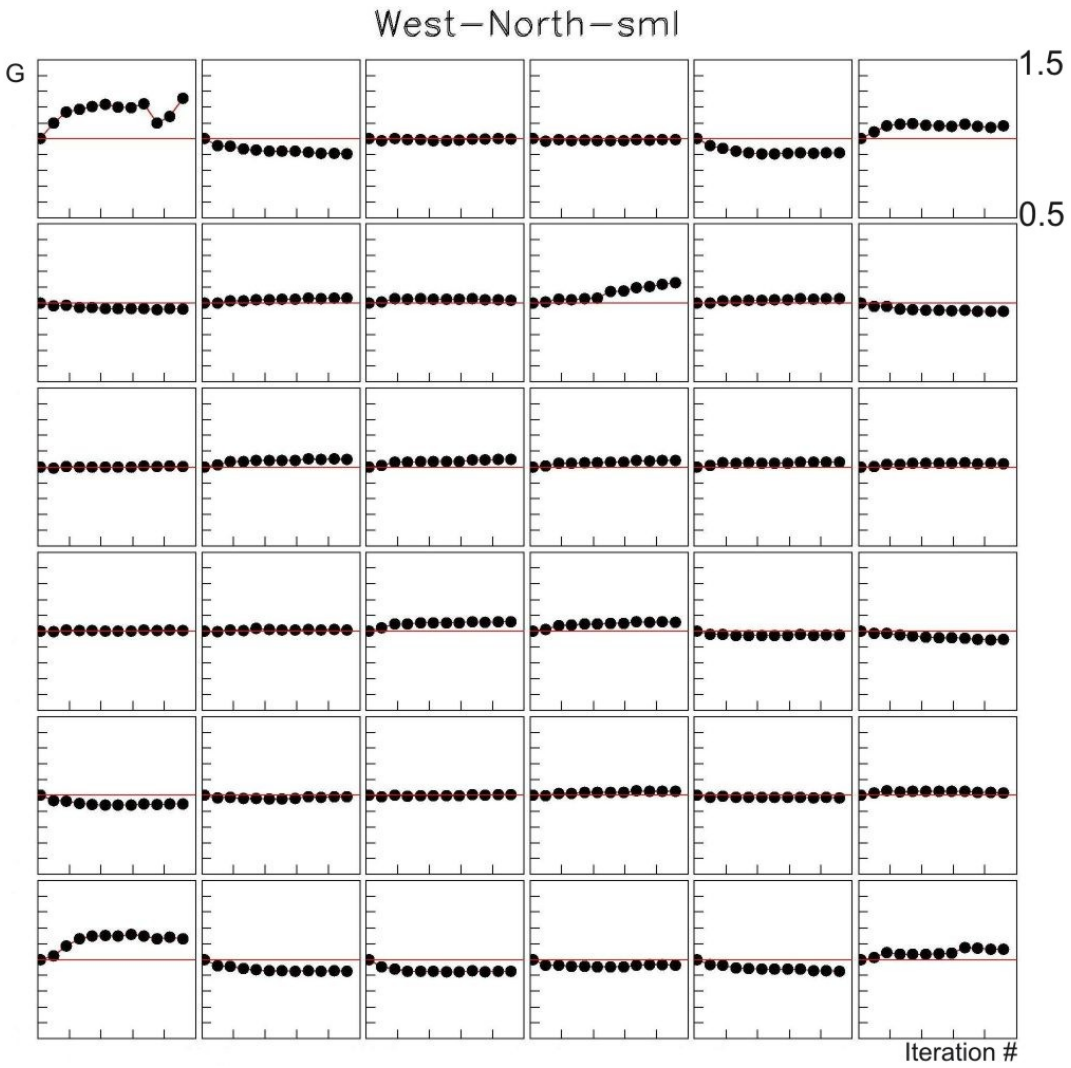

Figure 4.2: Dependence of gain correction factors on the iteration number for the WN small cells. One can note the stable behavior of the correction factors, apart from a single cell in the second row.

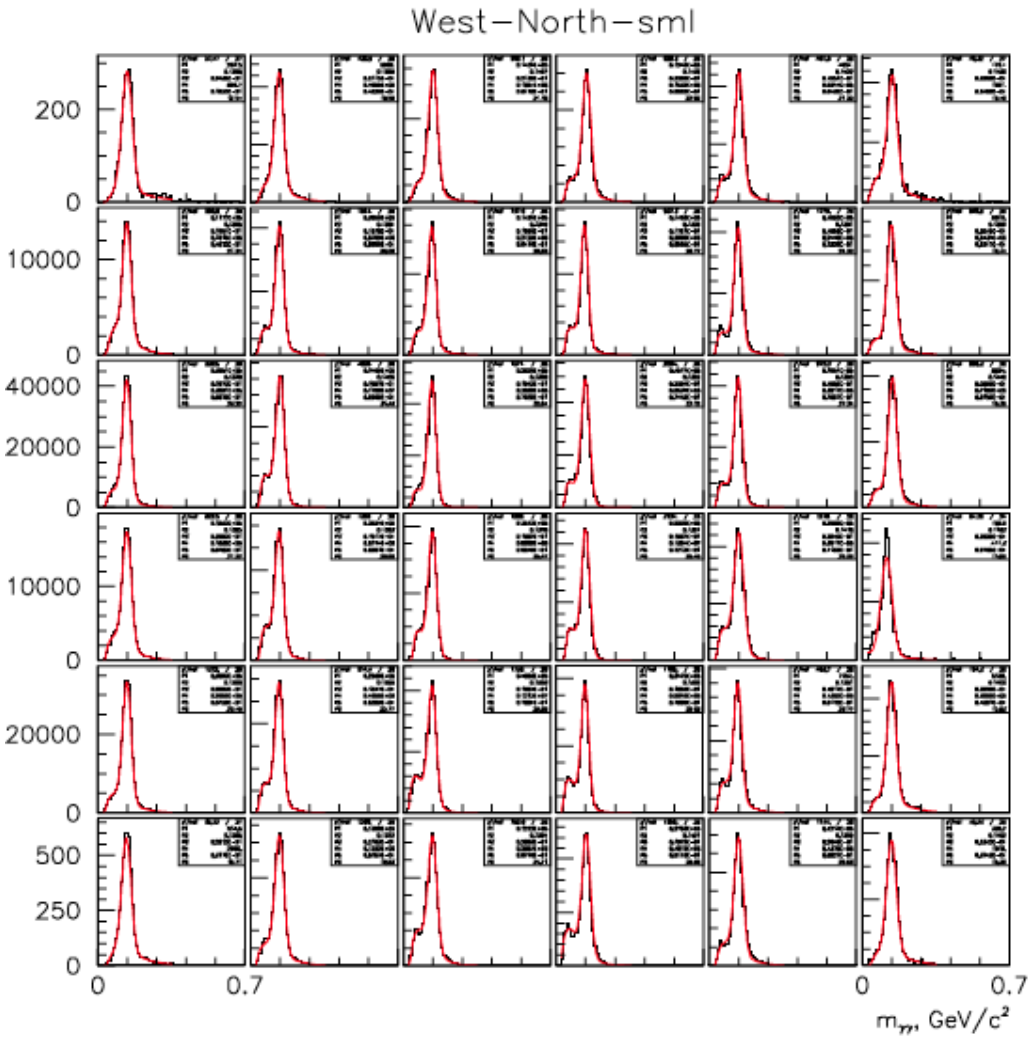

Figure 4.3: Invariant di-photon mass spectra for the calibrated detector. Shown here are the WN small cells in a channel by channel view. For each cell, the fit to the function defined in equation (4.4) is given for each cell with a red curve. The parameters of the fit are also given in the plot and are described in detail in figure 4.4.

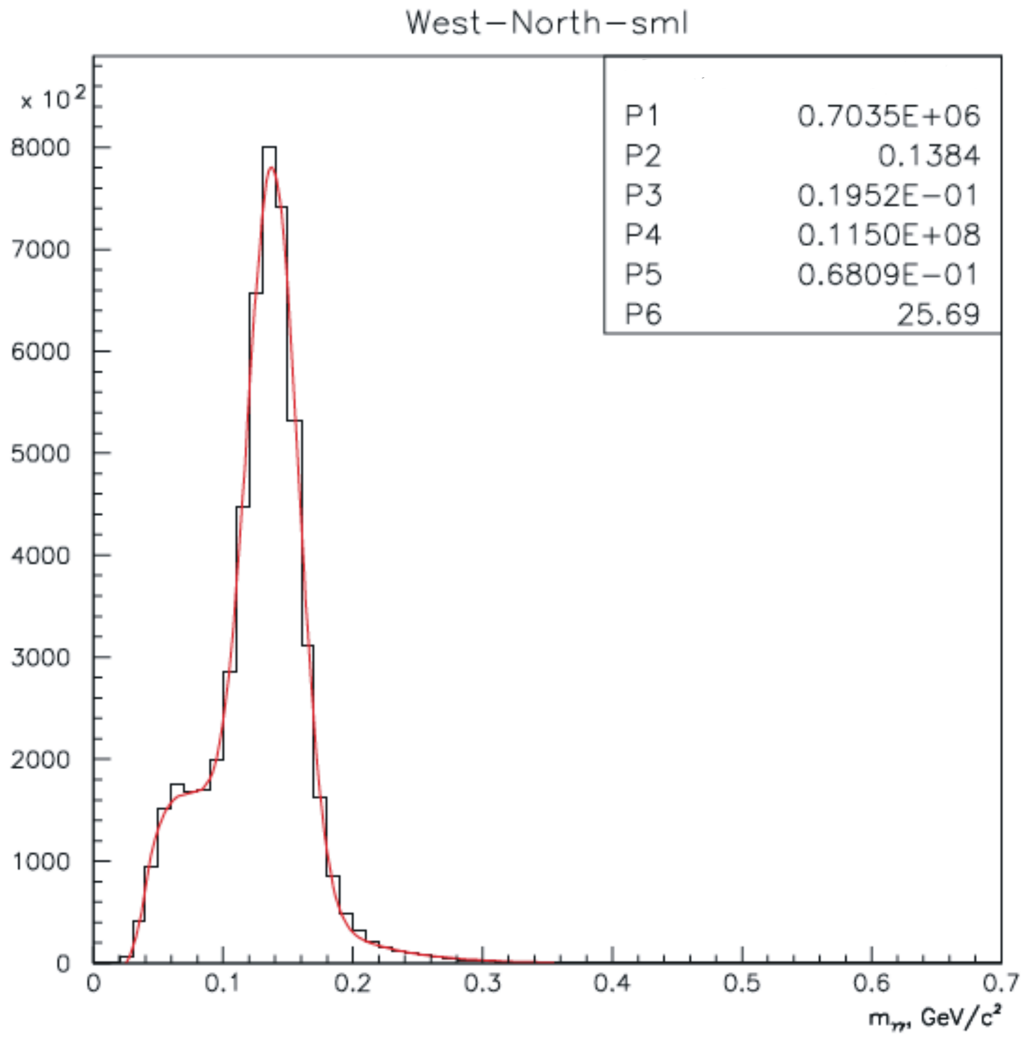

Figure 4.4: Summed invariant di-photon mass spectra for the calibrated detector. Shown here are the WN small cells. On the image, the red curve represents the fitted function of the form as given in equation (4.4). The parameters of the fit are given in the legend; the correspondence of these parameters and the functional parameters is: P1→ S, P2→ μ, P3→ σ, P4→ B, P5→ x_p and P6→ β. One can see that the value of the parameter P2 is equal to 0.1384, which differs from the neutral pion mass by 2%.

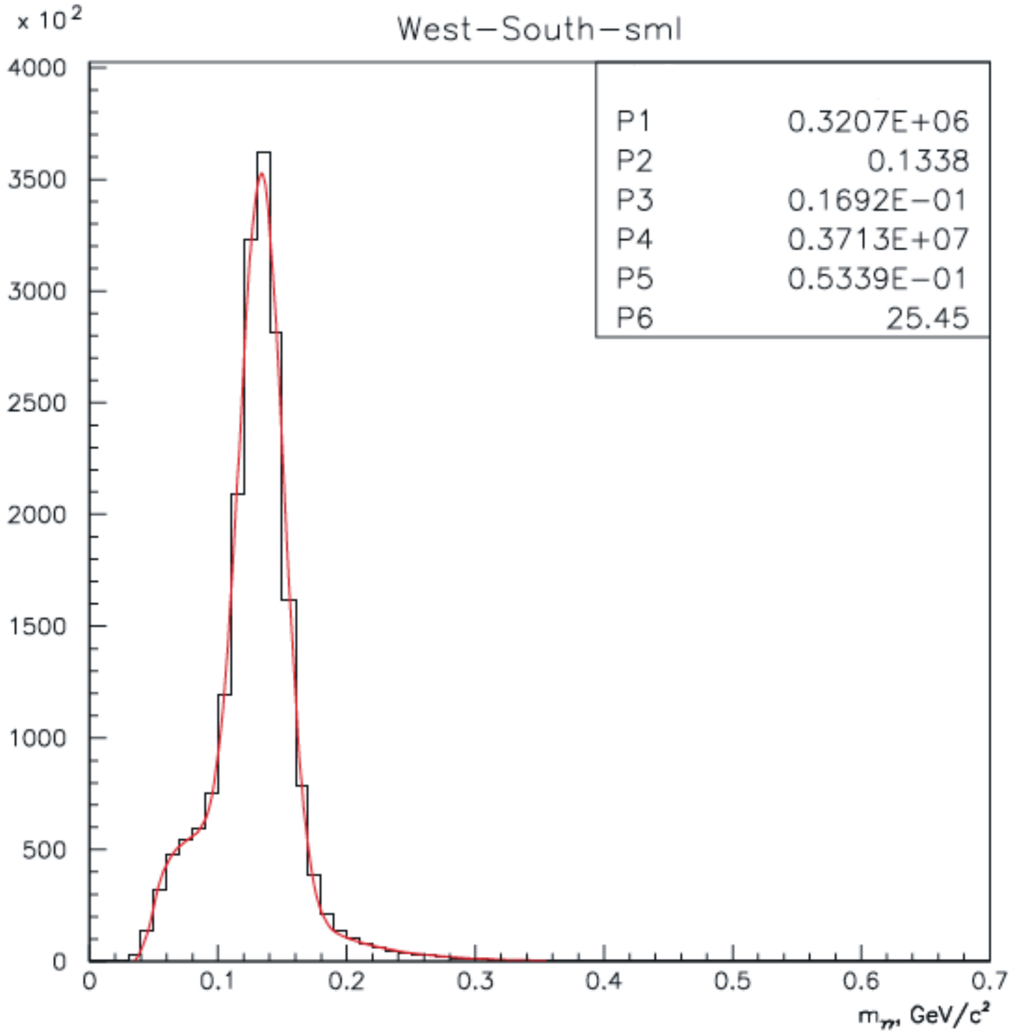

Figure 4.5: Summed invariant di-photon mass spectra for the calibrated detector. Shown here are the WS small cells. The description of the image is identical to figure 4.4. In this case, the parameter P2 is equal to 0.1338, which differs from the neutral pion mass by 0.9%.

4.4.2. Large cell calibration

The calibration of the large cells had to take a significantly different route than what it was for the small cells. The reason for this is simple, and that is that the trigger was set up in such a way that it only recorded an event whenever the ADC sum passed a certain threshold in the small cells, and so, consequently, there were not many events at high energy in the large cells, where neutral pion finding provides the best signal to background ratio. This was not the original intent for the triggering system, but we had to revert to it because the original plan proved to have excessive electronic noise. It is to be expected that a significant amount of energy ends up in the small cells and a small amount in the large cells. This makes the calibration of large cells more difficult since there aren't as many single pion events in the large cells.

There are two more reasons why the large cells prove more difficult. The first is that the gain variation throughout the cell set can be much larger than throughout the small cell set. So, it is difficult to find a good starting point for the gains and the iteration procedure. Second, the large detector is non-hermetic, since it has a "hole" in the middle where the small cells are placed. This will pose an additional fiducial volume cut on the large cells reconstruction.

At the beginning, an iterative procedure via pion reconstruction was planned, with the requirement that one and only one reconstructed photon is in the small cells, the other in the large cells. This would ensure there is enough data in the sample and yet extend the calibration to large cells. This method proved ineffective at the beginning since the photons have small opening angles and the only portion of the large cells that could be calibrated was the one near the inner-outer cells boundary. The result of such a procedure is given in figure 4.6.

One can see that the distributions on the inner-outer cell boundary look reasonable from the standpoint of the shape of the spectra, but they suffer the same problem as the outer parts of the calorimeter and that is lack of statistics. Iterating the gains this way wouldn't prove much worth because of that reason and another step had to be made before it.

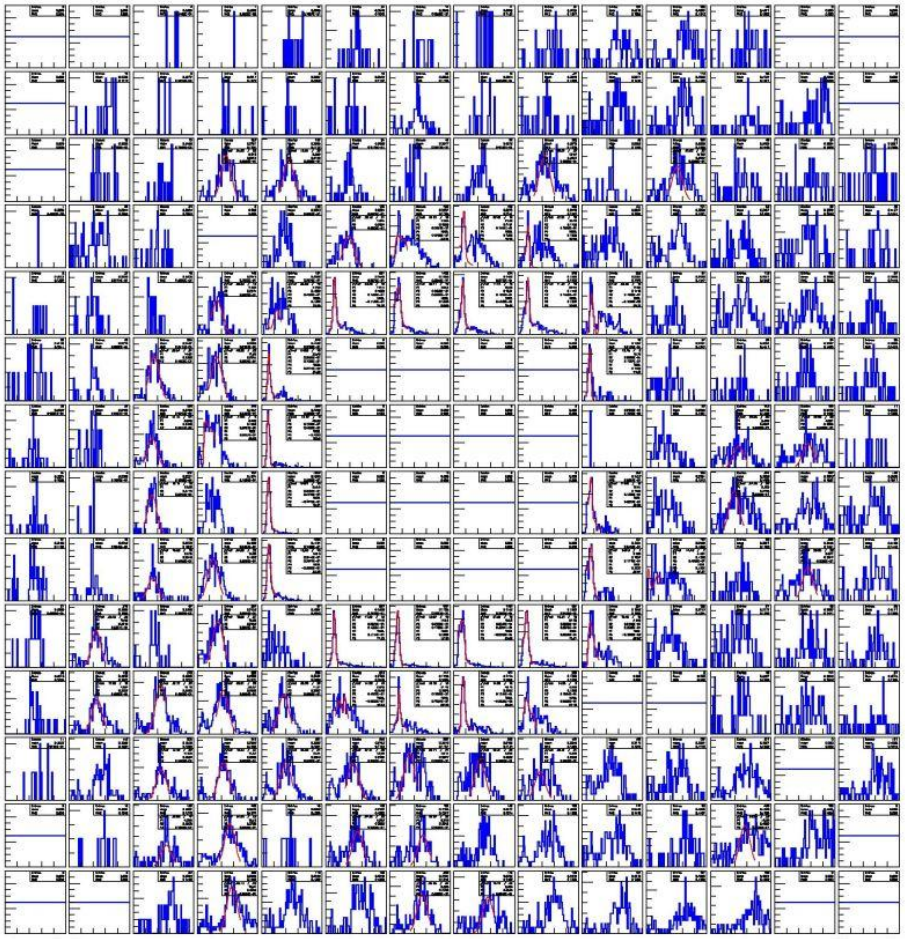

Figure 4.6: Invariant di-photon mass spectra for the north large cells with one photon in small cells. The blue lines are the di-photon mass distributions, the red lines are fits to the pion invariant mass spectra.

There is a benefit to the reconstruction with one photon in the inner calorimeter and one photon in the outer calorimeter. The benefit is to demonstrate that the inner and outer calorimeter data is correlated for each event. That may sound simple, but is not in any way trivial given the electronics used by necessity. Essentially there were two different acquisition systems, which were interlocked by "tokens" (i.e., common data that appeared in the two different acquired data set). The "tokens" were used to "build" the event from the different

acquisition systems. A test of proper event building is the physical correlation between the inner and outer calorimeter, which is there.

At this point, a simulation sample was made representing a perfect calorimeter and event set. The comparison of simulations with data is described in more detail in results. Since the energy deposition in a cell depends only on its relative position in space with respect to the interaction point (provided that we can simulate the pp collisions well), the real detector should have the recorded energy spectra behave similarly to the ideal detector spectra. The most important feature of the spectra to look at is their slope. The further one goes from the beam pipe (interaction point), the more steep the slope should be. A typical slope histogram will show the number of events in an energy bin, i.e. $\mathrm{d}N/\mathrm{d}E$ vs. the deposited energy E. This distribution can be parametrized with a 3 parameter function:

$$N = \frac{N_0}{\left(1 + \frac{E}{E_0}\right)^p}\,, \tag{4.6}$$

where N_0 stands for the number of events with energy going to zero, while E_0 and p are the actual useful fit parameters that give information on the slope. A typical view of one of these histograms, for which N_0=10180, E_0=1.897 and p= 3.6854, is given in figure 4.7.

Correlating the fit parameters directly to the slope proves to be hard. An approximate measure of the slope was determined from the fit function in the following way: points where the values for the number of hits are 100 and 100/e were selected and the distance between them was named Δx. It was visible that Δx depends on the gain correction factor of the cell. A cell was selected from the simulation sample and its gain correction factor was modified on purpose for this study. Basically, by modifying the cell gain factor, one can observe the function $\Delta x(g)$ and then try to invert it to $g(\Delta x)$ to determine the gain from Δx. This procedure can in general be specific on a cell-by-cell basis, so we had to look at more than a couple of random cells. The conclusion was that $\Delta x(g)$ does not show strong dependence on the distance of the cell from the inner calorimeter or from the beam. As far as the gain factor is not too large (i.e. less than 5), the function $\Delta x(g)$ is a linear one. An example of

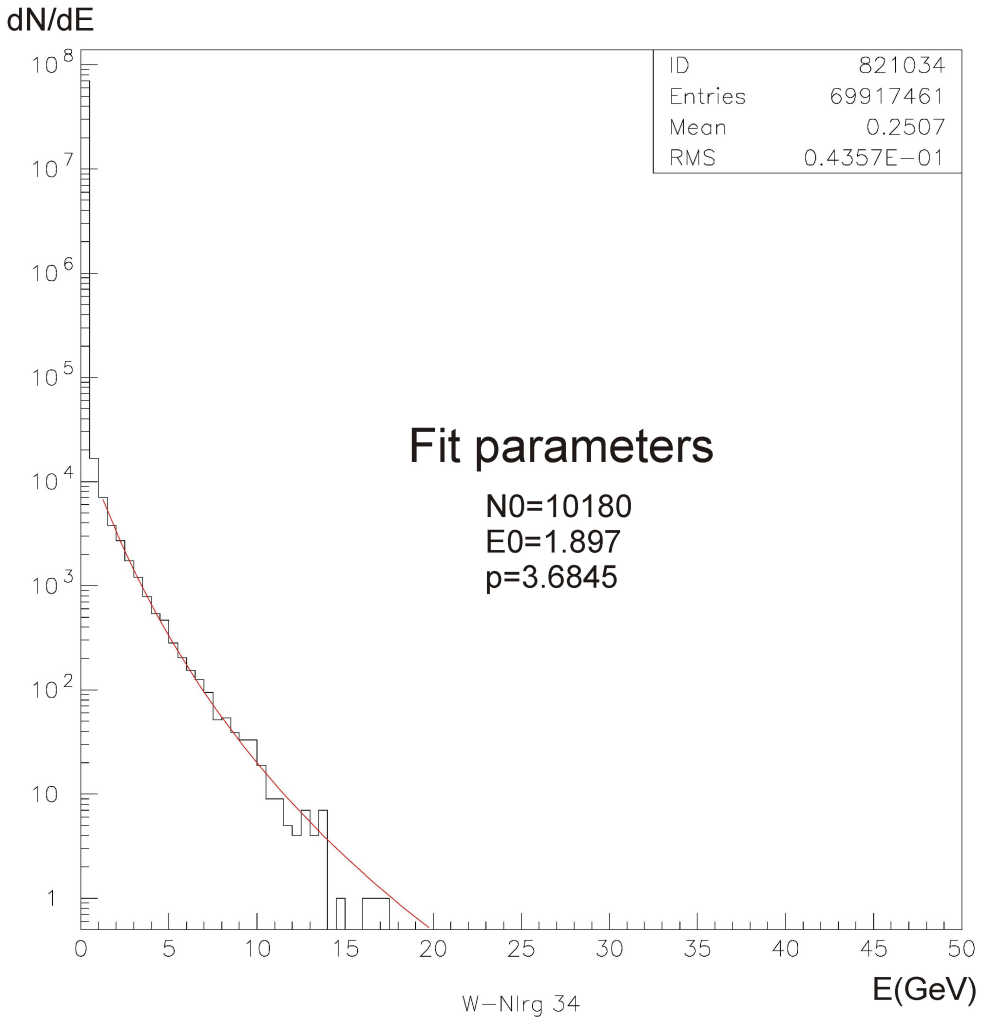

Figure 4.7: A typical view of an energy deposition in a cell. The histogram shows the number of events in an energy bin, i.e. $\mathrm{d}N/\mathrm{d}E$ vs. the deposited energy E. This distribution is parametrized with a 3 parameter function of type: $N = N_0/\left(1+\frac{E}{E_0}\right)^p$, where N_0 stands for the number of events with energy going to zero, while E_0 and p are the actual useful fit parameters that give information on the slope.

this is given in the table:

Correction factor c	Δx(g=c)	$\frac{\Delta x(\text{g=c})}{\Delta x(\text{g=1})}$
0.5	4.5	0.65
0.75	5.6	0.81
1.0	6.9	1
1.5	9.4	1.36
2.0	11.4	1.64
2.25	12.8	1.85

Table 4.1: The dependence of Δx on the correction factor

One can make a linear fit for this cell that gives

$$\frac{\Delta x(\text{g=c})}{\Delta x(\text{g=1})} = 0.68c + 0.31\,. \tag{4.7}$$

A global fit on all the cells will give slightly different parameters, with slope = 0.6 and the intercept point at 0.4. Since Δx(g=1) is known for all cells from simulations and Δx_{data} is known from the data, one can extract the correction factor c. So, a converging iterative procedure was designed to go as follows:

1. For the summed sample of all runs, readout the total deposited energy for each cell.
2. Fit the histograms to a 3 parameter function given above.
3. From the function, determine the points on the x axis where the values are 100 and 100/e, respectively; this will give $\Delta x_{\text{data}} \equiv \Delta x(\text{g=c})$
4. Do the first three steps for the simulation sample as well; this will in turn provide us with the ideal case $\Delta x_{\text{simulations}} \equiv \Delta x(\text{g=1})$
5. From these two values, find the correction factor c
6. Repeat all previous steps

This procedure proved to iterate quickly and was used to get the initial gain correction factors. It is important to note that this calibration can only serve as an initial "rough" estimate for calibration. There are at least three reasons for that:

- The 3 parameter fit will try to fit the energy deposition distribution for each cell over the entire range of energies, whereas the calibration will use only a part of this range. The global fit can put more weight to parts of distribution other than those used for calibration in order to make a better fit.

- Defining the slope as the slope of a line that approximates the segment of the fit can lead to errors in the correction factors. This is due to the fact that the length of the segment can be different for different cells.

- For a fraction of cells, the slope gets calculated for values that are close to the pedestal values for those cells. Pedestal fluctuations throughout the dataset can lead to errors in the calculation of correction factors.

The estimate is that these effects can combine to give up to 10-20% error on the correction factors. So, it is to be expected that this calibration procedure won't improve the correction factors much after the average relative difference of slopes in the data and simulations falls below 15%. After 4 iterations this limit was reached and the initial correction factors were available. At this point we looked at two distributions for both data and simulations: first the energy deposition histograms throughout the detectors, shown for data in figure 4.8, and second, the invariant di-photon mass results with the condition that one photon is reconstructed in the inner cells and one in the outer cells. Both of these distributions match well in simulations and data, so this ensured us that the initial set of correction factors was good.

Likely the best way to view the accuracy of the calibration is the following: define the slope "S" as the ratio of difference of y values (here 100-100/e) over the difference of x values (here Δx). This quantity can be calculated in the data and in the simulations and relative differences in the slopes can be found on a cell-by-cell basis. This distribution can be viewed in two ways; one as a correlation of slopes in the data and the simulations, and the other as the cell-by-cell view of the relative difference. These are both given in figures 4.9 and 4.10 for WN.

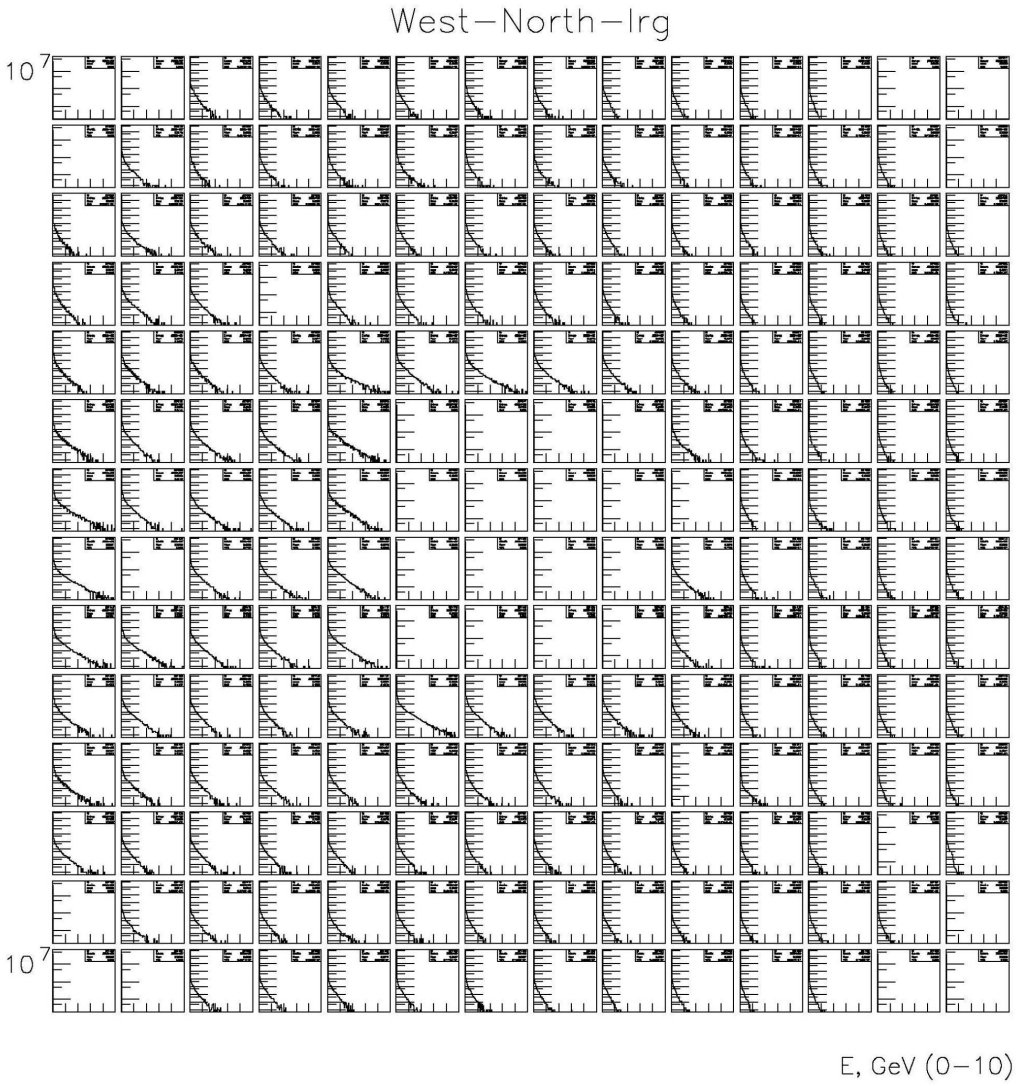

Figure 4.8: WN Cell-by-cell view of the energy deposition for the WN detector in the data after initial calibrations. The beam pipe is placed left of this figure and one can note how the slopes of the distribution become steeper the further one goes from the pipe. The normalization in this figure is not important for the result.

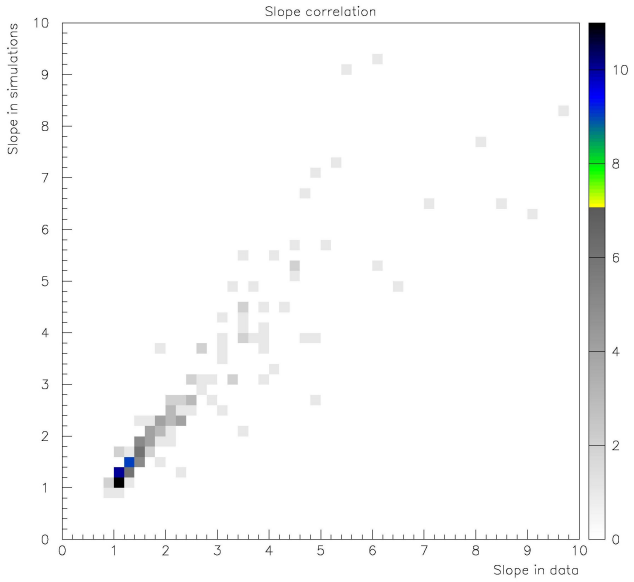

Figure 4.9: The correlation of slopes in the data and in the simulations after initial calibrations for WN. Ideally, this would be described with a line given by $y = x$. Here, best fit gives $y = 1.06x$. The correlation factor of this set is 0.95.

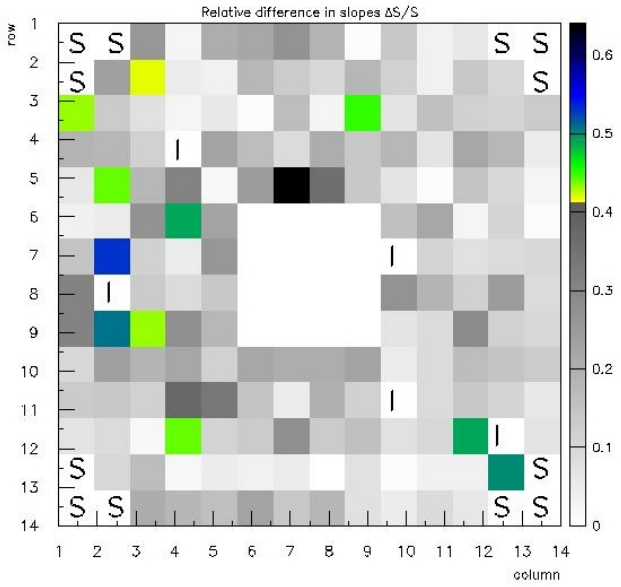

Figure 4.10: WN Cell-by-cell view of the relative difference of slopes in the data and in the simulations. The average difference over all cells is 14%. The "S" symbols in this figure mark spacers and the "I" symbols mark inactive cells.

Some of the cells from figure 4.10 look as if they are not calibrated well at all. This is mostly so because of the definition of the slope and a close visual inspection will show that the distributions look almost identical in the data and simulations. To demonstrate that, one of the cells (WN 114, row 9, column 2 on figure 4.10) was selected and the results of the calibration are given here. In 4.10, the calculated difference of slopes equals around 50%. On figure 4.11 is given an overlay of data and simulations before any calibration. In this figure, the simulated deposition has the gentler slope. On figure 4.12 is given the same overlay after the calibration procedure. On both figures, the red lines are the fitted energy deposition functions. It is clearly visible that even though the slope difference calculation gives a difference of slopes of 50%, this does not arise from bad calibration, but likely from the definition of the slope.

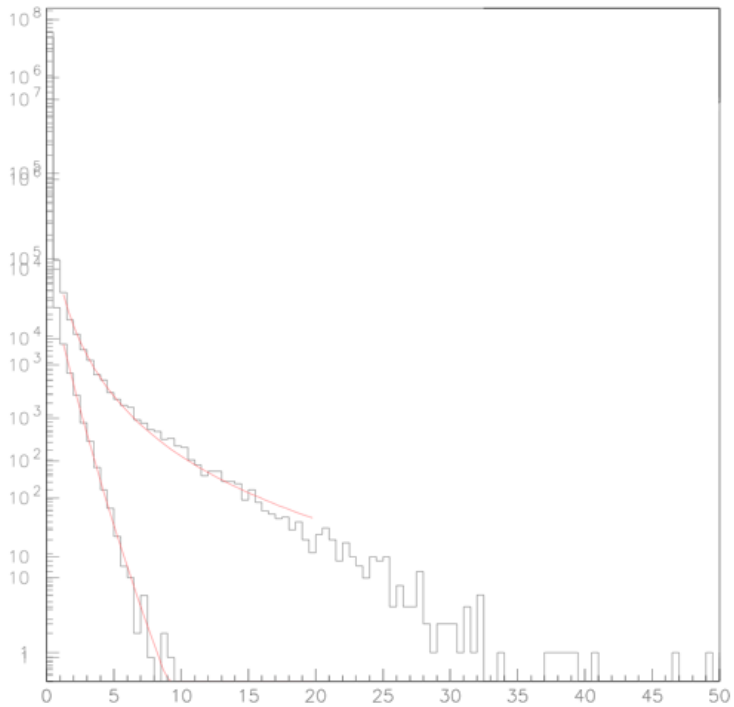

Figure 4.11: WN Cell 114 view of the energy deposition in data and simulations before calibrations. The simulated response is the one with the gentler slope. The red lines are the fitted energy deposition functions. One can see a big difference in the shapes of the functions in data and simulations.

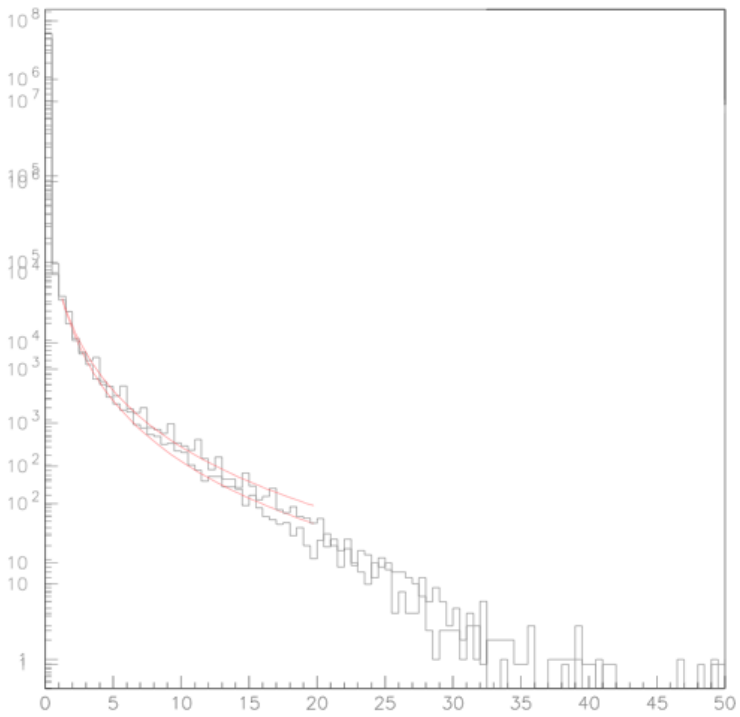

Figure 4.12: The red lines are the fitted energy deposition functions. One can see that the shapes of the functions in data and simulations are almost equal. Calculation shows that the difference of slopes is $\approx 50\%$. This fact can not arise from calibration, but likely from the definition of slope.

Still, there were several cells in both WN and WS that proved hard to calibrate in this way. This was either because of one of the reasons listed above or simply because more iterations were needed. The fraction of the cells that needed more iterations was on the order of 2%. It was concluded not worth while to make their calibration factors more precise since they were expected to get calibrated well in the di-photon calibration procedure.

After obtaining the initial correction factors, we proceeded to calibrate the detector by means of di-photon events. This was still a partially unexplored area since it was the first time a detector was trying to get calibrated that did not serve as a trigger. Background and reconstruction efficiency were a concern and guidance from the simulations was again needed. The set of cuts used for the calibration was very similar to that for the calibration of small cells, with a single difference: the minimal energy deposited in a single calorimeter module

was varied to ensure enough events for calibration, but to avoid too much background. This cut was set to 7 GeV.

The procedure used was the same iterative procedure used for the small cells. Again, the procedure was found to converge fast and after 5 iterations most of the detector has shown di-photon mass peaks at the position of the π^0 mass. This is illustrated in figure 4.13.

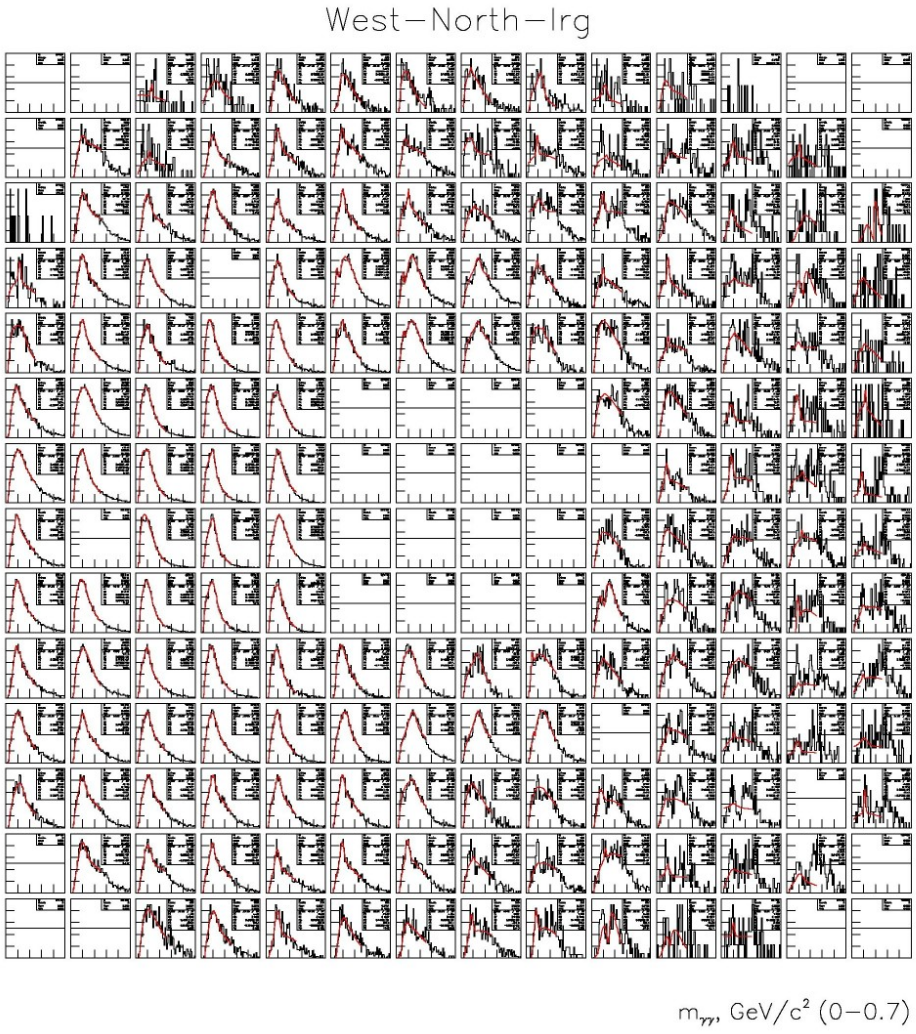

Figure 4.13: WN Cell-by-cell view of the invariant di-photon mass in the data after 5 iterations. The beam is placed to the left of this figure. One can see how the number events decreases as one moves away from the beam, making the di-photon mass distributions less populated in the cells on the right.

There were several issues still to deal with here. One of them was the low population of cells far from the beam and the other was the signal-to-background ratio in the cells. To investigate both of these, we looked in the simulation sample. One thing that is of crucial importance is to have the simulations mimic the data trigger in the best possible way. This was done in the following way:

1. For each simulation event, the energy deposited in the detectors was read out on a cell-by-cell basis.

2. For each detector, a random number in units of GeV was added simulating the noise in the data. The random number was a product of three factors:

   (a) the width of the pedestal, derived for the entire module using summed channel distributions and dividing by $\sqrt{N}$, where N is the number of entries,

   (b) the average energy deposition per ADC count; separately for each detector, and

   (c) a random Gaussian number with a mean value of 0 and a sigma of 1.

   At times, the first of these factors was used as a free parameter since, in general, the width of the pedestal is different for different runs. This freedom allowed to explore the influence of noise on the simulation sample results.

3. The energy is then converted to ADC counts. The conversion factor is equal to the corrected gain factor for each cell and is fed in the simulations from the data, ensuring the same trigger as the data had. The ADC count gets rounded to the closest integer lower in value than the calculated real ADC count.

4. If the ADC value for a channel is found to be negative, it gets reset to zero. The ADC counts then get summed for each module.

5. Now, a software trigger mimicking the hardware trigger is imposed: an event gets analyzed only if the summed ADC value passes the threshold of 75 counts either in WN small cell module or WS small cell module.

6. If an event passes the trigger, the energy for each cell is calculated back from the ADC count for that cell. If the event didn't pass the trigger, the energy for all cells is set to zero.

7. After this procedure, the event is treated further as a normal data event.

This simulation trigger was used in all the later analyses as well. As far as the signal-to-background ratio is concerned, the simulations show somewhat better resolution than the data if there is no noise added into them. Setting the noise equal to 1 average ADC click per event, the data and simulations have shown comparable signal-to-background ratios. There are other real detector effects, like run dependent pedestals, that are not in the simulations and that also contribute to background, so one can expect more background in the data than in the simulations.

The channels that were less populated got calibrated with 4 more iterations of the calibration procedure, but with the deposited energy in the module cut now set to 4 GeV. This practically doubled the statistics in all the channels and the ones further from the beam were populated enough to get calibrated. It turns out that the correction factors for the cells further from the beam didn't need much change, since they were calibrated well in the first calibration step. The stability of the correction factors can be seen from figure 4.14.

By looking at figure 4.14, one can see that about 98% of the correction factors are stable. The few outliers that were in need of attention did not go through further iteration procedure, since that is very time consuming. Instead, they had their correction factors set manually in such a way that the di-photon mass peak would fall as close as possible to the position of the π^0 mass value.

The estimate is that the calibration factors for large cells are determined at the level of 5-10%. The reason to believe this is so is that they were at the level of 15% after the energy deposition slopes calibration and they have significantly improved with the neutral pion calibration.

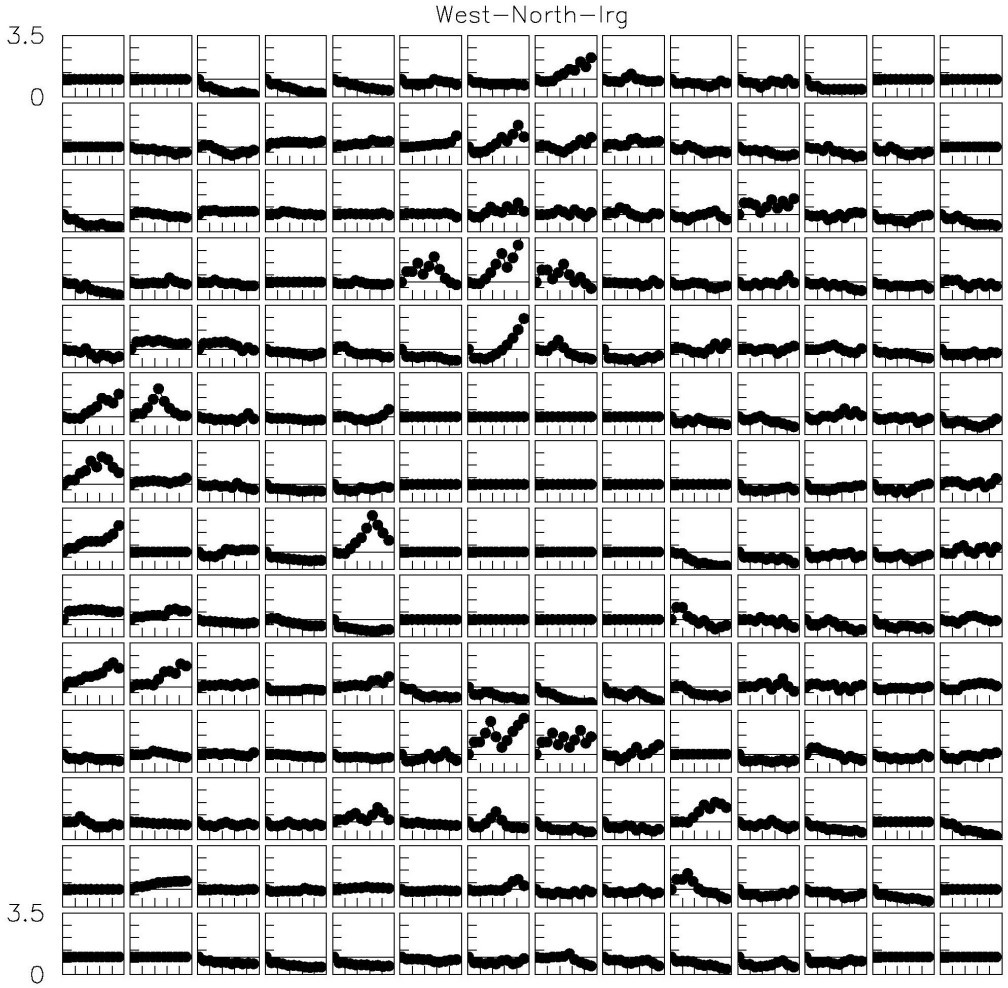

Figure 4.14: WN Cell-by-cell view of the correction factors after 9 iterations. The zeroth value on this plot is the value obtained with the energy slope calibration. Each next dot represents the new correction factor divided with the zeroth value of the correction factor.

4.4.3. The energy dependent and run dependent correction factors

The calibration procedure was at this point done for the event sample that extends through all the possible reconstructed di-photon energies and all the runs in the sample. One thing that still needed investigation is to look if the reconstructed di-photon invariant masses, used for calibration, show any dependences on the run number, fill number or the summed energy of the di-photon event. The energy dependence arises naturally due to the photon reconstruction algorithm [48]. The shower fit for the photons used for reconstruction does not completely account for transverse and longitudinal shower profiles at all energies and causes the reconstructed di-photon invariant mass to be energy dependent. There could possibly be other reasons to energy dependence connected to the photomultipliers. In general, the photomultipliers can have different gains and/or efficiencies for different incoming energies or the rate of incoming energy (luminosity). This is also a reason to see if the correction factors depend on run/fill number, since luminosity generally differs on a run by run basis.

The energy and run dependence was checked for the inner cells only. These cells serve as trigger and their correction factors are important for both analyses. The large cells only enter the multiphoton analysis where detector energies, rather than reconstructed photon energies, enter into calculations, so energy dependence is not as important. Further, since the large cells are not calibrated as well as the small cells, the energy and run dependent corrections won't account for any observable change in results.

The energy dependent corrections were determined from the fits in six energy bins; these are given by 20-25-30-35-40-45-50 GeV. The fits for these bins are shown in figure 4.15. From the fits one can clearly see how the position of the invariant mass of the reconstructed neutral pion rises with energy. So, the centroids of the fit are easily described as a function of the average energy of a given energy bin. Application of energy-dependent corrections can be done in the following way: the energy dependence can be described by means of a polynomial fit function:

$$E_{\text{real}} = E(\beta E + \gamma)\,, \tag{4.8}$$

where E is a shorthand for the recorded energy. After making corrections, in all the energy

bins one reconstructs the correct average neutral pion energy, as can be seen on figure 4.16.

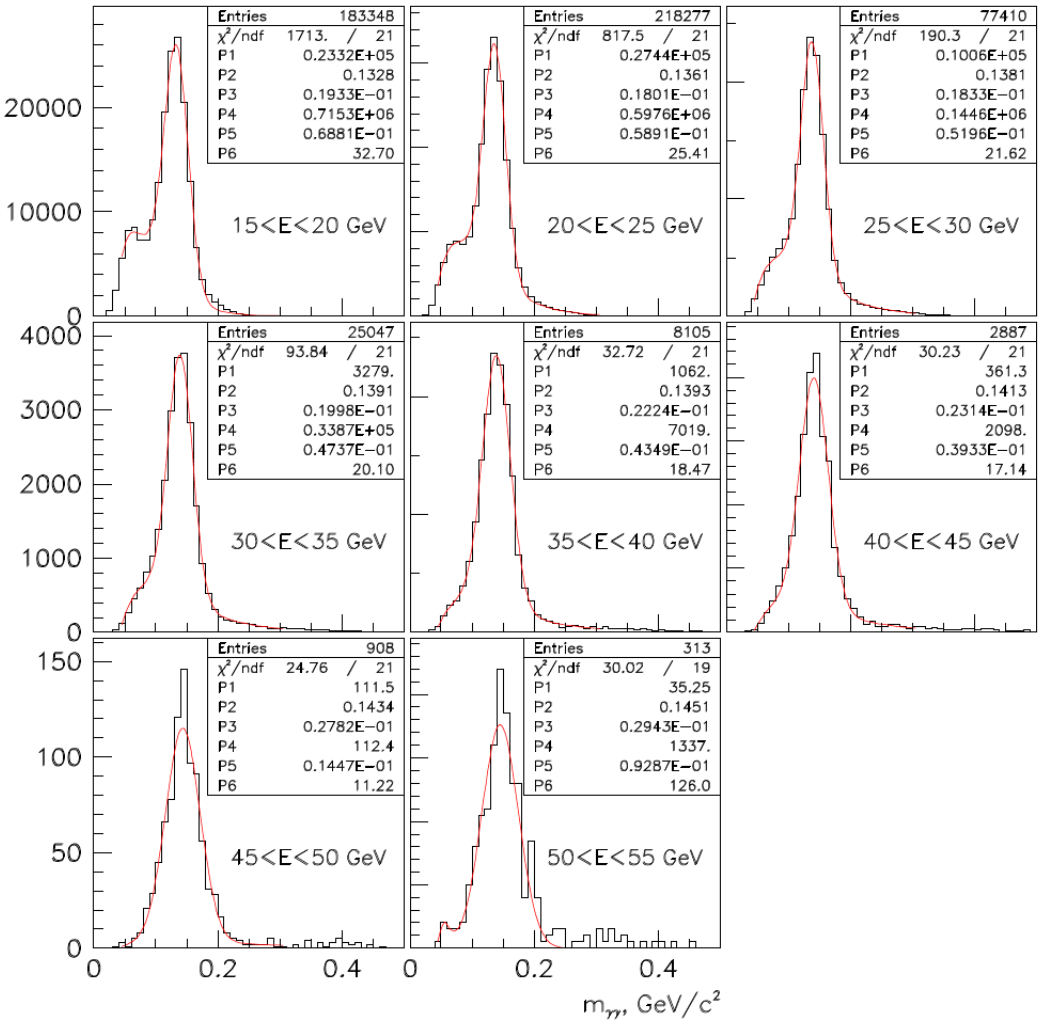

Figure 4.15: The position of the π^0 peak in the invariant mass distributions binned in π^0 energy bins before applied energy dependent corrections. One can see that as the average energy of the bin increases, so does the reconstructed position of the peak of the π^0 invariant mass.

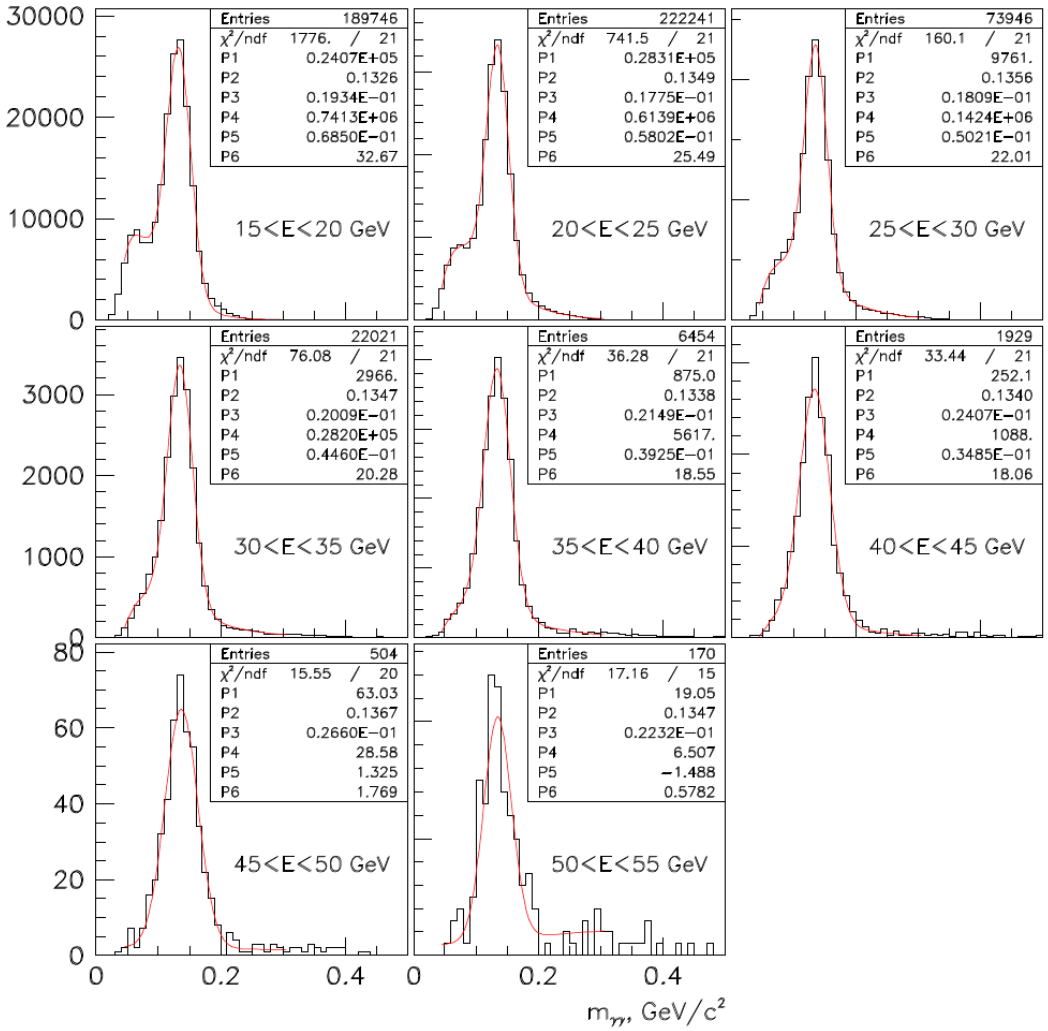

Figure 4.16: The position of the π^0 peak in the invariant mass distributions binned in π^0 energy bins after applied energy dependent corrections. One can see that in all the energy bins the position of the peak of the π^0 invariant mass is reconstructed at the π^0 mass.

To determine the run dependence, the invariant mass distribution for reconstructed diphoton events is analyzed in a similar fashion to how the gains were determined. For the run dependence, the analysis is done for all runs that have >600 events satisfying all acceptance cuts. The average value (P0) of the ratio of the π^0 mass to the fitted peak of the diphoton invariant mass from three corrected energy bins (bin 1: 20-25 GeV; bin 2: 25-30 GeV; bin 3: 30-35 GeV) for each run having sufficient statistics is calculated. Figure 4.17 shows this dependence on a segment of runs.

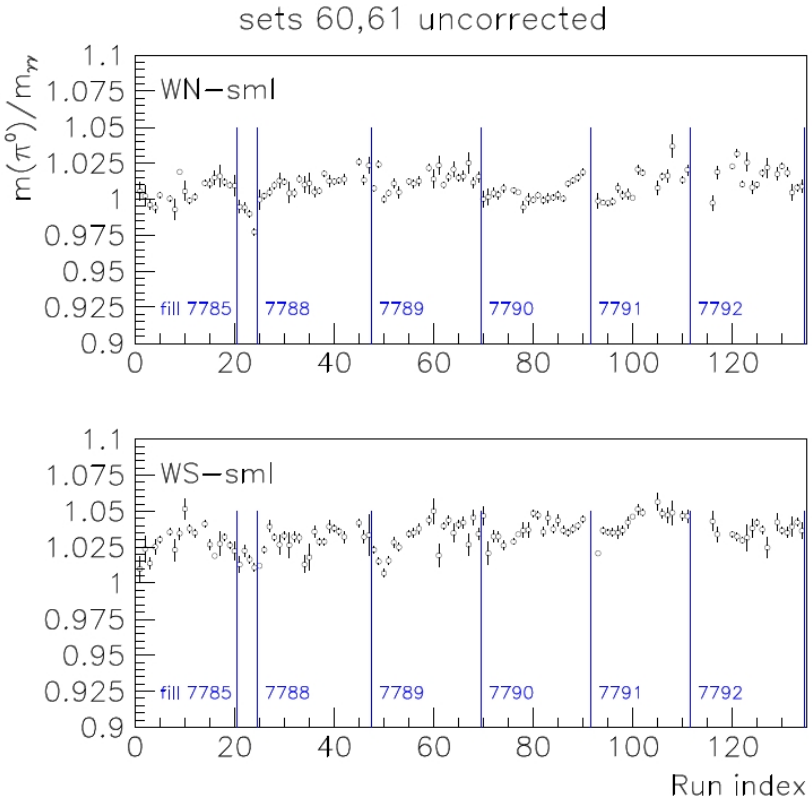

Figure 4.17: The dependence of the reconstructed value of the mass peak on the run/fill number.

From this image, one can see clear evidence of run dependence. The gain correction factors are modified and made run dependent to correct for this effect. For each run, the correction factor is simply the inverse value of the point on figure 4.17. This concludes the calibration of the detector.

4.4.4. Cross sections at large rapidity

The invariant cross section for a given process is an important observable to help establish and understand the origin of particle production. At low collision energies, such as $\sqrt{s} = 20\,\text{GeV}$, it is generally believed that large rapidity particle production arises from soft processes collectively known as beam fragmentation. NLO pQCD calculations at $\sqrt{s} = 20\,\text{GeV}$ underpredict measured cross sections for pion production in this kinematical area by almost an order of magnitude [49].

In STAR, a prototype Forward Pion Detector was used for measurements of large x_F π^0 production cross sections in the first polarized proton collision run at RHIC [50]. The results of the measurement are given in figure 4.18. The data are compared with NLO pQCD calculations evaluated with the CTEQ6M parton distribution functions and equal renormalization and factorization scales set to p_T. The agreement between the NLO pQCD calculation and the data is comparable to what is observed at mid-rapidity. Even though the transverse momenta are small, the agreement suggests that particle production at large rapidity in p+p collisions at $\sqrt{s} = 200\,\text{GeV}$ is dominated by partonic scattering, rather than soft mechanisms presumed responsible for beam fragmentation.

Furthermore, in addition to agreeing with the theory, the measured π^0 production cross sections at high pseudorapidities agree with results from the PYTHIA generator as well, as shown in figure 4.19. Hence, it is possible to claim that we understand particle production in this kinematical area at $\sqrt{s} = 200\,\text{GeV}$ and that it can be described well by both NLO pQCD and simulated well in PYTHIA.

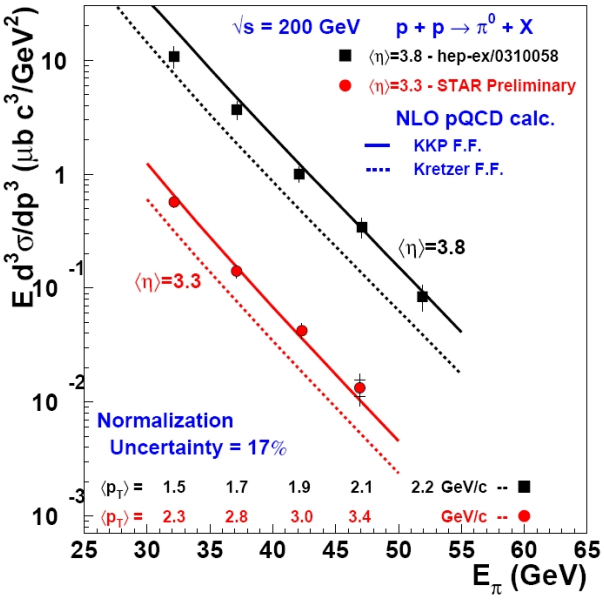

Figure 4.18: Measured invariant cross section for π^0 production in pp collisions at high pseudorapidities at $\sqrt{s} = 200\,\text{GeV}$. Shown in the image are two theoretical sets of fragmentation functions.

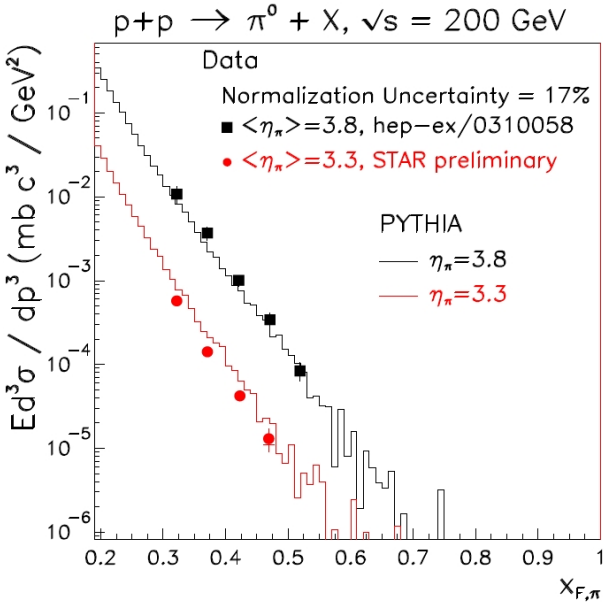

Figure 4.19: Measured invariant cross section for π^0 production in pp collisions at high pseudorapidities at $\sqrt{s} = 200\,\text{GeV}$ compared to PYTHIA prediction.

4.4.5. The neutral pion analysis

The analysis of the π^0 events can immediately be done after the calibration of the detector. This is so because the same event selection applies to the π^0 analysis as to the calibration procedure. The π^0 analysis was published independently of this work [8] and used the data from the small cells only. The steps of the analysis include spinsorting the data and calculating the cross ratio asymmetry. At last, the final result can get binned in pion energy and transverse momentum bins.

The spinsorting of the data uses the same neutral pion cuts as the calibration procedure. In addition, the bit describing the spins of the colliding protons is read in and the data is sorted by spin bits. The variable that gets sorted is the calculated invariant mass of the di-photon and the binning is done in the energy of the di-photon event. With these variables and the reconstructed position of the event, one can also find the transverse momentum of the di-photon and separately bin the results in p_T.

In the end, the asymmetry gets calculated for this sample of events. If one looks at, for example, equation (2.5), one can see that the spin information for only one of the incoming protons is required. So, the spin information of the other proton gets integrated over and one can make the asymmetry calculation. For the published result, the asymmetry was calculated and binned in x_F and p_T bins. These two quantities are correlated, which can be seen from the event locus, plotted in figure 4.20.

There is a strong correlation between x_F and p_T at a single pseudorapidity. The asymmetry was calculated and binned in x_F, as well as in p_T. The results of this analysis will be given in the next chapter.

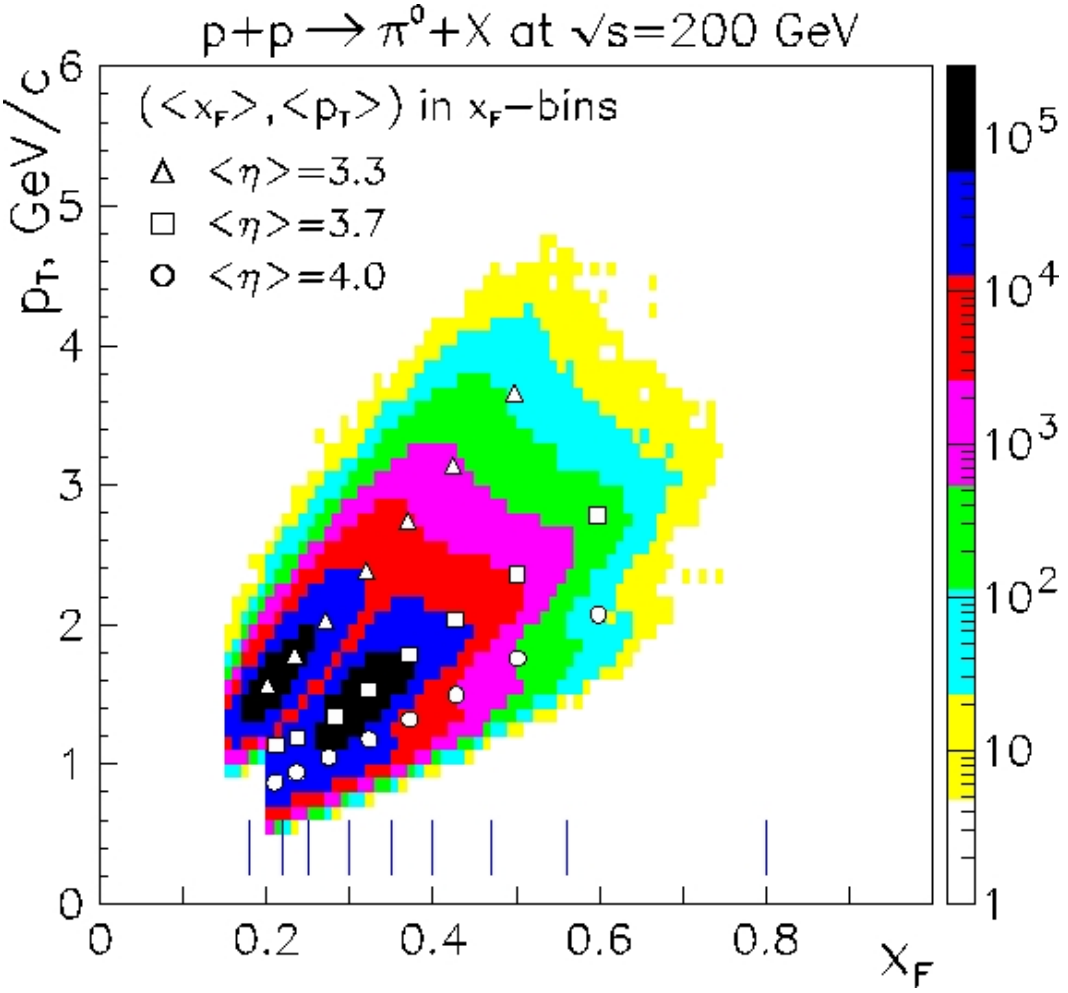

Figure 4.20: Event locus showing the $x_F - p_T$ correlation. Plotted in this figure are events for both west ($\eta = 3.3$) and east detectors (not described in this work). Bins in x_F are indicated by vertical lines.

4.5. Definition of multiphoton events

Looking only at the inclusive neutral pion production, one can not disentangle the Collins / Sivers contributions to the asymmetry. One could isolate contributions from the Sivers effect by looking at direct photons or jets, since these particles are produced in hard scattering. So, an event selection was made to extract "jet-like" events from the sample. These are, naturally, not full jets, since the jet-like response of the FPD++ emphasizes the electromagnetic part of the jet. This won't precisely determine the jet energy, but will reconstruct it's direction, as discussed below, well enough. We will call these events "multiphoton" events.

The multiphoton event finder algorithm then goes as follows:

1. For a single calorimeter, events are considered if the inner module summed energy passes the minimum threshold energy, set to 23 GeV, to avoid events that are near the hardware threshold.

2. Further, an event is required to contain data in the outer module and for it not to be an LED event; the first of these conditions can be imposed by reading in a bit that is non-zero if the large cell readout is "live". The second condition is imposed by an energy cut: $E_{\text{summed}}^{\text{inner+outer}} < 80\,\text{GeV}$.

3. The cells in the detector are read out. If a cell contains more than 0.4 GeV of energy, it is considered by the multiphoton clustering. It is required that there are at least 4 cells that satisfy this in order for the finder to continue. The energy of the multiphoton is now defined as the sum of energies of the cells in it. The p_T of the event is the average p_T of all the towers.

4. After this, the finder is run. The finder takes all the cells passed on to it and imposes the following set of cuts:

   (a) minimum weighted sum of towers; small towers have a weight of 1, large a weight of 1.52632 (ratio of side lengths of the large/small cells). The cut is set to 10.

   (b) maximum number of towers in an event, constrained to avoid too large combinatorial factors.

(c) minimum p_T of the event, set to 1.5 GeV/c.

(d) minimum energy of the event, set to 20 GeV and

(e) maximum cone size of the event in the $\eta - \phi$ space, set to 0.5.

5. If the initial set of cells satisfies all of these conditions, it is taken to be the final multiphoton event. If not, a single cell is taken out of the sample (in all possible combinations) and the finder is run again. The procedure is continued until the finder finds a satisfying event or no event at all.

6. At this point, all the kinematical factors, such as p_T, the direction of the multiphoton axis, the angles with respect to the interaction point etc., of the event are calculated.

7. Finally, a 2 (large cell) perimeter fiducial volume cut is put on the multiphoton intercept point. This is the point where the multiphoton axis intercepts the calorimeter face.

8. In the end, the physical variables for the event are calculated. These include the energy, momentum and the invariant mass. Since cell-by-cell information is available, one can also look at the multiphoton energy profile, i.e. the fraction of energy that gets deposited at a fixed distance from the axis as well as at a fixed angle around the axis. The first observation will give the "multiphoton energy profile".

The code is run through both data and simulations with the data mimic trigger. The simulation sample serves as a check on all the unpolarized quantities to see if we understand the data sample and if there are any significant issues in the data. Even though the simulation sample is limited in statistics, the unpolarized data results show great resemblance to the simulation results. With this "jet-like" event finder and the trigger used during Run 6 over 10^6 multiphoton events are found in the data, which is a great statistical example to study. The locus of events summed over all runs and both modules, along with the geometrical acceptance of the inner modules (averaged over the N and S detectors), is given on figure 4.21.

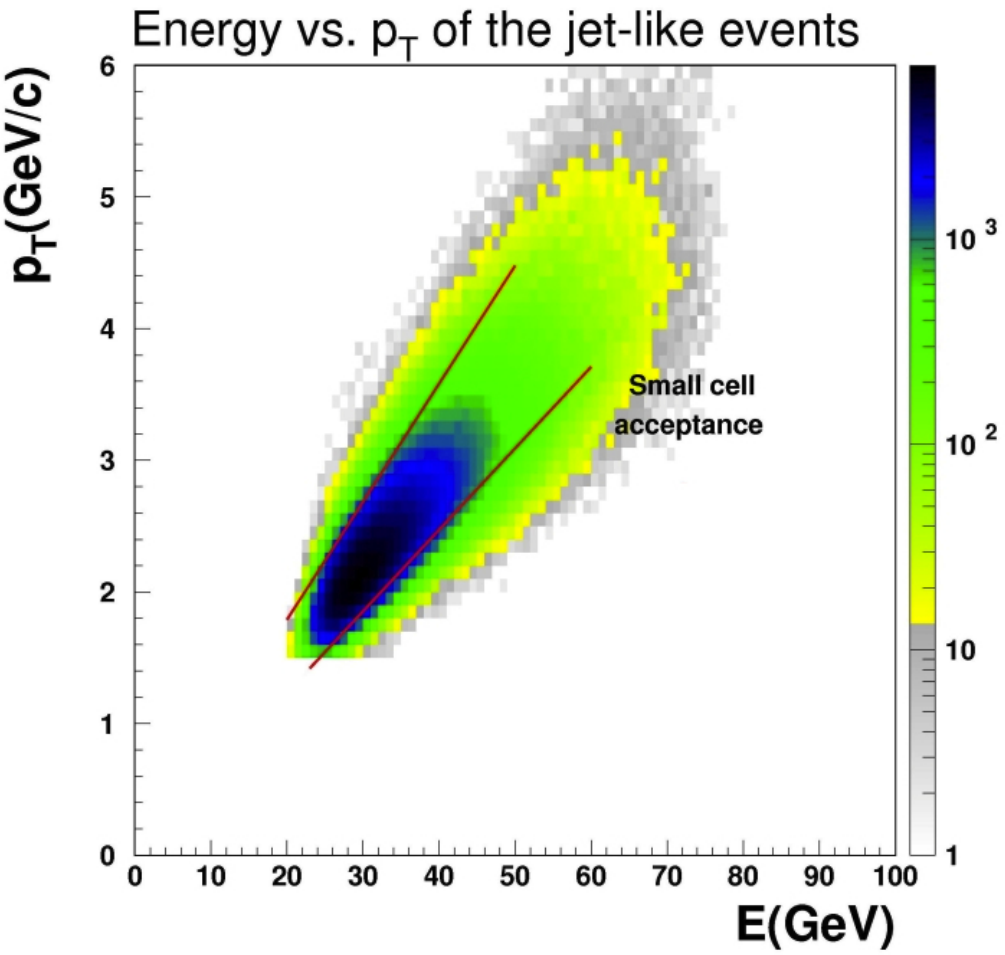

Figure 4.21: The locus of multiphoton events in the E-p_T plane. On the figure, the geometrical acceptance of the inner modules is given with red lines.

One can note from figure 4.21 that most of the events fall within the acceptance of the small cell modules, as expected, given the triggering scheme. The fraction of events in the outer cells is negligible, so one can expect that the average event will have its axis intercepting a small module and most of the energy will be contained there. The maximum radius of the event is set to 0.5 in the $\eta - \phi$ space, which corresponds to about 2 perimeters of large cells given that the jet intercepts the geometrical center of the small cell module. This is good from the viewpoint that the cells closest to the boundary of inner and outer cells have the

most accurate calibration factors.

Most of the energy deposited in the large cells is located near the inner-outer cells boundary. Additionally, in the cells further from the boundary, most energy comes from the side closest to the beam. In an average data event, 10.8 cells will be present, out of which 7.5 are small cells. It is likely that the small cells contain a neutral pion. This can be seen by calculating the invariant mass of the event, but including small cells only. Clearly visible is a peak slightly above the mass of the neutral pion, indicating that there is likely a leading pion in the small cells. The shift and the width of the peak suggest there are additional photons in the small cells aside from the two constituting the pion. The invariant mass calculated for events in the WS is given on figure 4.22. The data are compared with simulations with no simulated noise.

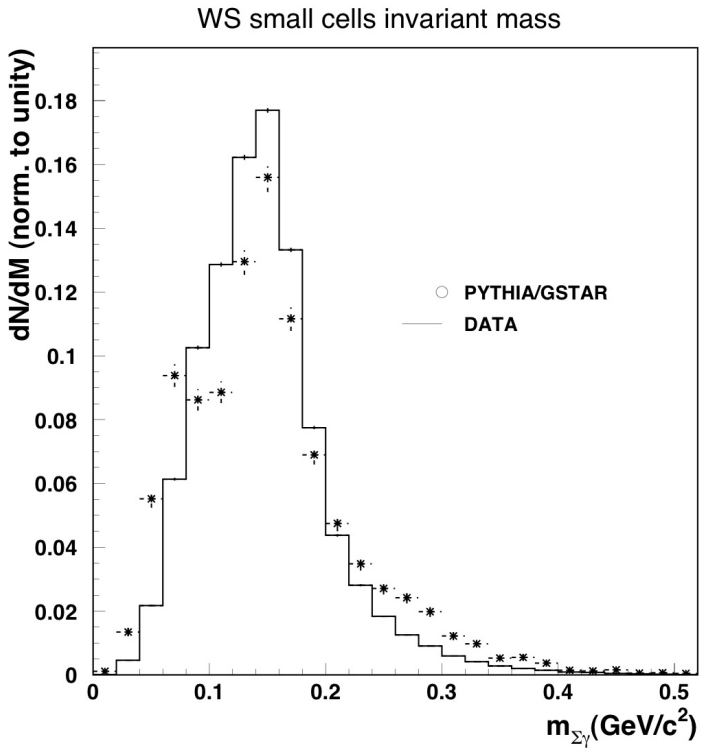

Figure 4.22: Calculated invariant mass of the multiphoton events calculated for small cells only. One can note the "widened, shifted" neutral pion peak. The data are compared to simulations with no simulated noise.

It is instructive to contrast this distribution to the mass distribution given in figures 4.4 and 4.5. It looks to be that the widened pion peak sits atop a background mass distribution that peaks near 0.08 GeV/c^2, and then falls to larger mass values. The multi-photon condition decreases the dominance of single neutral pions, in addition to shifting the peak to larger mass values, likely from additional energy in the inner calorimeter.

After the assessment of the multiphoton event characteristics, the unpolarized physics results were extracted and compared to the simulation results. These are listed in the Results chapter.

4.6. Association analysis

As described earlier, PYTHIA simulates particle production by either modeling soft processes or by computing via perturbative QCD hard scattering processes. For our set of simulations, the inner-calorimeter summed energy trigger primarily selects the former processes. The pQCD calculations in PYTHIA are done only at leading order in the perturbation theory, but the initial state and final state PYTHIA showering models allow for some aspects of processes beyond the leading order. Basically, showering done by PYTHIA uses splitting kernels to produce partons, and can effectively produce inelastic partonic scattering ($2 \rightarrow 3$) events. Strings are formed from the produced partons, and particles are produced via string fragmentation.

For each simulated event, one can get the PYTHIA listing. This list will include the history of the event, with mother hadrons, initial state partons, before and after radiation, final state partons, spectators partons etc. For each of these, the energy and momentum components can be read out. A part of a typical $2 \rightarrow 2$ scattering process listing is given in table 4.2.

Line	ID	M	D1	D2	p_x(GeV)	p_y(GeV)	p_z(GeV)	E(GeV)
1	2212	0	0	0	0	0	99.996	100
2	2212	0	0	0	0	0	-99.996	100
3	2	1	0	0	0.021	-0.516	35.838	35.842
4	21	2	0	0	-0.938	-0.006	-14.35	14.381
5	2	3	0	0	0.02	-0.508	35.309	35.312
6	21	4	0	0	0.793	0.246	-1.946	2.116
7	2	0	0	0	2.846	0.152	34.791	34.909
8	21	0	0	0	-2.033	-0.414	-1.429	2.519
9	2	7	21	21	2.812	0.15	34.384	34.501
10	21	8	21	21	-1.981	-0.853	-0.445	2.202
11	21	8	21	21	-0.018	0.44	-0.576	0.725
12	21	4	21	21	-0.759	0.109	-0.472	0.901
13	21	4	21	21	0.358	-0.78	-1.244	1.512
14	2101	2	21	21	-0.087	0.331	-76.893	76.896
15	2	0	34	34	-1.58	-0.622	-0.138	1.704
16	-2	0	34	34	1.58	0.622	23.12	23.182
17	2101	1	39	39	-0.021	0.516	40.165	40.172
18	21	4	39	39	-0.663	0.646	-2.13	2.323
19	21	4	39	39	-0.665	-0.235	-8.028	8.059
20	2	2	39	39	1.025	-0.325	-7.742	7.823

Table 4.2: A part of a PYTHIA listing for a typical event, showing first 20 lines and selected columns. Column 1 is a line counter. Column 2 gives the PYTHIA particle code. Column 3 is the line number for the mother of the particle and columns 4 and 5 are line numbers for daughters of the particle. Finally, the last 4 columns are the components of the four momentum.

This is just a part of the listing, showing first 20 lines and selected columns. Column 1 is a line counter. Column 2 gives the PYTHIA particle code. Quarks have positive IDs < 7, antiquarks negative IDs $>$ -7 and gluons have ID $= 21$. The IDs > 1000 belong to diquarks or hadrons. Column 3 is the line number for the mother of the particle and columns 4 and 5 are line numbers for daughters of the particle. Finally, the last 4 columns are the components of the four momentum.

The structure of the table is such that the first two lines represent the colliding particles, lines 3-4 are initial state partons prior to radiation, lines 5-6 are initial state partons after radiation, lines 7-8 are final state partons after the scattering process and lines 9-20 are partons produced by initial-state radiation, final-state radiation and spectators to the partonic scattering. An analysis of this specific table would give the following:

- The colliding particles are protons, each of energy 100 GeV, moving head-to-head on the z axis.
- Lines 3-4 and 7-8 are a quark and a gluon, so this is a qg $\rightarrow$ qg process.
- Lines 5-6 are the initial state quark and gluon after initial state radiation. Note that the sum of four momentum components in lines 5-6 and 7-8 are unchanged, indicating that this is an elastic scattering event.
- Lines 15 and 18 correspond to spectators from the proton. The sum of the four momentum of all spectators and participants in the hard scattering (prior to initial-state radiation) equals the initial-state proton four momentum.
- The other lines are partons produced in the initial-state radiation and the final-state radiation. Also in there (lines 10-11) are partons produced by final-state radiation, corresponding to a splitting of the scattered gluon into two gluons

The association analysis is used to establish whether the "jet-like" event reconstructed from the data is associated with either a hard-scattered parton or a parton from initial-state radiation. Given the rapidity difference from the beam, spectator partons are not relevant for the association. If the reconstructed "jet" is best associated with a hard-scattered parton, then the scattering is described as an elastic $2 \rightarrow 2$ partonic scattering. In the table, the final states 7 and 8 have large p_T and correspond to hard scattered particle to which the association analysis will be done. There are cases where multiple produced partons are found with large p_T in the final state, and the hard-scattered partons appear at mid-rapidity. In this case, the scattering is analogous to $2 \rightarrow 3$ inelastic parton scattering, which is a key addition beyond the leading order in NLO pQCD calculations.

The pseudorapidity and the angle were found for the associated parton and compared to the pseudorapidity and the angle of the reconstructed "jet-like" event. The association analysis was run through the entire simulation sample. The result is given in figure 4.23.

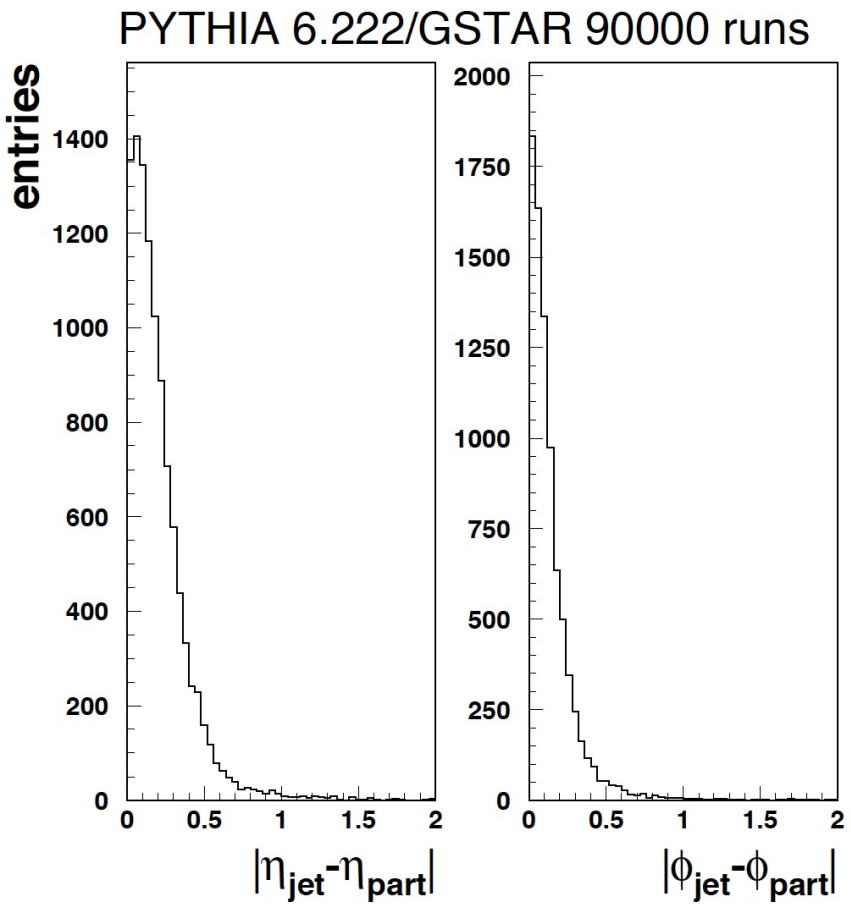

Figure 4.23: Results of the association analysis giving the difference of directions of the reconstructed "jet-like" event and the associated parton. The left panel shows the difference of the pseudorapidities, the right panel the difference of angles.

In principle, the association analysis serves to show that one can determine the multiphoton event jet axis and the direction of the scattered parton that produces the multiphoton event reasonably well, although one can not determine its energy well. This is due to the fact that the detector only emphasizes the electromagnetic part of the incoming jet. The result demonstrates that the "jet-like" events get associated with a parton and that the direction of the event is reconstructed well.

4.7. The Collins angle definition and analysis

The analysis strategy was at this point clearly identified and can be outlined. Looking at multiphoton events, coupled with neutral pion reconstruction, give means of partially measuring a second scale, as required to discriminate whether spin-correlated k_T is in the initial or final state. The dependence of the asymmetry on the Collins angle can be looked at. If there is no such dependence, and the asymmetry is larger than zero, one has isolated the Sivers effect, since the fragmentation is not involved, and one is left with just the initial state k_T. If there is such a dependence, one would be seeing asymmetry sensitive to the Collins effect.

So, after obtaining the unpolarized multiphoton event results, π^0 results and the association analysis results, the following step can be made. From the π^0 events, two categories will be formed; one in which the readout of the large cells is "live" and one in which it is not. Spinsorting and the calculation of cross ratios for these events can be made in the same way as for the complete π^0 event sample. This will show if the large cell dead time has any effect on the polarized π^0 results.

Next, from the first category, two subcategories are made: one where there is a multiphoton event found in the module where the π^0 is reconstructed and the other where there isn't a multiphoton event reconstructed. Then, as one can determine the multiphoton event jet axis and the direction of the scattered parton that produces the multiphoton event, the Collins angle can be defined. Looking at figure 2.8, one can see that this is the azimuthal angle of the pion with respect to the outgoing parton. The operational definition of the Collins angle in the detectors can be made as follows:

1. Find the coordinates of the multiphoton intercept point and the pion intercept point in the STAR coordinates. Figure 4.24 shows the STAR coordinate system along with the STAR angle ϕ definition. To the left is the south (S), to the right is the north (N).

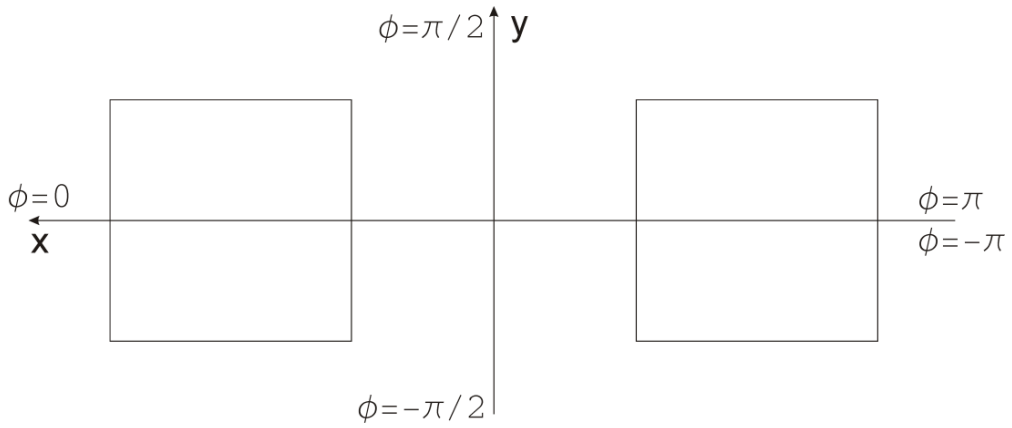

Figure 4.24: Schematic view of the detectors in the STAR coordinate system. The z axis points into the page and positive z corresponds to the z component of the momentum of the blue beam.

2. From the found coordinates, form vectors from the beamline to the multiphoton intercept point (p), and from the intercept point to the pion point (d). The vectors connecting the beam line and the pion (or the multiphoton) are the STAR angles ϕ_π and ϕ_{MP}.

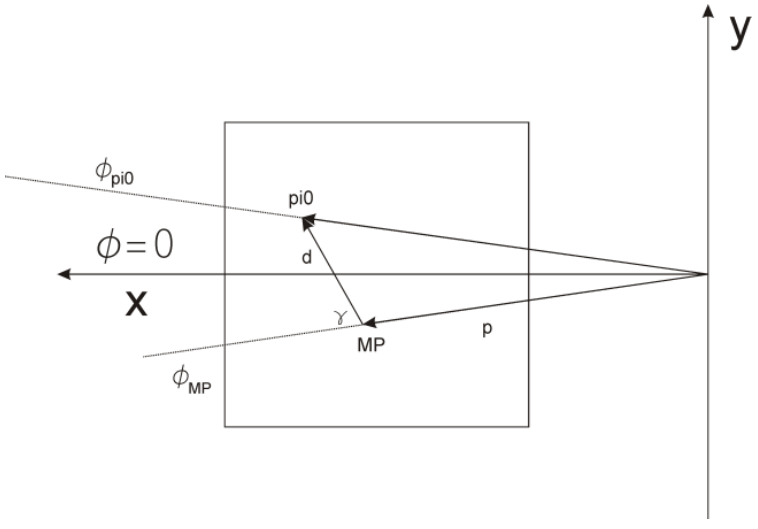

Figure 4.25: The definition of vectors used in the Collins angle calculation.

The angle between p and d is the Collins angle, designated here by γ. From calculation, the angle takes on values from 0 to π. We are currently dealing with the magnitude of γ, with the sign of γ determined as specified in item 3.

3. A further set of conditions is placed on the Collins angle, to define which are negative and which are not. The bins in the Collins angle are defined in such a way that they are mirror symmetrical, with $\gamma = 0$ being further from the beam and $\gamma < 0$ being the angles below the "beam pipe - multiphoton intercept" line. Figure 4.26 shows the calculated Collins angle if the multiphoton intercept point is in the center of a detector.

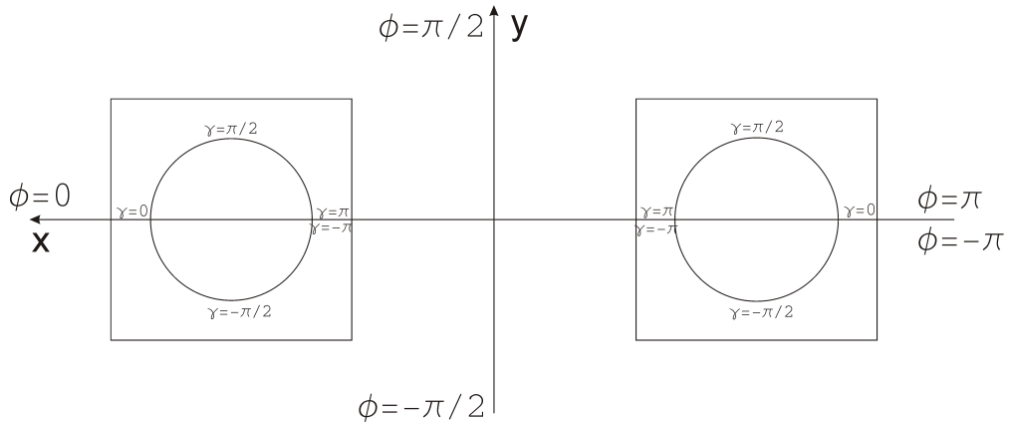

Figure 4.26: The calculated Collins angle in the case the multiphoton intercept points are in the center of the detectors.

A full operational definition of the Collins angle is given in the Appendix.

The resolution with which the Collins angle can get reconstructed was explored with the help of the association analysis. As both the reconstructed multiphoton event and the reconstructed π^0 have an associated parton and pion with them, one can define the "reconstructed" Collins angle and the "simulated" Collins angle. In the ideal case, the difference between these two quantities would be zero. The distribution of these differences was found for the same set of cuts as applied to the data. The result is given in figure 4.27. This result has shown that the Collins angle reconstruction works well.

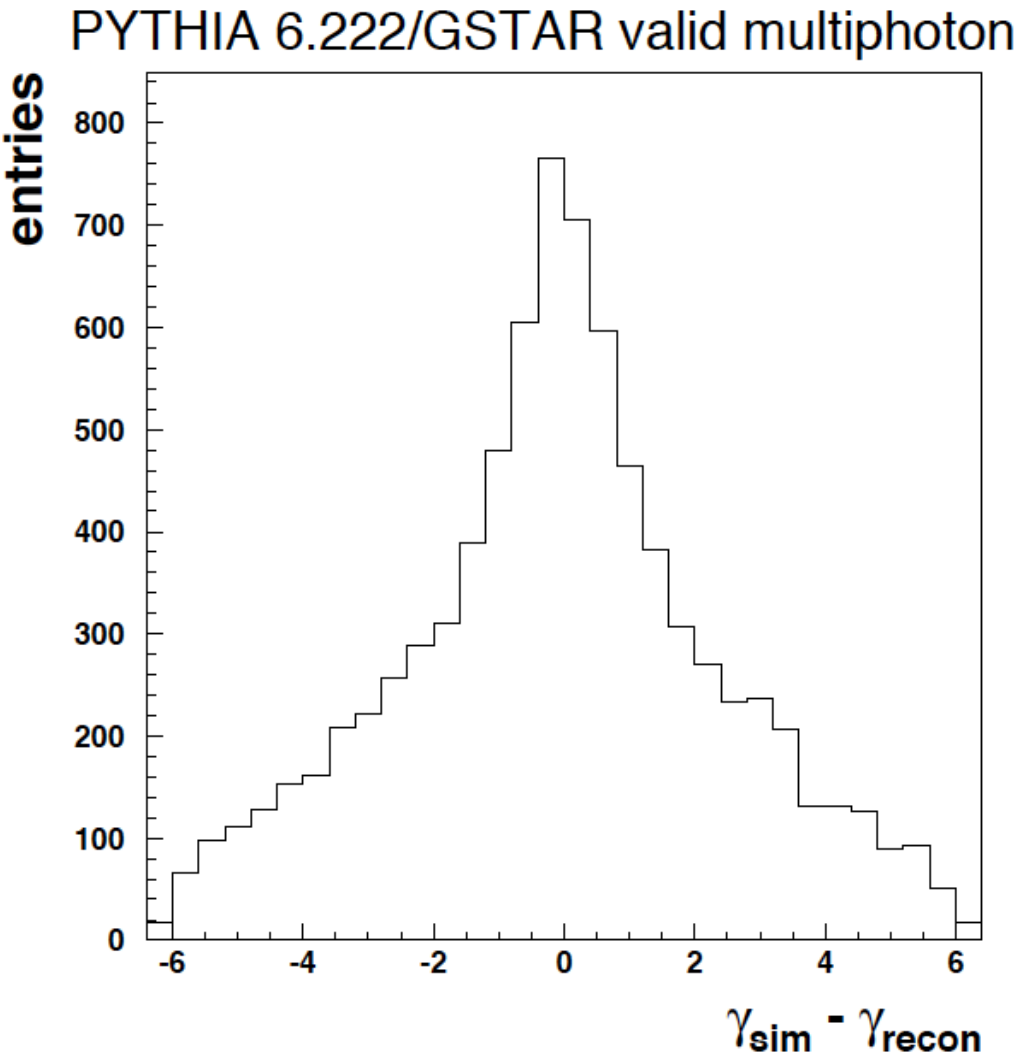

Figure 4.27: The difference of the "simulated" and the "reconstructed" Collins angle. The reconstructed angle is calculated with the help of the reconstructed π^0 and the multiphoton event, while the simulated angle is reconstructed from the associated simulated π^0 and the associated parton.

4.8. Analysis of polarized data and asymmetries

After defining the Collins angle, the events that contained both a pion and a multiphoton event in the same module were split into four bins in the cosine of the Collins angle. The bins are made to be flexible. A set of cuts on the differences of physical observables of the π^0 and the multiphoton was imposed. These were imposed to insure the "jettiness" of the multiphoton event. Typical cuts would include the difference in energies and/or the invariant mass.

After this binning, the spinsorting had to be done. To spinsort the results and calculate the asymmetries, one has to know the average run polarizations. The CNI Polarimeter Group develops, maintains and operates polarimeters in the Relativistic Heavy Ion Collider (RHIC) complex [51]. As stated in the Experiment chapter, the polarimeters include the AGS polarimeter, the pC polarimeter in RHIC and the polarized H-jet target, also in RHIC. In addition to providing polarization measurements that are essential to the RHIC Spin Program, the polarimeters also make it possible to measure single and double spin asymmetries in the $\sqrt{s}$ regimes accessible at RHIC. The measured polarizations for Run 6, as reported by the pcCNI group, are given on in [51].

Out of all of the Run 6 runs, only a fraction is important for this work. These are the runs that were included in the fills 7785 through 7833, given on figures 4.28 and 4.29. For the runs important to the analysis, the polarizations were equal to $P_{\text{blue}} = (0.55 \pm 0.04 \pm 0.03)$ and $P_{\text{yellow}} = (0.56 \pm 0.03 \pm 0.02)$. The first quoted error is statistical, the second is systematical. The polarization measurements, together with errors, are given on figures 4.28 and 4.29. For ease of viewing, the yellow polarization points are marked as red. In the figures, the statistical error is represented with the vertical error bar and the systematical with the horizontal error bar.

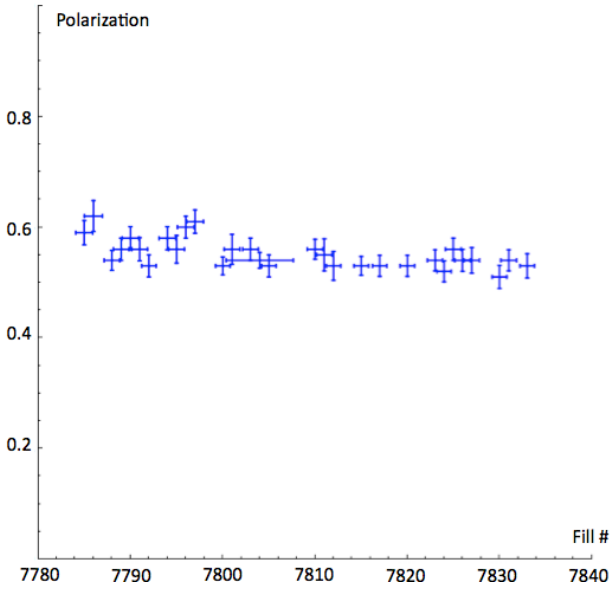

Figure 4.28: The measured polarizations of the blue beam for the fills important to this work. The vertical error bars represent statistical errors, the horizontal the systematical errors.

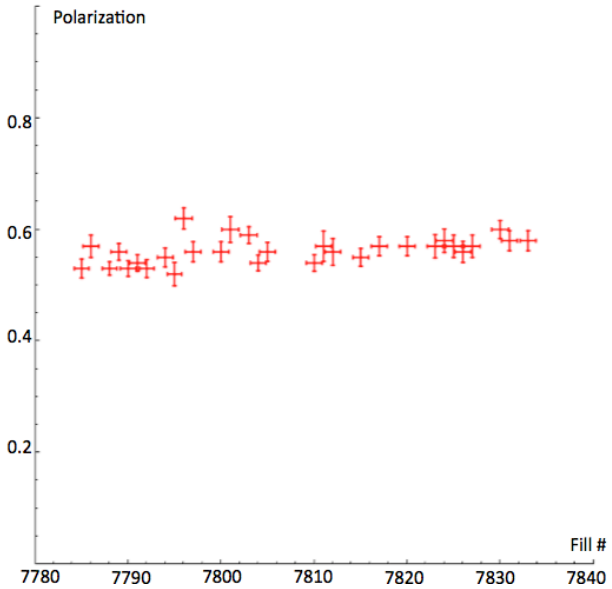

Figure 4.29: The measured polarizations of the yellow beam for the fills important to this work. The vertical error bars represent statistical errors, the horizontal the systematical errors.

After the average polarizations are determined, one can start asymmetry calculations. The asymmetries are calculated using the spin bits describing the polarization states of the blue beam and the yellow beam. The spin bits are checked, in the sense that the spin bits from CNI results are compared to spin bits from the DSM. If these patterns don't match, the data is excluded from the analysis. Specifically, because of this disagreement, all data from days 114-115, part of day 116 data and 12 runs from days 118-129 were excluded from the analysis.

The calculation then proceeds by binning the events in energy bins, as well as spin bins. The "energy" was chosen to be the reconstructed neutral pion energy, with the energy bins given earlier. The spin bins are simply "blue up", "blue down", "blue other", "yellow up", "yellow down" and "yellow other". Finally, the asymmetry is calculated using the "cross-ratio" method, as given by equation (2.5). There are, of course, various choices of what the quantity entering (2.5) can be. A choice used earlier, for the published Run 6 neutral pion analysis [8] is the number of reconstructed neutral pions. A choice for the current analysis will be the number of events that contain both a reconstructed neutral pion and a multiphoton event, satisfying all cuts.

The asymmetry is now calculated in the following way. The calculated cross ratio for a given $\cos(\gamma)$ bin is equal to:

$$\epsilon = \frac{\sqrt{N_{+}^{L} \cdot N_{-}^{R}} - \sqrt{N_{-}^{L} \cdot N_{+}^{R}}}{\sqrt{N_{+}^{L} \cdot N_{-}^{R}} + \sqrt{N_{-}^{L} \cdot N_{+}^{R}}}, \tag{4.9}$$

where $N_{+,-}^{L,R}$ are given by the following definitions:

For the γ bin near zero,

- N_{+}^{L} stands for the number of events that had a spin-up left-scattered jet and a right-fragmented pion.
- N_{-}^{R} stands for the number of events that had a spin-down right-scattered jet and a left-fragmented pion.

These two quantities are related by a rotation about the z axis by 180^0. Consequently,

they both measure the fragmentation to the right of a spin-up scattered jet (the same as the fragmentation to the left of a spin-down scattered jet). By forming the geometric mean of these terms, detector induced effects should be minimized.

Further, for the γ bin near zero,

- N_{-}^{L} stands for the number of events that had a spin-down left-scattered jet and a right-fragmented pion.

- N_{+}^{R} stands for the number of events that had a spin-up right-scattered jet and a left-fragmented pion.

  Again, these two quantities are related by a rotation about the z axis by 180^0. They measure the fragmentation to the left of a spin-up scattered jet (the same as the fragmentation to the right of a spin-down scattered jet).

Furthermore, N_{+}^{L} and N_{-}^{L} in the bin near $\gamma = 0$ fix the fragmentation to be to the right of the jet and reverse the polarization. Also, N_{+}^{R} and N_{-}^{R} in the bin near $\gamma = 0$ fix the fragmentation to be to the left of the jet and reverse the polarization. So, the desired asymmetry will be obtained by forming the difference between N_{+}^{L} and N_{-}^{L} or N_{+}^{R} and N_{-}^{R}.

For inclusive production, it would be analogous to doing a single-arm experiment, reversing the polarization. In such a measurement, the spin-dependent relative luminosity would need to be used. The geometric mean in this cross ratio definition should cancel detector effects. The same consideration can be made for the other bins.

If one now considers how things behave at different $\cos(\gamma)$, the conclusion is the following. For the Sivers effect, the spin asymmetry does not depend at all on the $\cos(\gamma)$ bin. So, a spin asymmetry independent of $\cos(\gamma)$ is expected. For a positive Collins effect, the spin asymmetry for the $\cos(\gamma)$ bin for γ near π will be larger than the spin asymmetry for the $\cos(\gamma)$ bin for γ near zero. Consequently, the slope of the spin asymmetry as a function of $\cos(\gamma)$ is a signal of the Collins effect. The "offset" of the spin asymmetry as a function of $\cos(\gamma)$ is a signal of the Sivers effect.

Other spin asymmetries could be formed, but would not account for detector effects in the same manner as the cross ratio formed like this.

4.8.1. Systematic error calculation

The systematic error of the result can have many sources, which should all be taken into account. Two of the largest sources are the model of the multiphoton event, which can be explored via the cuts imposed on the multiphoton sample, and the uncertainty of the calibration of the large cells. Other systematic effects, like the polarization uncertainty of luminosity fluctuations are far smaller than these two. Since one should be interested only in the size of the maximal systematic errors, these effects were not explored in depth. The two effects mentioned were analyzed in such a way that we either purposely introduced a different model of a multiphoton event by varying the weighted multiplicity cut by 10% in both directions and observed the influence on the final result or purposely introduced the correction factors that are 10% larger (smaller) than the ones obtained and used for analysis, and again, observed the influence on the final result. For each bin, the maximal systematical error was calculated and plotted as a gray-shaded area in the result. Detailed information on the systematical error is given in the "Results" chapter.

4.9. Potential impact of imperfections

In an experiment there are always imperfections, and one needs to conduct a research of how these imperfections could impact the results. A primary imperfections concerns the uniformity of the calibration and the calibration of the cells far from the beam. An investigation can still be done on improvement of these factors. One could repeat the previous di-photon calibration procedure but allow for more than two photons in the outer cells. This would improve statistics at the cost of the resolution of the mass peak. A possibility exists that the uniformity of the correction factors could be improved by running more di-photon calibration iterations. This procedure is very time costly, so, given that the improvement would be very small, it was never conducted. Further, given the fact that the results are mostly sensitive to the small cells, the impact of this imperfection is negligible.

Chapter 5.

Results and discussion

5.1. Inner cells π^0 results

The analysis of the π^0 events is done immediately after the calibration of the detector, as described in the Data analysis chapter. The asymmetry was calculated and binned in x_F, as well as in p_T. Given on figure 5.1 is the transverse single spin asymmetry in x_F bins at two different pseudorapidities. The right side of the figure represents the FPD++ small cells ($< \eta >= 3.3$) and the left side the FPD ($< \eta >= 3.7$). Statistical errors are indicated for each point and systematic errors are given by the shaded band, excluding normalization uncertainty. The Sivers and twist-3 calculations, also given on the figure, are described in the text. The inset in the figure shows examples of the spin-sorted di-photon invariant mass distributions. The vertical lines in the insets mark the position of the π^0 mass. The p_T dependence for events with $|x_F| > 0.4$ is given on figure 5.2. Errors are the same as described for figure 5.1. Finally, transverse single spin asymmetries versus π^0 transverse momentum in fixed x_F bins are given on figure 5.3.

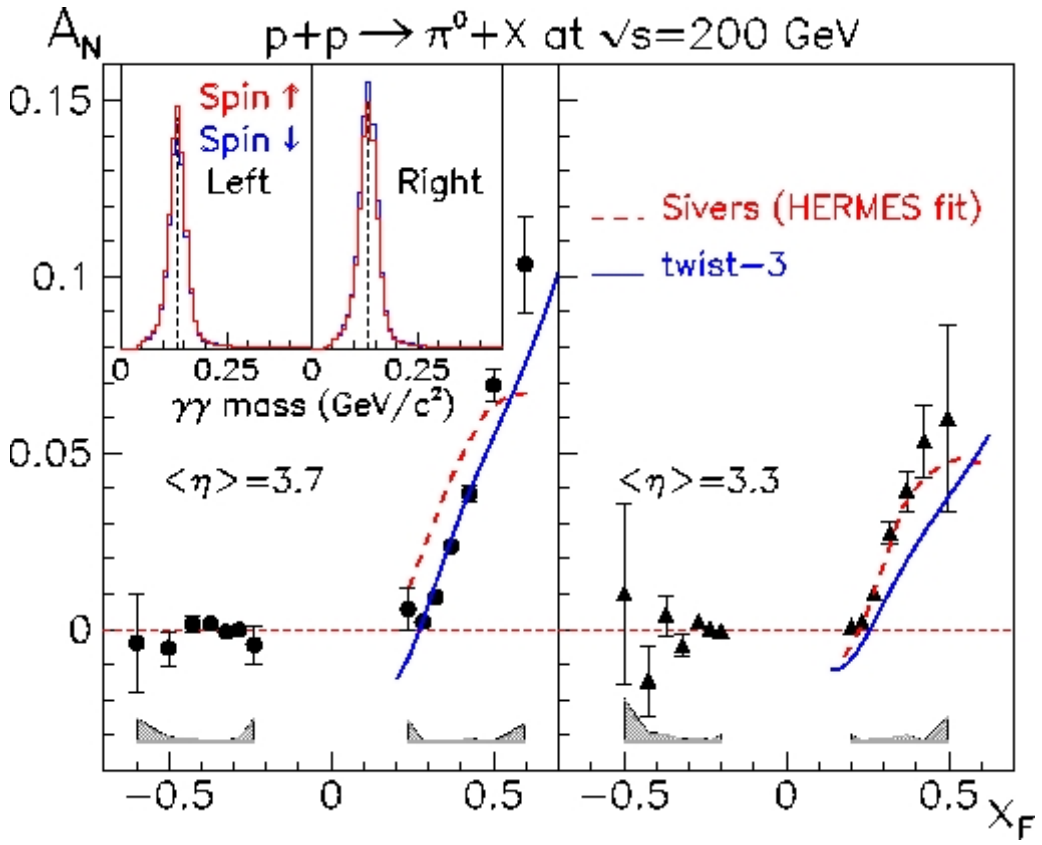

Figure 5.1: Calculated asymmetry for π^0 events in x_F bins. The right side of the figure represents the FPD++ small cells ($< \eta >= 3.3$) and the left side the FPD ($< \eta >= 3.7$). Statistical errors are indicated at each point and systematical errors are given by the shaded band, excluding normalization uncertainty [8].

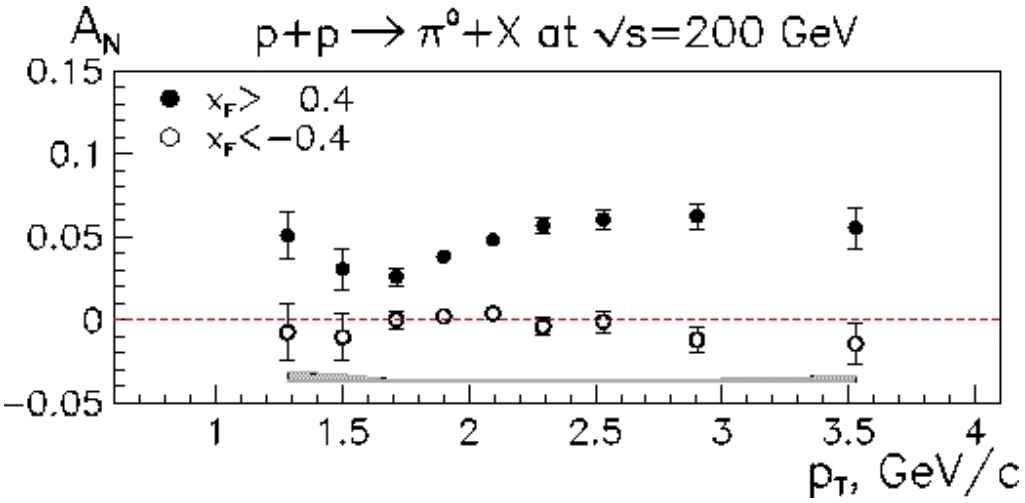

Figure 5.2: Calculated asymmetry for π^0 events in p_T bins for events with $|x_F| > 0.4$ [8].

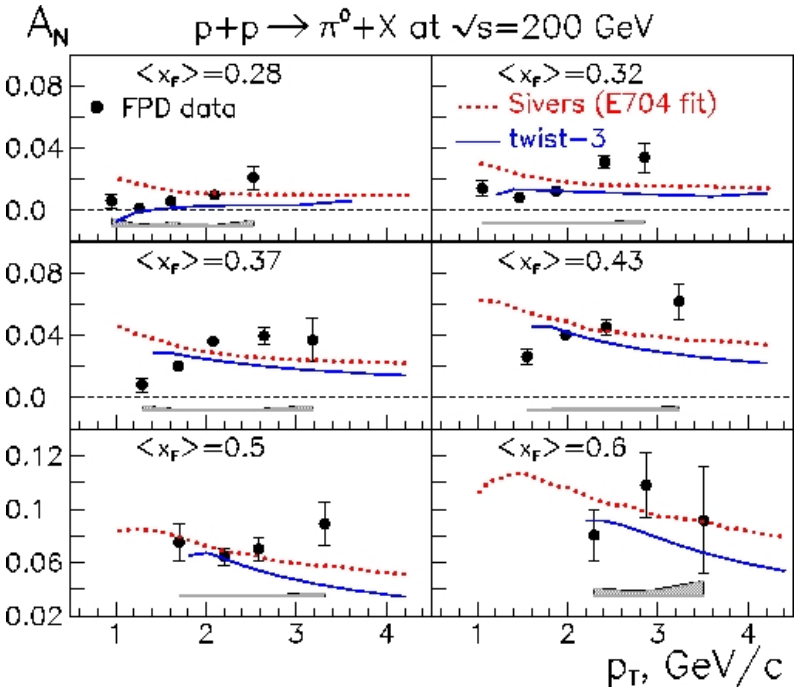

Figure 5.3: Calculated asymmetry for π^0 events in p_T bins at fixed x_F. One can see that the data and the theory don't agree well [8].

Several things should be noted from these results. First, figure 5.1 shows precision measurements of the asymmetry in x_F bins and they show agreement with theory. They agree in the fact that the asymmetry rises with x_F, although it is not conclusive which model the data follow. Specific values of the calculated asymmetries are given in the Appendix. The p_T dependence, given on figure 5.2, on the other hand, disagrees with theoretical predictions. In fact, the data show tendency to behave oppositely to the predictions. This holds true for all x_F bins, except maybe for the last two bins, where the results are inconclusive.

Another very important feature of these results lies in our understanding of the underlying theory. One can make that claim by looking at the measured cross section vs. the theoretical prediction for the cross section. Still, the transverse momentum distribution (TMD) calculations [20], are not based on a proven factorization theorem. To the contrary, it is fully expected that hadroproduction of hadrons will break factorization, due to all the initial and final state color-charge interactions. Consequently, the calculations are strictly a model. At least this model gets ingredients from other probes (e.g., Sivers functions from fits to SIDIS). Further, the twist-3 calculation makes no contact with data, other than pp scattering. It does include the E704 results and there is a proven factorization theorem [21, 22]. The twist-3 calculations are not independent of TMD model calculations, in that the "Wilson gauge link" required by gauge invariance for the TMD approach is accounted for to twist-3 in the Qiu-Sterman approach. The downside is that there is no "universal" fit to pp and SIDIS data.

5.2. Unpolarized multiphoton results

The multiphoton event unpolarized results are given in this section. "Unpolarized" means that the spin information for all events is disregarded. These results can be compared to the simulation results since there is no polarization there as well. After verifying that the data and simulations show reasonable agreement, one can proceed to look at polarized results. The results in the simulations depend, naturally, on the amount of noise that is simulated, which will be discussed in more detail later.

The set of cuts used to obtain the multiphoton results was the following:

- At least 23 GeV of energy deposited in a small cell calorimeter. As opposed to the π^0 analysis, where this cut was set to 15 GeV, it was increased here to avoid threshold effects.
- A requirement that the large cell readout is live.
- At least 4 cells with energy of at least 400 MeV deposited in any combination of same side large and small cells.
- At least 10 cell in the "weighted sum of cells". The weight of the small cells was set to 1, the weight of large cells was set to 1.52, which is the ratio of sides of large and small cells.
- A maximum of 20 cells with energy of at least 400 MeV deposited in any combination of same side large and small cells. This cut was introduced to avoid large combinatorial factors in the multiphoton event search code.
- Maximum energy deposited in all calorimeters was set to 80 GeV. This was put in place to avoid any possibility of LED events in the considered sample.
- After reconstruction of the multiphoton event, its jet axis was required to be within a two cell fiducial volume of a calorimeter. This cut was introduced to avoid looking at multiphoton events whose significant fraction of energy was not recorded in the calorimeter and was, hence, not well reconstructed.

- The minimal transverse momentum of the reconstructed multiphoton event was set to 1.5 GeV/c
- The cut on the size of the cone of the multiphoton event in the η–ϕ space was set to a maximum of 0.5.

It is important to mention that the same set of cuts was used in an earlier analysis of multiphoton events that was done with the Forward Meson Spectrometer (FMS) [52]. This is good from the viewpoint that one can try to compare the results obtained at that point with the result obtained with the FPD++. However, a number of difficulties arises in trying to make the comparison, as described in the next subsection.

The characteristics of the multiphoton event sample are summed up in figures 5.4 through 5.12. The one dimensional histograms are overlays of data and simulations and the twodimensional histograms show only data. In the overlays, the distributions are normalized to 1, so that one can compare them in the data and simulations. The WN and WS modules show great similarity, so it is not necessary to show results for both of them. Only the results of the WN calorimeter are presented here.

An average WN multiphoton event will have 10.66 towers present in the jet, with an average energy of 34.23 GeV. Out of this, 7.3 towers are from the small cells and carry an average energy of 26.68 GeV. This is about 80% of the energy of the entire multiphoton event, so most of the energy of an event is deposited in the small cells, which serve as the trigger. The fact that the events are mostly contained within the small cells can be seen from two more results. One was given on figure 4.21, showing that most events fall within the small cell acceptance region. The other is the spatial distribution of the points where the calculated jet axis intercepts the detector face ("jet intercept" points), given on figure 5.7.

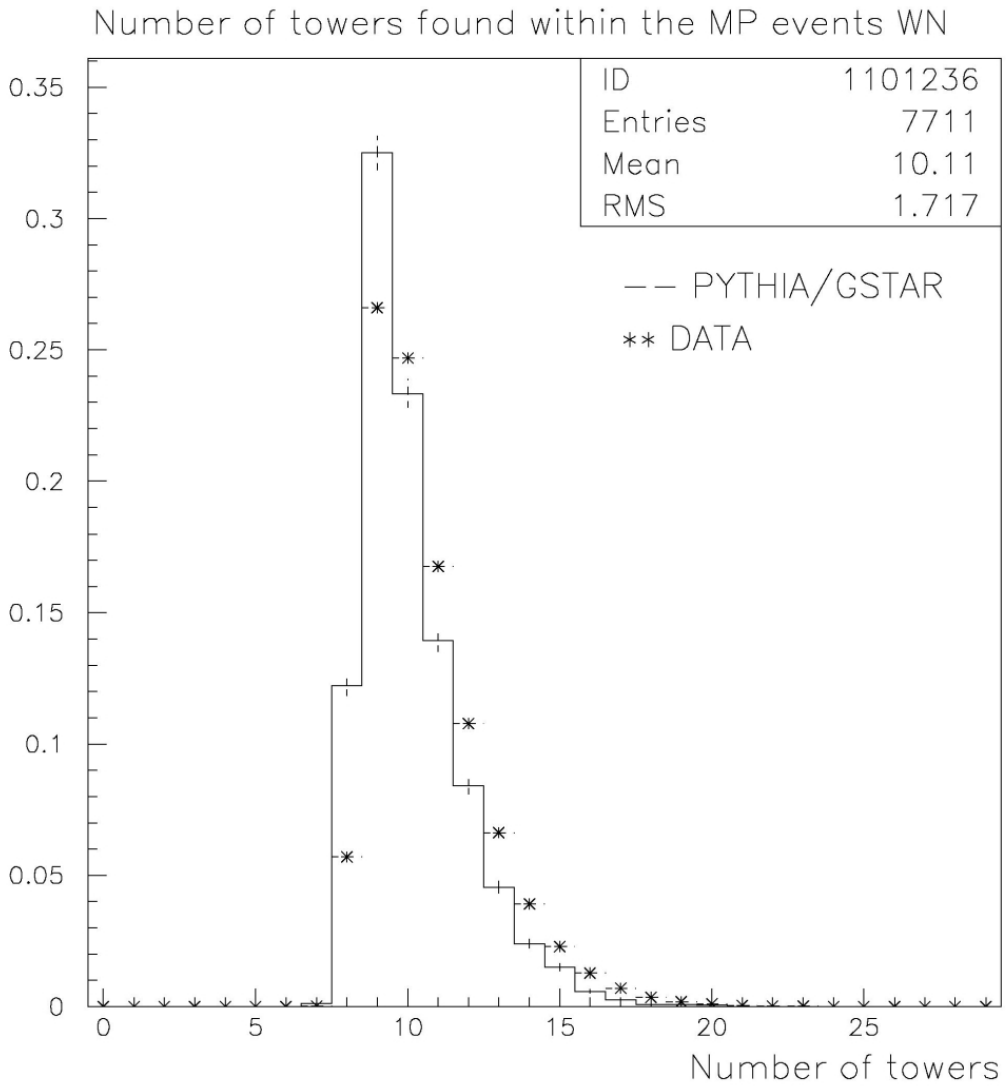

Figure 5.4: The number of towers in the multiphoton events in the WN calorimeter. The difference of the average value (shown on image for simulations) for data and simulations is about 5% and equals 10.66 for the data sample. The error bars are statistical.

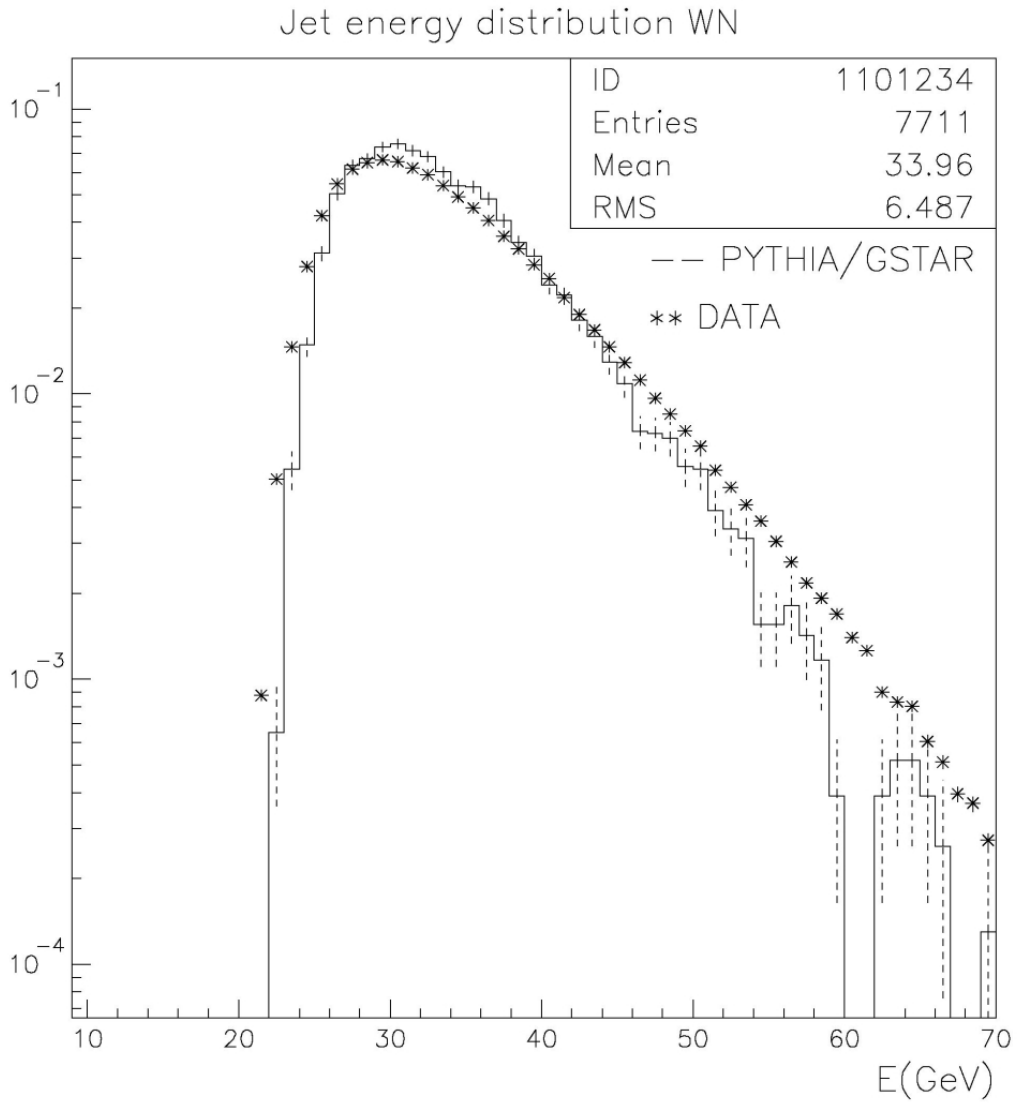

Figure 5.5: The energy distribution of the multiphoton events in the WN calorimeter. The difference of the average value (shown on image for simulations) for data and simulations is $< 1\%$ and equals 34.23 GeV for the data sample. The error bars are statistical.

The "jet intercept" distribution can be viewed in the detector coordinate system or the STAR coordinate system. In the STAR system, the distance from the beam in the detector plane is described by the x coordinate. So, the x distribution shouldn't be symmetric around the axis of symmetry of the detector, since the cells closer to the beam receive more energy than those further from the beam. This does not hold true for the y axis, though. The $y = 0$ in the STAR system is exactly the line that is also, in case of the ideal placement of the detector, an axis of symmetry of each module. So, the y distribution of the intercept points should be symmetric and maximal around $y = 0$ if the detector is placed ideally. If it is not, as in reality, than the maximum should still appear at $y = 0$, but the mean value of the distribution y_0 should be somewhere between that and the axis of the symmetry of the detector, $y = y_{\text{sym.}}$. This claim assumes that the detector response to the incoming energy is y independent. The distribution is illustrated in figure 5.6.

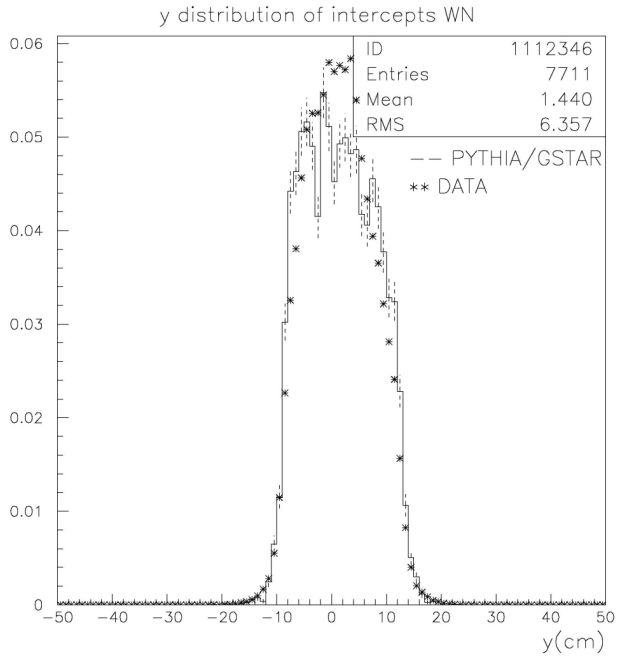

Figure 5.6: The y distribution of the points where the calculated jet axis intercepts the WN calorimeter face. The maximal value appears at $y = 0$, but the mean is shifted toward the the value at the axis of symmetry of the detector, $y = 1.9\,\text{cm}$. The error bars are statistical.

Two more important observables to look at are the ratio of events in the N/S calorimeters and the uniformity of events throughout them. To investigate this, it is best to separate the data sample into multiphoton energy bins. 9 bins were created: 20-23 GeV, 23-27 GeV, 27-30 GeV, 30-33 GeV, 33-37 GeV, 37-40 GeV, 40-45 GeV, 45-50 GeV and >50 GeV. The first bin will be almost unpopulated due to the cuts imposed on the event sample. The number of events in a bin will then have a sudden rise in second bin and still grow to the third bin, which is, energetically speaking, still near the WS trigger threshold. After that, the statistics fall suddenly, as does the energy deposition in the detectors. The spatial distribution of intercepts for 33-37 GeV bin for both calorimeters is given in figure 5.7.

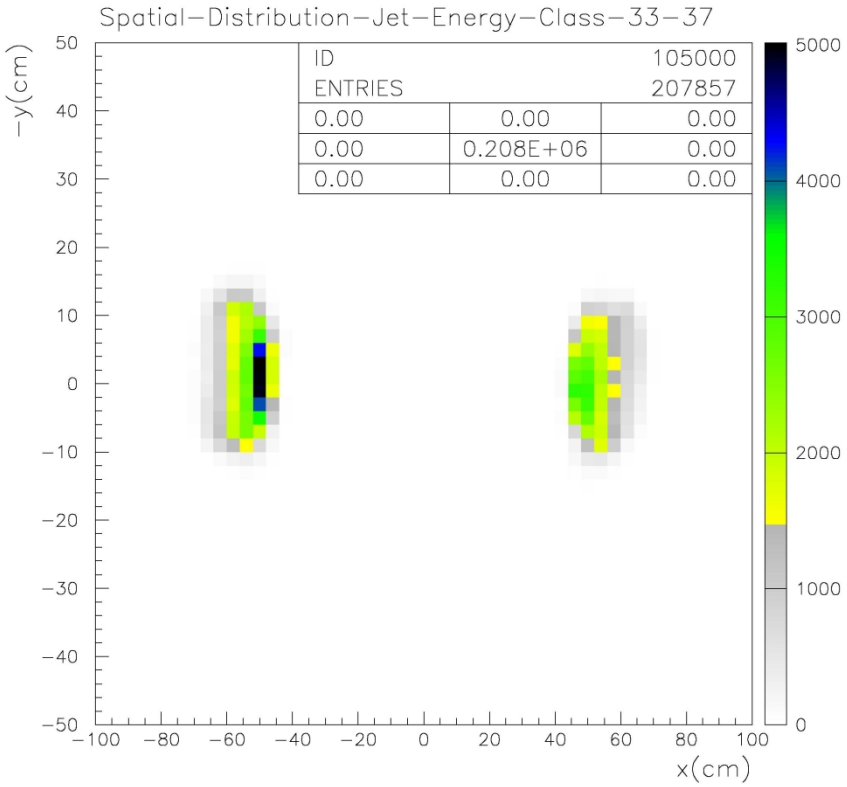

Figure 5.7: The spatial distribution of the points where the calculated jet axis intercepts the calorimeter faces in the 33-37 GeV multiphoton energy range. One can see that the distributions show the largest number of events in the areas closer to the beam. Also, it can be noted that there are more events in the WN (left side of the image) than in the WS.

In all the bins there are more events in the WN detector than in the WS detector. The difference in the number of events is about 10-15% and it is there due to hardware trigger conditions. Specifically, the WN will issue the hardware trigger about 3 times more than the WS will because the average gain of the cells in WN is about 5 MeV/count lower (summed over all cells) than the gain of the WS cells. This triggering asymmetry falls with the rise of energy, as expected, but is still present at higher energies.

The uniformity of events is best looked at from the perspective of the jet-like event, not from the STAR coordinate system. After finding the jet intercept point, one can make it the origin of a new, "jet" coordinate system. The distance from the origin of this coordinate system will be called R. The system is simply the translation of the STAR system to the point of intercept. The line of $\phi' = 0$ is defined as the line parallel to the STAR $y = 0$ line, looking away from the beam for WN and toward the beam for WS. To investigate the uniformity of events, for all the towers that are present in a single event, the angle with respect to $\phi' = 0$ is found. This angle is simply called ϕ'. For each tower, the distance from the jet axis (R) and the angle (ϕ') are found and plotted in a two dimensional histogram. This is given in figure 5.8. This representation will, on average, show the distribution of energy of multiphoton events in the detectors, given that an average multiphoton event intercepts the calorimeter in the geometrical center of its face.

From the ϕ' axis of figure 5.8 one can note that there are many events near $\phi' = \pm\pi$. This is because this is the "beam side" and most of the energy is deposited there. From the R axis one can note that there are many events near $R = 0$ and fewer events as R increases. This is because for a multiphoton event, most of the energy is concentrated close to the jet axis, i.e. near $R = 0$. The first bin in R has less events than the next because in the limit $R \to 0$ the number of towers also goes to zero. In the ideal case, to get rid of the ϕ' dependence, one can weight each tower with the energy deposited in it and then divide that histogram with this one. This is shown is figure 5.9. The results shows the effect of evening out the energy dependence, since the higher energy events will divide with higher count events and vice versa. This way one can again investigate the uniformity of the calorimeter.

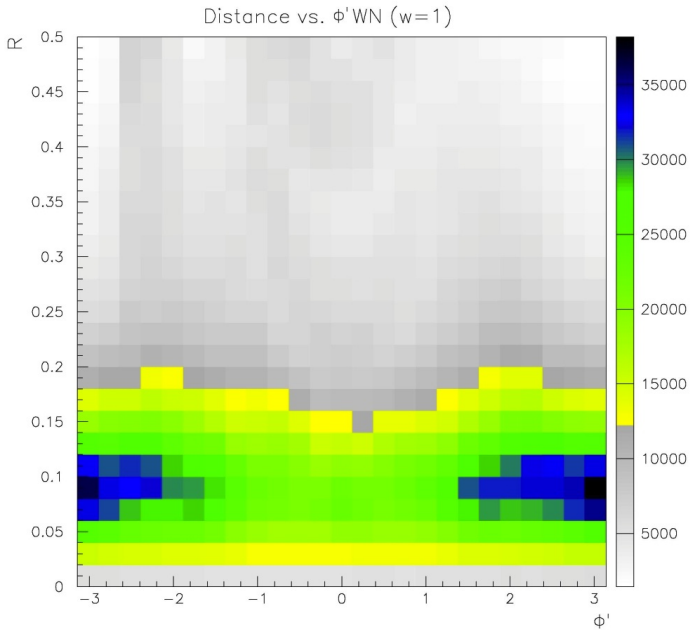

Figure 5.8: The distance of the towers vs. the angles with respect to the $\phi' = 0$ in the multiphoton events.

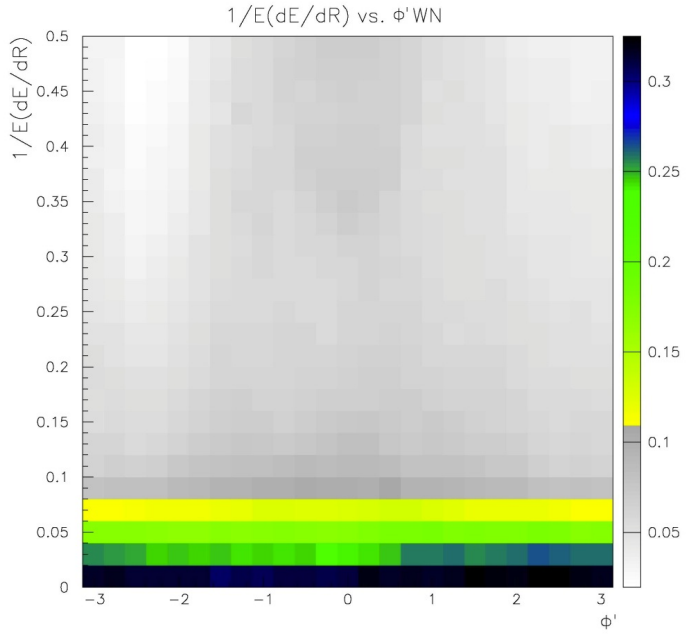

Figure 5.9: The $1/E_{\mathrm{mp.}}(\mathrm{d}E_{\mathrm{mp.}}/\mathrm{d}R)$ vs. ϕ' distribution.

In the ideal case, this distribution in figure 5.9 should be ϕ independent. This is an important quantity that gives the "Jet energy profile" - how much energy is deposited at a certain distance from the jet axis.

Figures 5.7 - 5.9 could also be given for the simulation sample, but they are so similar to the data results it is not instructive to show them here. It is visible from figure 5.9 that the distribution is uniform in the angle ϕ' up to a few percent. This is in accordance with the calibration, which is no more uniform than that. Figure 5.9 shows the distribution integrated over all the energy bins defined earlier; dividing it into energy bins and integrating it over all ϕ'-s will give the $1/E(\mathrm{d}E/\mathrm{d}R)$ distributions, where E is a shorthand for $E_{\mathrm{mp.}}$. This is one important observable of the multiphoton events. Other physical observables worth mentioning are the invariant mass of the multiphoton event and the ratio of energy in the small cells and the entire multiphoton event. The invariant mass of the multiphoton event is calculated as:

$$m_{\Sigma\gamma} = \sqrt{E^2_{\Sigma\mathrm{towers}} - \left(p^{\mathrm{reconstructed}}_{\mathrm{average}}\right)^2}\,. \tag{5.1}$$

Here, $E_{\Sigma\mathrm{towers}}$ is the summed energy of all the towers in an event and $p^{\mathrm{reconstructed}}_{\mathrm{average}}$ is the average of the reconstructed momenta from all the towers in the event. The magnitude of p for a tower is taken to be equal to energy for that tower, since it is assumed that the energy deposition is from a massless photon. The three mentioned physical observables were calculated, separated in energy bins and compared to simulations. In figures 5.10 - 5.12 the energy bin 30-33 GeV is shown for WN. For this bin, the average x_F equals 0.32, and the average p_T is 2.3 GeV/c.

Looking at figure 5.10, one can see the excellent agreement of data and simulations. This figure shows the jet energy profile, i.e. the amount of energy deposited at a certain distance from the jet axis in the $\eta - \phi$ space. It is expected that most of the energy is contained near the jet axis and the further one goes from the axis, the less energy one will find. After a starting steep decrease, a gentler decrease is expected. This can be seen from the result both in data and simulations. The results repeats itself in all the bins. The WS calorimeter shows very similar results, although with a feature that was dubbed the "jet-tail". This is

the effect that the distribution starts to slowly rise again near the boundary of the jet cone, i.e. close to R=0.5, and is discussed more later.

Figure 5.11 shows the invariant mass of the multiphoton events. In this case, the agreement between data and simulations is still good, although not as good as for the jet profile. A short investigation shows that the most likely cause for this is the lack of simulated noise in the simulation sample.

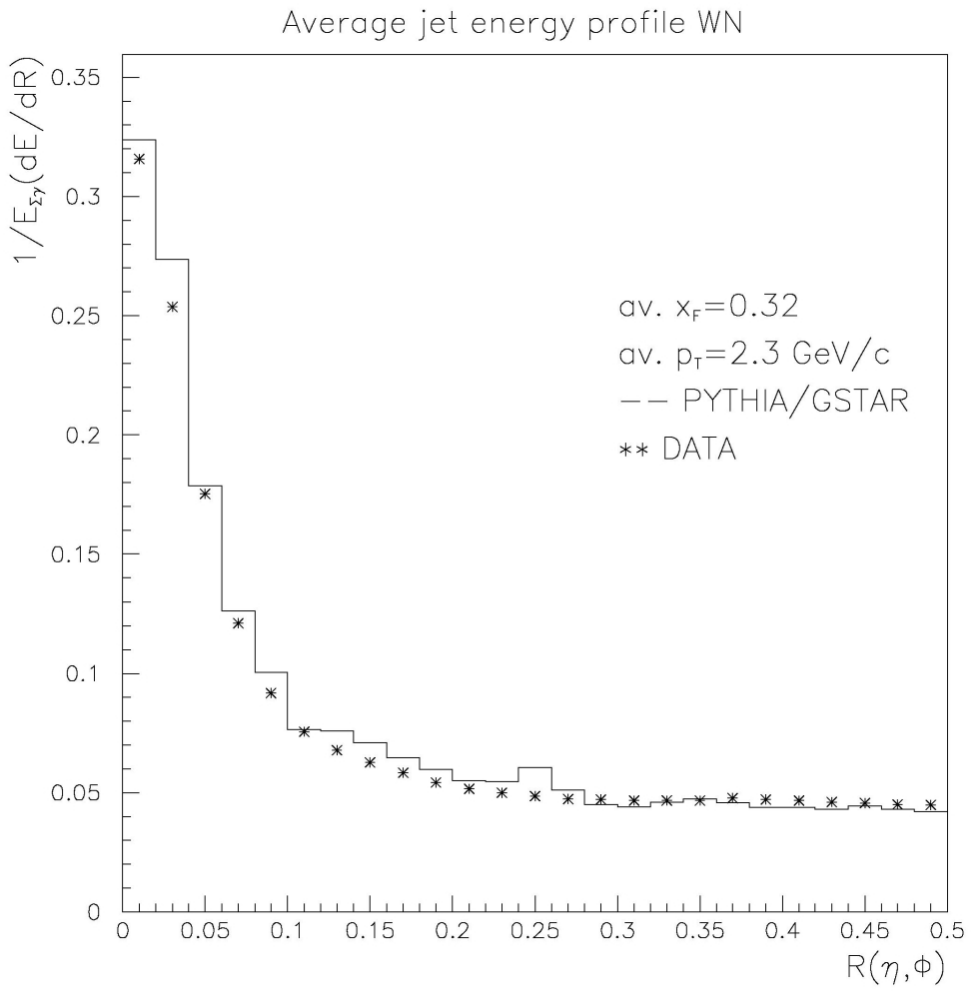

Figure 5.10: The $1/E_{\mathrm{mp.}}(\mathrm{d}E_{\mathrm{mp.}}/\mathrm{d}R)$ (jet profile) distribution for the energy bin corresponding to $< x_F >$=0.32 in the WN module. The data and the simulation sample show very good agreement.

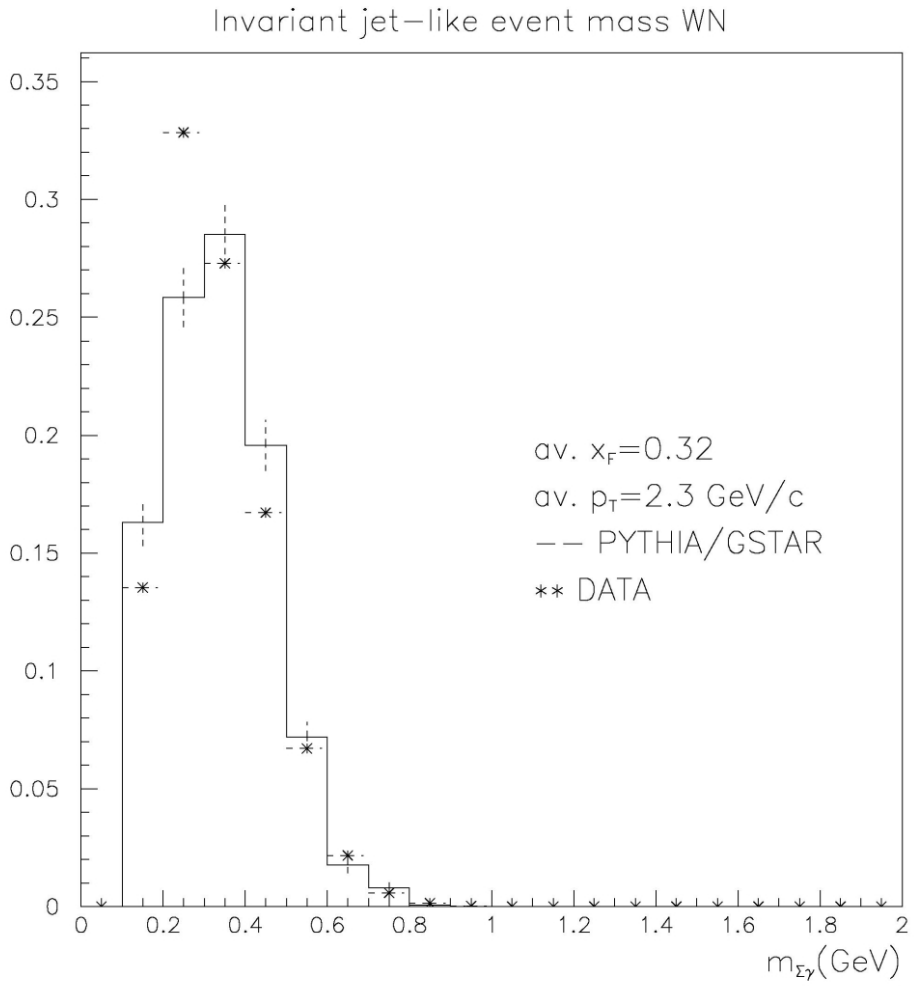

Figure 5.11: The invariant mass of the multiphoton events compared in the data and simulations for the energy bin corresponding to $< x_F >$=0.32 in the WN module. The data and simulations show fair agreement. The errors bars give statistical errors.

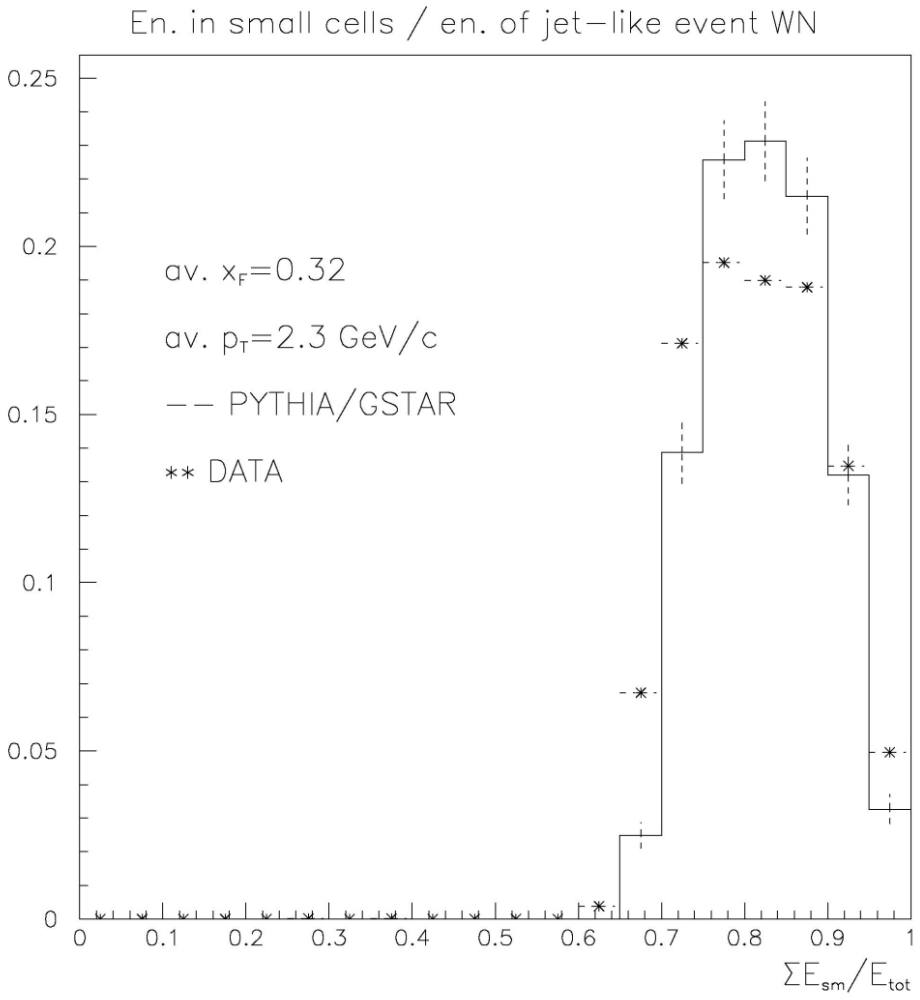

Figure 5.12: The ratio of energy in the small cells and the multiphoton energy compared in the data and simulations for the energy bin corresponding to $< x_F >$=0.32 in the WN module. The data and simulations show fair agreement. The errors bars give statistical errors.

Figure 5.12 gives the ratio in the small cells and the multiphoton event energy. This ratio is always in favor of the small cells, since most of the energy comes from there. This is natural, since they served as the trigger. Here, again, the data and simulations show fair agreement.

5.2.1. Comparison with the FMS results

One could try to compare the result for the jet energy profile and the invariant mass of the jet-like event with previously published results from STARs Forward Meson Spectrometer (FMS) [52]. The schematic view of the FMS is given on figure 5.13. The FMS was placed on the STAR west platform after dismantling the FPD++.

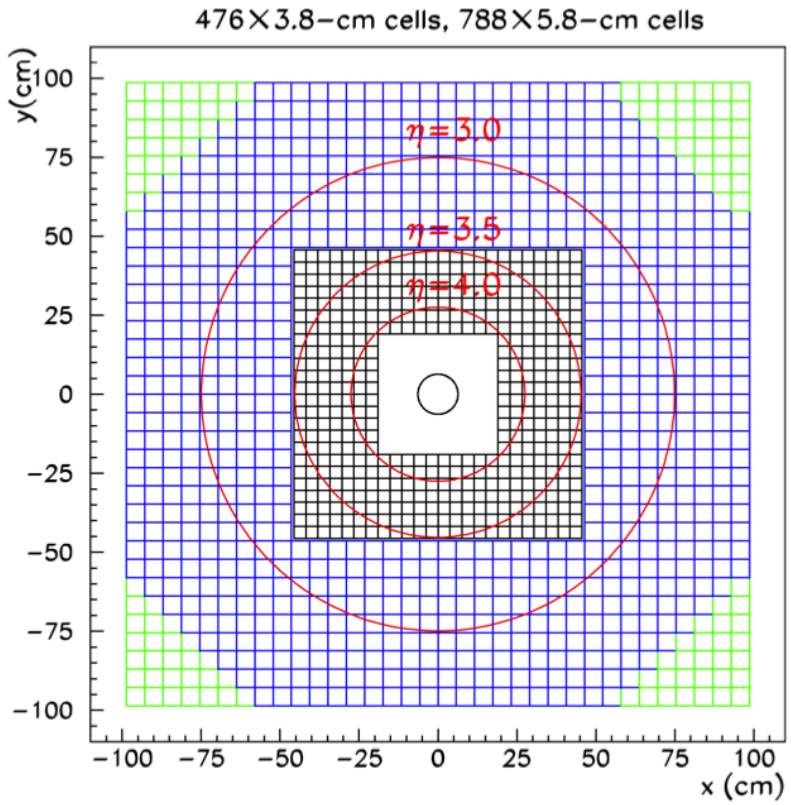

Figure 5.13: The schematic view of the FMS. The FMS was placed on the STAR west platform after dismantling the FPD++.

Some care has to be taken in comparing the results since two key differences exist between the FMS and the FPD++: the geometry and the trigger scheme. It is from this reason that the results for the invariant mass are very difficult to compare. The result for the jet profile should be very similar since it is mostly a property of the jet and not so much of the detector. To illustrate the differences, the results obtained with the FMS are given on figures 5.14 and 5.15.

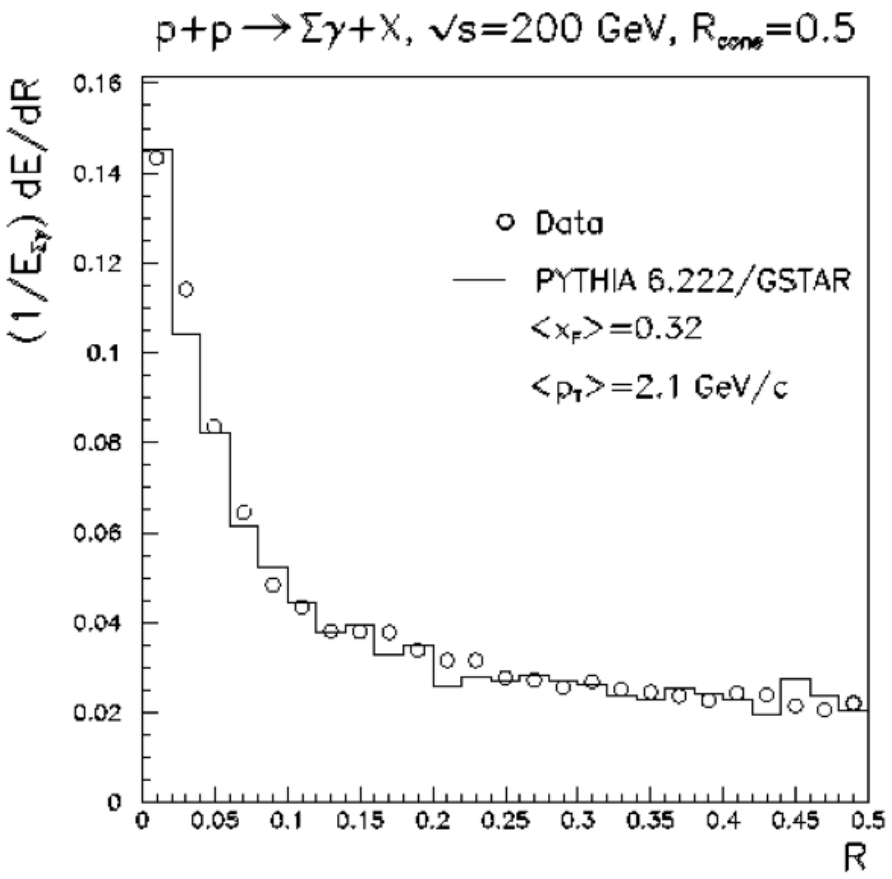

Figure 5.14: The jet profile result obtained with the FMS. Shown on the image are both the data and simulations.

One can see that in the FMS, as well as in the FPD++, the result for the jet profile has the same shape and the data and simulations agree well.

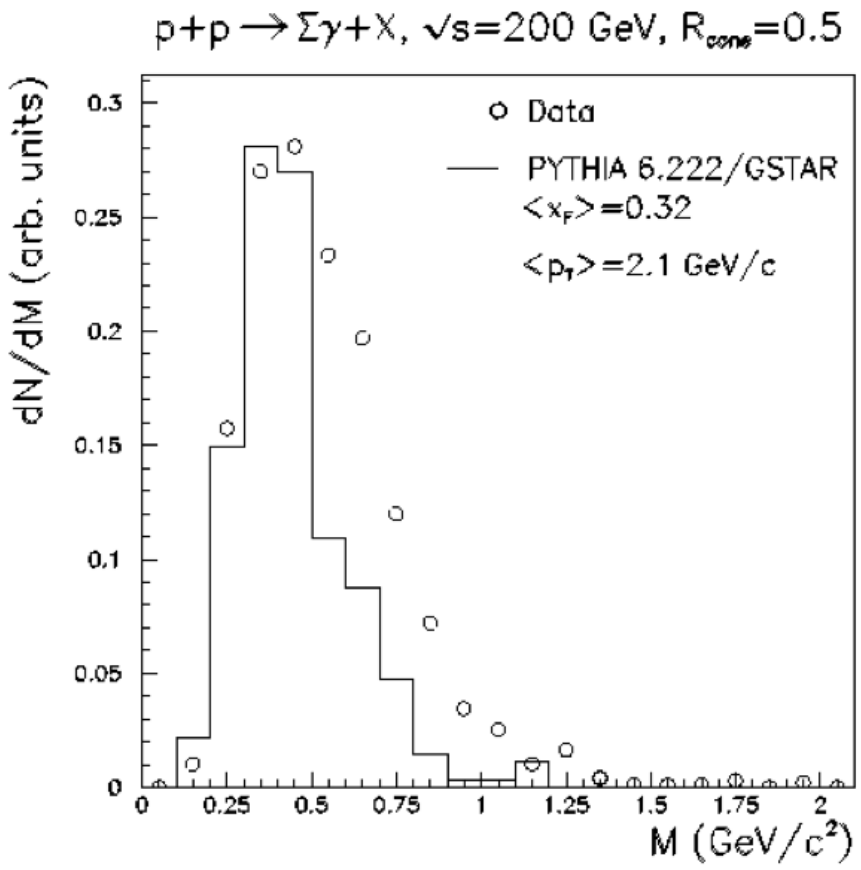

Figure 5.15: The invariant mass of the multiphoton event result obtained with the FMS. Shown on the image are both data and simulations.

The result for the invariant multiphoton mass in the FMS has significant differences compared to the FPD++ result. First, the shape of the distribution is more "peaky", rather than "Gaussian". Second, the average value of the invariant mass is higher, and third, the data are consistently above the simulated prediction. The reasons for the differences should be looked for in the differences of trigger and geometry.

The FMS trigger was a hightower trigger. The thresholds for triggering were 200 ADC counts for large cells and 400 ADC counts for small cells. If any of the cells had satisfied one of these conditions, the event would get read out. The average gains and thresholds of the FMS are given in table 5.1.

Cells	ADC count threshold	Av. gain (GeV/count)	Av. en. threshold (GeV)
North-inner	400	0.090	36
South-inner	400	0.091	36
North-outer	200	0.145	29
South-outer	200	0.180	36

Table 5.1: FMS trigger characteristics

Two things were done in order to compare the FMS and the FPD++ results. First of all, the difference of trigger had to be taken into account. The FMS, as well as FPD++, consisted of large and small cells, but there is a significant difference in geometry in the FPD++ and the FMS. The FMS small cells extend out to 46.5 cm from the beam and the FPD++ small cells start appearing at 46.05 cm from the beam. This means that the placement of the FPD++ small cells, which served as trigger, corresponds to the placement of large cells in FMS, which has to be taken into account.

The averaged outer cells energy threshold for the FMS is 32.5 GeV. The energy incident upon a lead glass cell will be proportional to its surface. Since the ratio of cell front face sides is equal to (3.8/5.8), the ratio of energy incident upon a small and a large cell is equal to $(3.8/5.8)^2 = 0.43$. Accounting for this difference and the fact that the FPD++ small cells were placed where the FMS large cells are, the small cell threshold should be set to $32.5\text{GeV} \cdot (3.8/5.8)^2 = 13.95$ GeV. However, a trigger set up in this way has the problem that it is not a subset of the hardware FPD++ trigger. To make it so, pairs of neighboring small cells were taken into account with a threshold of 28 GeV. In the neighboring cells, the cells that touch on the diagonal were not taken into account. In this way, a trigger that mimics the FMS trigger and is also a subset of the FPD++ hardware trigger was set up. The result of this procedure is given in figure 5.16. This result is shown in a higher energy bin due to the fact that the statistics in the bin usually looked at are low. This fact stems from the strict combination of the FPD++ hardware trigger and the FMS simulated hightower trigger, which decreases the number of events down to 8% of the number when only the usual hardware trigger is satisfied.

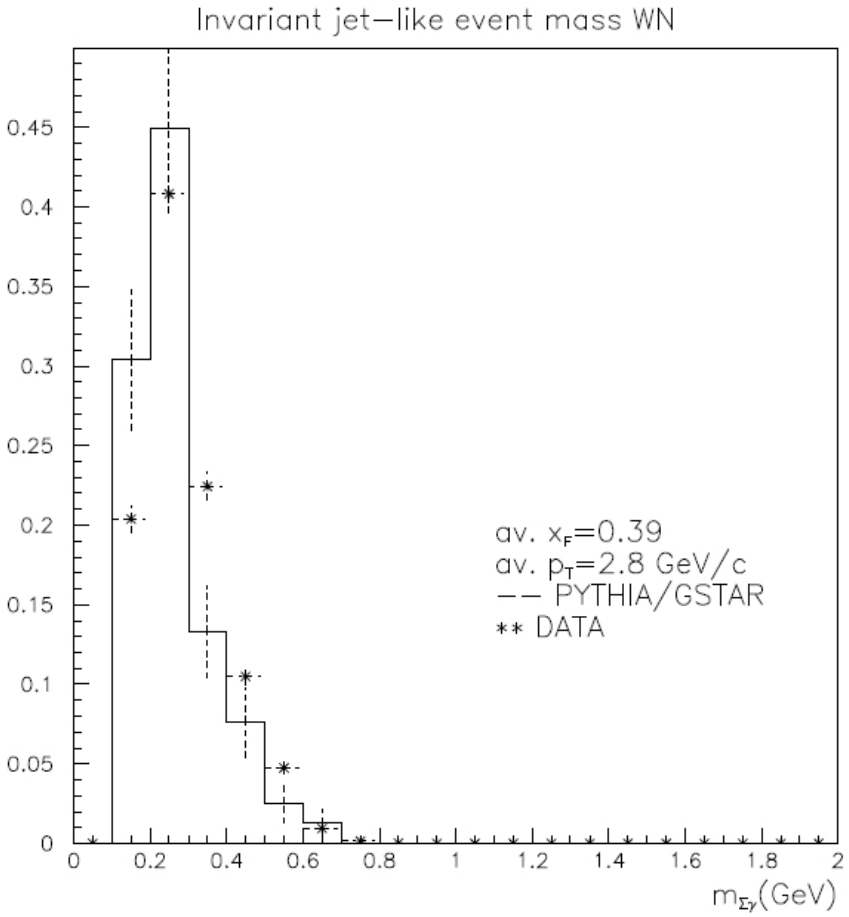

Figure 5.16: The invariant mass of the multiphoton event result obtained with the FMS mimicked trigger. Shown is a higher energy bin than usual due to lack of statistics in lower energy bins.

The result of this was that the invariant mass distribution is now shaped much more similarly to the FMS result. Earlier, the shape was "Gaussian", whereas now it is more "delta function" like. Also, in the falloff part of the spectrum, the data is systematically above the simulated prediction, as in the FMS result. Still, the average value of the invariant mass in the obtained mass is much lower than in the FMS results. This issue is most likely there because of the difference in geometry of the detectors and the "weighted multiplicity" cut.

The weighted multiplicity cut will produce different results in detectors with different geometry if one looks at, for example, the same x_F range of results. This is simply so because the weights of the large and small cells are different and the admixtures of the two types will be different in detectors different geometries. Looking at the FPD++ analysis, one can see that the detectors in the multiphoton sample are mostly small cells, each weighted by 1. In the FMS, in the same x_F range, this is not the case; there is surely a more dominant admixture of large cells, each weighted by 1.52. So, to mimic that, the weighted multiplicity cut in the FPD++ was raised from 10 to 15. The results obtained in this way have shown that the average invariant mass rises significantly, but also that the statistics in a given energy bin fall rapidly (down to 8.5% of the number of events when the weighted multiplicity cut is equal to 10). Due to a relatively small simulation sample, it was not possible to further compare the data and simulations. The results obtained in the data were compared to results in the data obtained in the FMS and are given on figure 5.17.

This result shows that the higher multiplicity cut moves the average invariant mass value higher. In conclusion, it was shown that the FMS mimic trigger, as opposed to the FPD++ trigger, produces distributions that are "peaky", as in published FMS results. The mass value of the peak is too low, most likely due to the multiplicity cut. Increasing the multiplicity cut produces higher average mass values, as those of the published results. The spectra have the same data/simulations behavior; namely the "falloff" part of the spectra show data points systematically above simulated points.

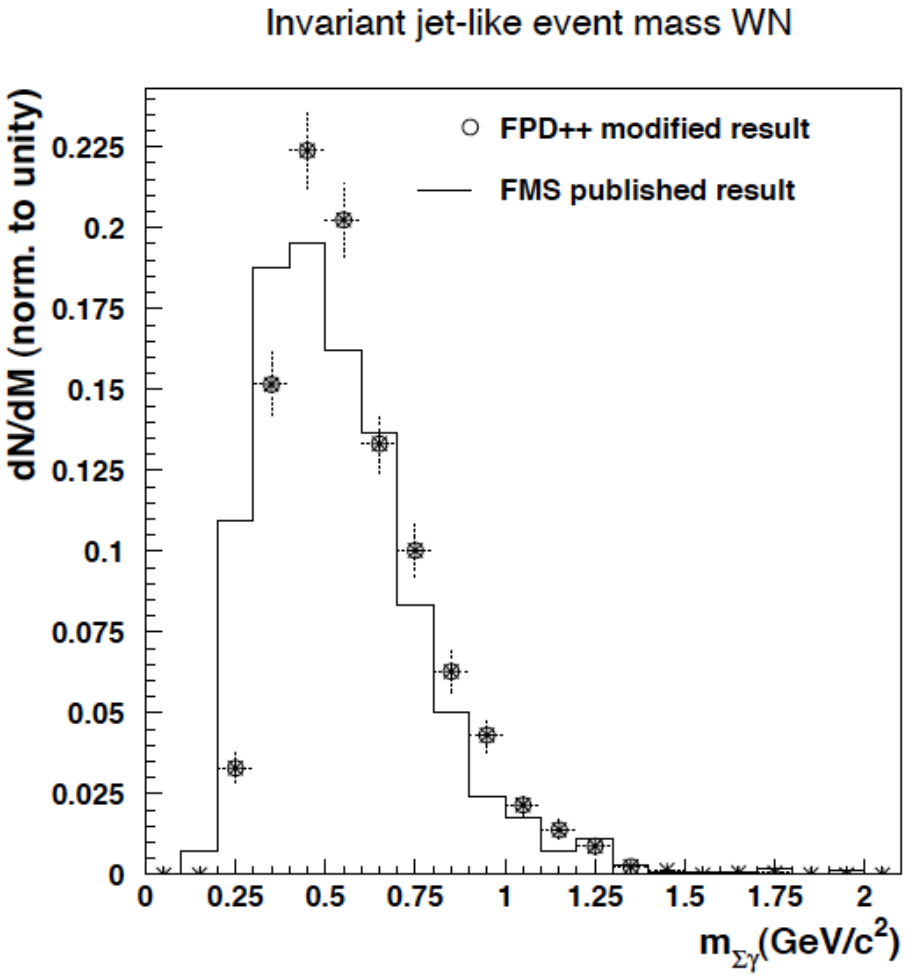

Figure 5.17: The invariant mass of the multiphoton event result obtained with the FMS mimicked trigger with a higher multiplicity cut compared to the FMS obtained result. The error bars on the data points are statistical.

5.2.2. Unpolarized results - potential impact of imperfections

As mentioned before, a feature was present in the unpolarized multiphoton results; the effect that the jet energy profile distribution starts to slowly rise again near the boundary of the jet cone, i.e. close to R=0.5 in the WS module. This is shown in figure 5.18.

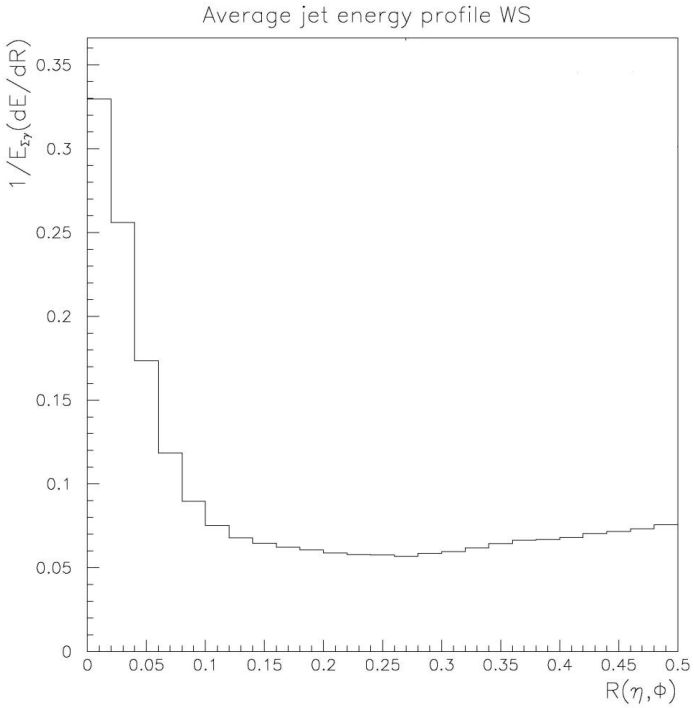

Figure 5.18: The WS module "jet tail" feature. Shown here is the distribution summed over all energy bins. One can see that the expected falloff spectrum at high R is not present; instead there is a slight rise of distribution towards the end of the cone the multiphoton event is in.

This effect was thoroughly investigated. The distribution from figure 5.18 was split into energy bins, as defined earlier. As it turns out, in the higher energy bins, the tail is more and more pronounced. In the lowest energy bins, there is no tail at all. This lead to the conclusion that the jet tail is an effect coming solely from the large cells; first because it appears at large R, in the large cells, and second, because it increases with increasing energy, and in the higher energy bins more and more energy comes from the large cells.

By looking at the dependency of $1/E_{\mathrm{mp.}}(\mathrm{d}E_{\mathrm{mp.}}/\mathrm{d}R)$ vs. ϕ' in the WS module revealed that there is an isolated ϕ' area where there is a lot of deposited energy. To make a thorough investigation, for each multiphoton event all the towers had their energy deposition recorded in a two dimensional histogram.

It was found that there is an area in the detector where a lot of energy comes from. This was later identified as an area with 4 cells in a 2 x 2 square that have high correction factors and hence, for example, improper diphoton invariant mass histograms. Simply removing these cells from the detector removes the jet-tail issue. Effort was undertaken to improve their correction factors and in this way remove the jet tail, while keeping the cells "live", thus improving the result.

This points out the possible impact of imperfections of the detector on the results obtained. Non uniform calibration, dead cells, noise in the detectors and similar effects can have impacts, so all of these were closely looked at and monitored in all analysis steps.

As far as comparison to simulations is concerned, it was found that it depends on the amount of noise simulated at the level of a few percent. In the simulations, one can introduce as much artificial noise as wanted, but finding the amount that will best represent the data is difficult since the noise in the real detector can depend on many variables. Hence, the results presented here are obtained without simulated noise, keeping in mind that the agreement with data could be different at the order of a few percent.

5.3. Spin-sorted results

5.3.1. Spin-sorted results obtained with the FMS

Just as for the unpolarized results, the FMS was used to obtain spin-sorted results as well. To obtain the asymmetry with the help of the cross ratio method, the FMS was divided into octants, as in figure 5.19.

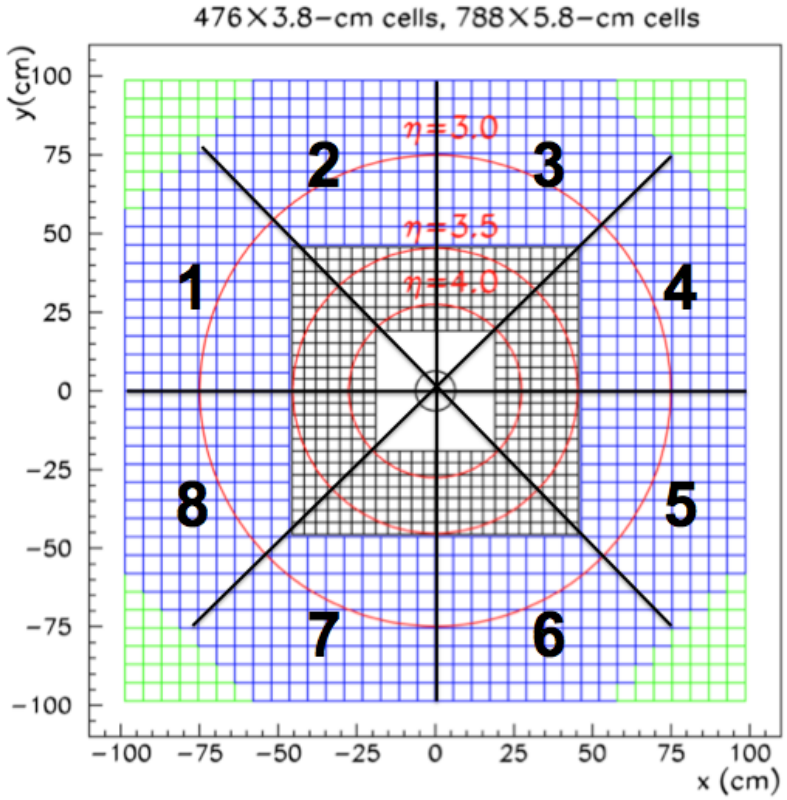

Figure 5.19: The division of the FMS used to obtain the asymmetry. The asymmetry as a function of ϕ was obtained using pairs if azimuthally opposite octants, such as 1-5. The asymmetry as a function of x_{F} was obtained by integrating over all such pairs.

Pairs of azimuthally opposite octants, such as 1-5 or 2-6, were used to calculate the asymmetries. In this way, the asymmetry as a function of the STAR angle ϕ was obtained. Further, the asymmetry as a function of x_{F} was obtained by integrating over all such pairs [52].

The asymmetry was calculated as a function of x_F to verify consistency with the previously published results [8], showing the rise of asymmetry with rising positive x_F, and an asymmetry consistent with zero for negative values of x_F. Further, the FMS was used to test the ϕ angle dependence of the asymmetry, with ϕ being the STAR (azimuthal) angle. This provided the first chance through the full forward calorimetry project to look at "polarimetry"; i.e., the $< \cos(\phi) >$ dependence. The expectation is that the asymmetry will be modulated by $< \cos(\phi) >$, as described in the Theory chapter. This calculation is fully analogous to the $< \cos(\gamma) >$ dependence, where γ is the Collins angle, which is the primary result of this thesis. The results obtained with the FMS are given in figures 5.20 and 5.21.

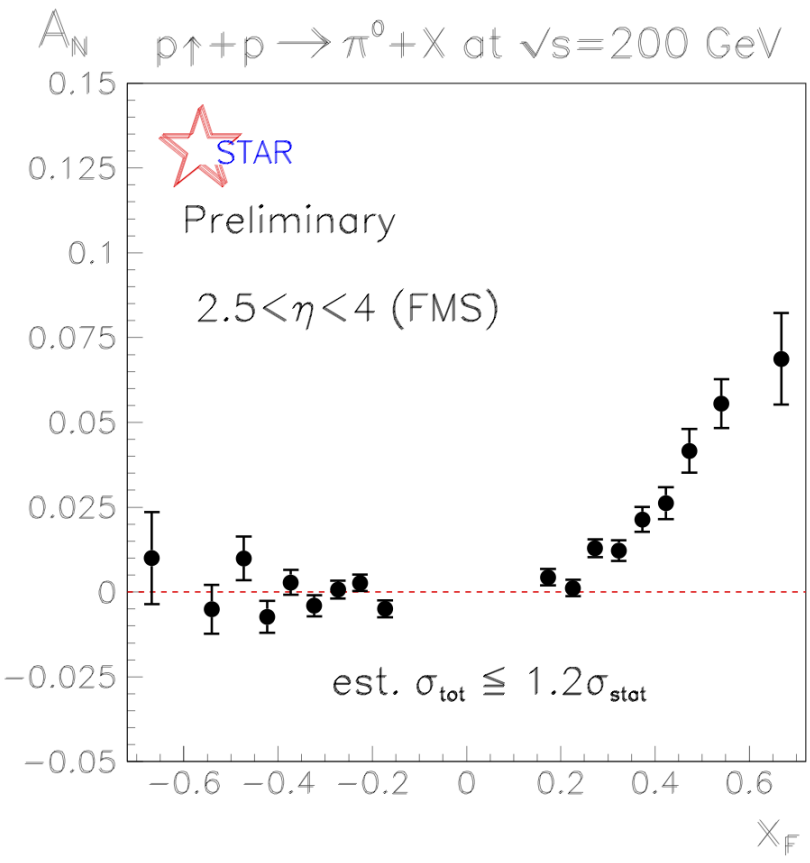

Figure 5.20: The asymmetry as a function of x_F, obtained with the FMS [52]. This result was obtained by integrating the calculated asymmetries over all octant pairs. The error bars are statistical. The asymmetry is consistent with the results obtained in [8].

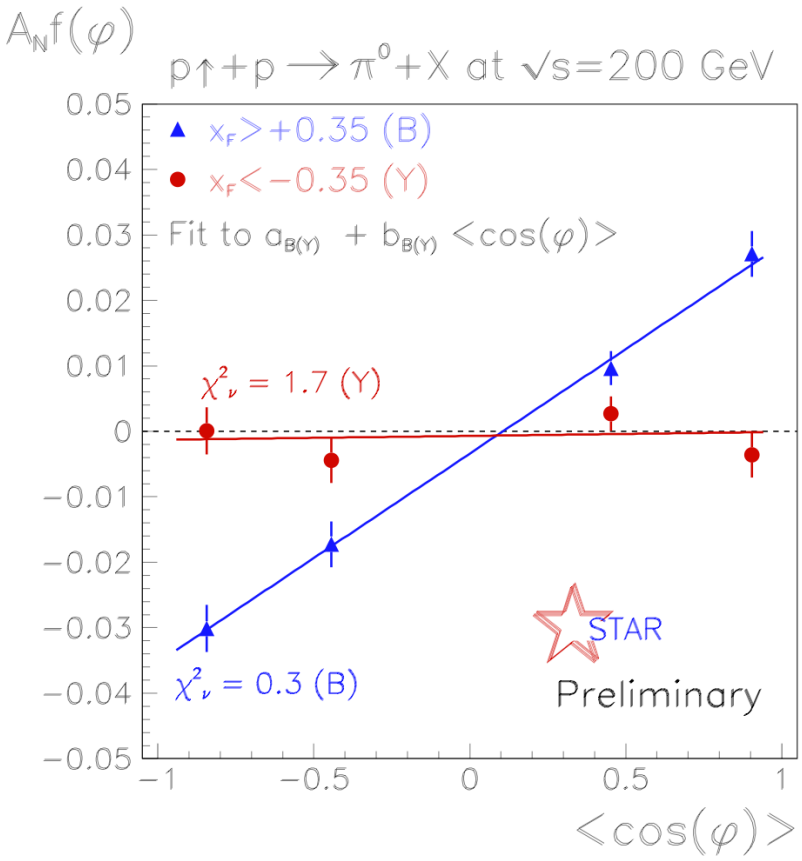

Figure 5.21: The asymmetry as a function of the STAR angle ϕ, obtained with the FMS [52]. The lines show fits to the function $a+b < \cos(\phi) >$. The goodness of the fits is indicated with the chi-squared values. The positive x_F asymmetry exhibits linear dependence on $< \cos(\phi) >$, while the negative x_F show no dependence. The error bars are statistical.

One can see that the asymmetry as a function of x_F is consistent with previously published results ([8] of figure 5.1). The positive x_F asymmetry is linearly dependent on $< \cos(\phi) >$, while the negative x_F shows no dependence on it, as expected.

5.3.2. Event selection and asymmetry

The next step in the analysis was to look at events from which one can determine the Collins angle. To do that, one has to insure that there is a leading neutral pion event in the same calorimeter in which there is a multiphoton event. In addition to the "unpolarized multiphoton event" cuts, a requirement was made to have a neutral pion reconstructed in the same module where the multiphoton event was found.

An event sample that was a subsample of the data for the published neutral pion results was made. This subset was produced in such way that in addition to the previously made cuts that defined the "neutral π^0" dataset a requirement was made that the large cell readout was "live". For this newly obtained dataset the spin information was read in and the asymmetry as a function of x_F was calculated. This was done for both the west detectors (FPD++) and the east detectors (FPD). This result is shown in figure 5.22, and the specific values of the calculated asymmetries are given in the Appendix.

It is visible from figure 5.22, comparing with the figure 5.1, that the "large cell live" condition didn't change the dependence of asymmetry on x_F. This is an important result, since it shows there is no systematic effect on asymmetry of large cell dead time. One can then be sure that no asymmetry will be introduced by this condition and can proceed to look at π^0+ multiphoton event in the same calorimeter. There is an important difference in the results given here and those from the published π^0 data. One can note that the result for the east lowest energy bin is in this case missing. This is simply so because the published result used not only data from Run 6, but also segments of data from Runs 3 and 5, from which the lowest energy bin result was extracted.

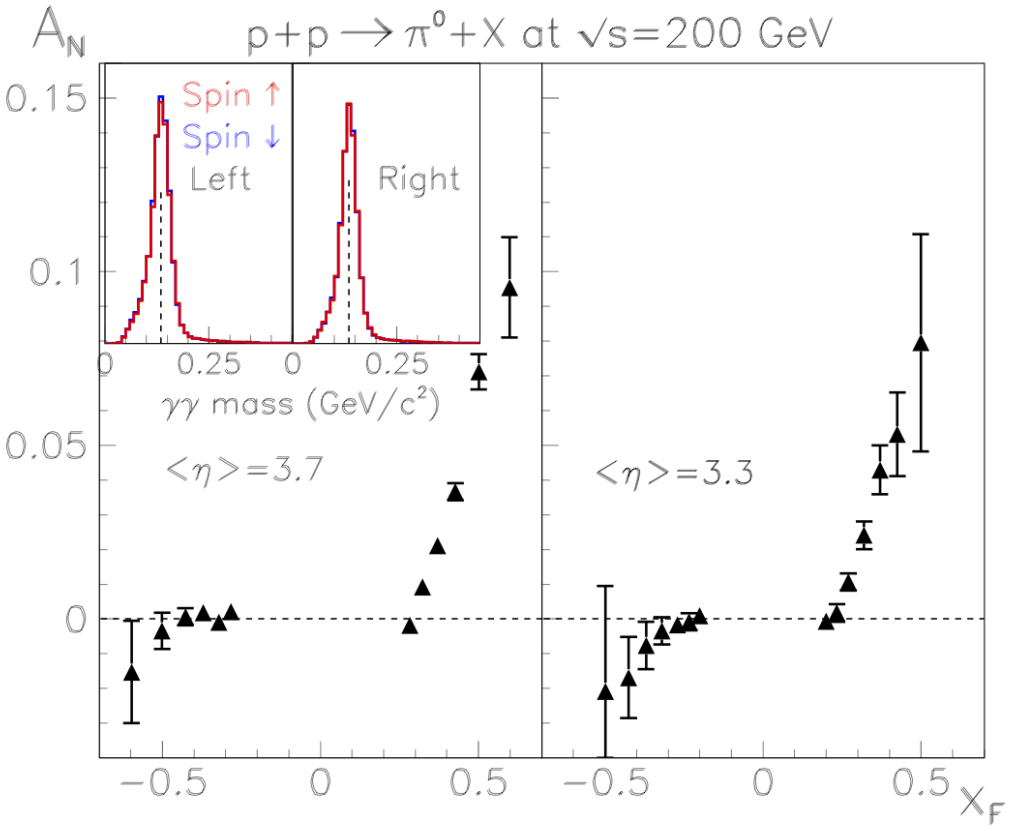

Figure 5.22: The asymmetry as a function of x_F for the neutral pion sample with the large cell "live" condition. The events in this figure are a subset of the events used in figure 5.1. The lowest east energy bin point is not present in this figure since only data from Run 6 was used, whereas in the published inner cells π^0 result portions of data from Runs 3 and 5 were used, from which the lowest energy point was extracted. The inset in the figure shows examples of the spin-sorted di-photon invariant mass distributions. The vertical lines in the insets mark the position of the π^0 mass. Intercomparison of figures 5.1 and 5.22 establishes that there is no spin dependence to the dead time for the large cell readout.

5.3.3. The Collins angle results

Looking at the data sample with the conditions that there is a reconstructed neutral pion in the same calorimeter as the reconstructed multiphoton event, one can look at the Collins angle. Other than the Collins angle, one can also look at the differences of reconstructed physical variables for the π^0s and the multiphoton events (energy, invariant mass, transverse momentum etc.). By making additional requirements on some of these differences one can assure that the multiphoton event is more "jetty". Since both the pion finder and the multiphoton finder are pattern recognition algorithms, they can find the same event. It is imaginable that the multiphoton finder could recognize a single pion as a multiphoton event, given that it satisfies all the imposed cuts. The "jettiness" of the event will be improved if the differences of physical variables of the π^0 and the multiphoton are as large as possible. This, however, will also severely limit the statistics of the sample. The difference distributions results and the Collins angle distribution given here were obtained with a cut on the difference of energies of the multiphoton and the pion of at least 1 GeV.

Before looking at the Collins angle directly, a conclusion can be drawn about the shape of its' distribution. On average, a large fraction of energy of a multiphoton event comes from the leading pion. The pion will, hence, for the same average x_F as the multiphoton event, have on average a larger p_T. This means that the pions intercept point will get reconstructed further from the beam than the multiphotons jet intercept point. Since this corresponds to Collins angles ≈ 0, it is to expect that the Collins angle distribution will be much larger near $\phi_C = 0$ than near $\phi_C = \pm\pi$. This behavior is basically independent of the cuts chosen, as long as they are reasonable and the multiphoton event is "jetty" enough, and can be seen in all the Collins angle distribution results. Local non-uniformities of the distribution can arise from detector effects, dead cells, calibration etc.

The results were obtained for the difference distributions and the Collins angle distributions both in data and simulations. Given on figures 5.23-5.25 are the difference distributions of the energy and the invariant mass and the Collins angle distribution for the WN detector.

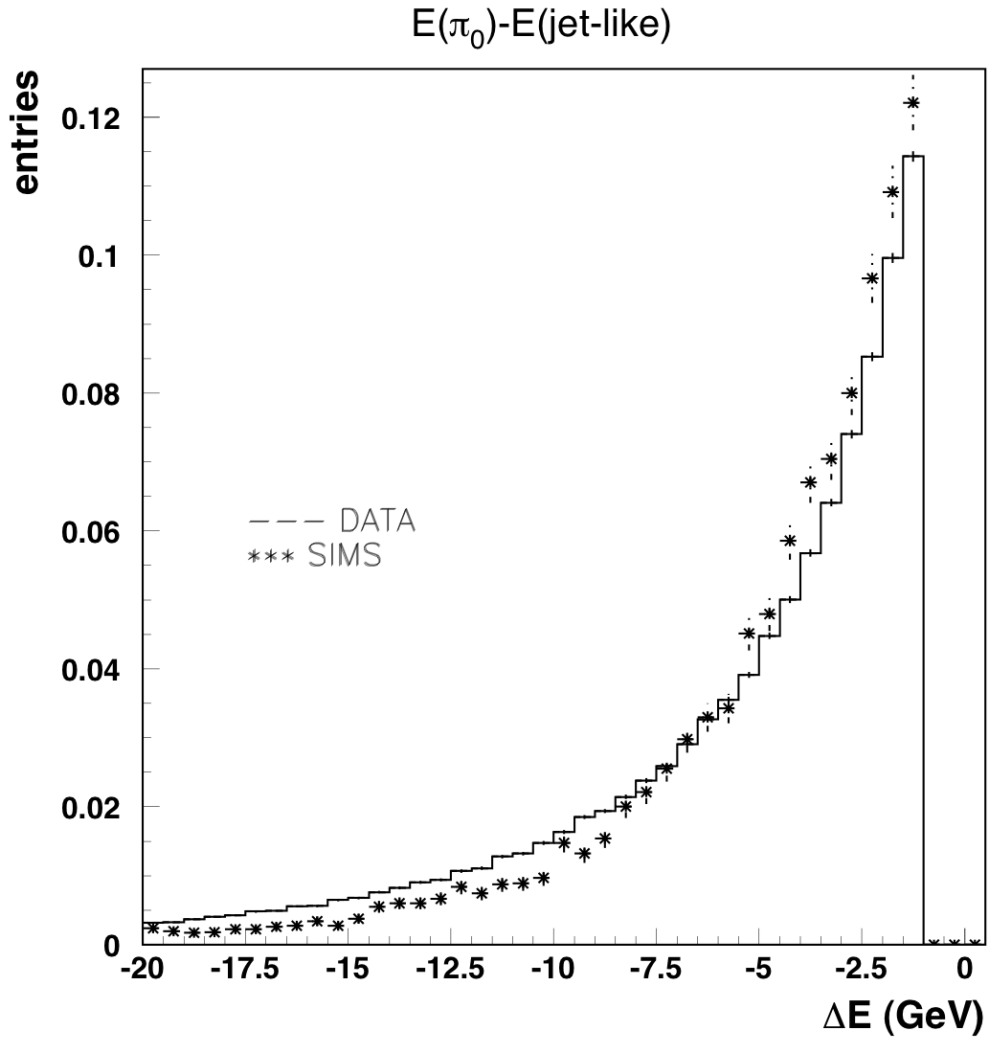

Figure 5.23: The distribution of the difference of energies of the multiphoton and the π^0. The data and simulations show agreement. There is a visible cut at ΔE=1 GeV. The error bars are statistical.

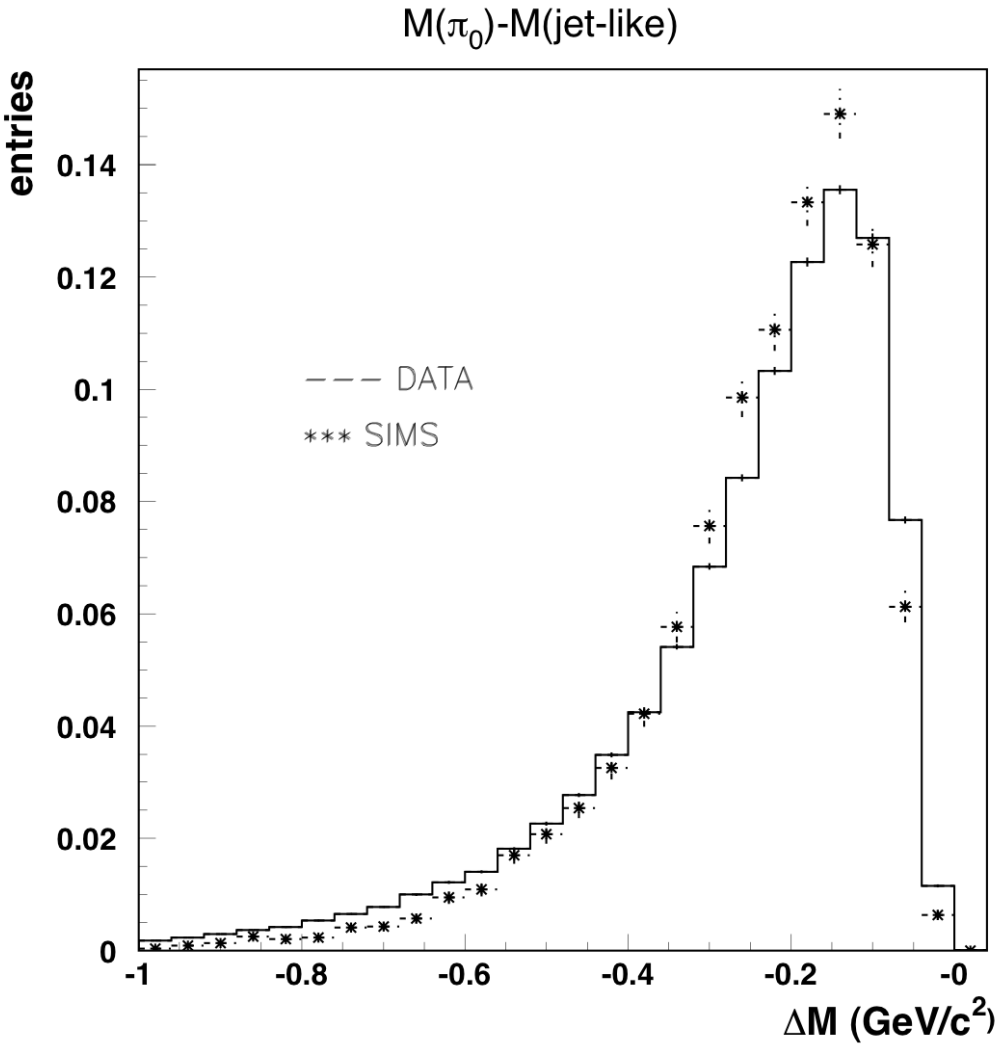

Figure 5.24: The distribution of the difference of invariant masses of the multiphoton and the π^0. The data and simulations show agreement. The error bars are statistical.

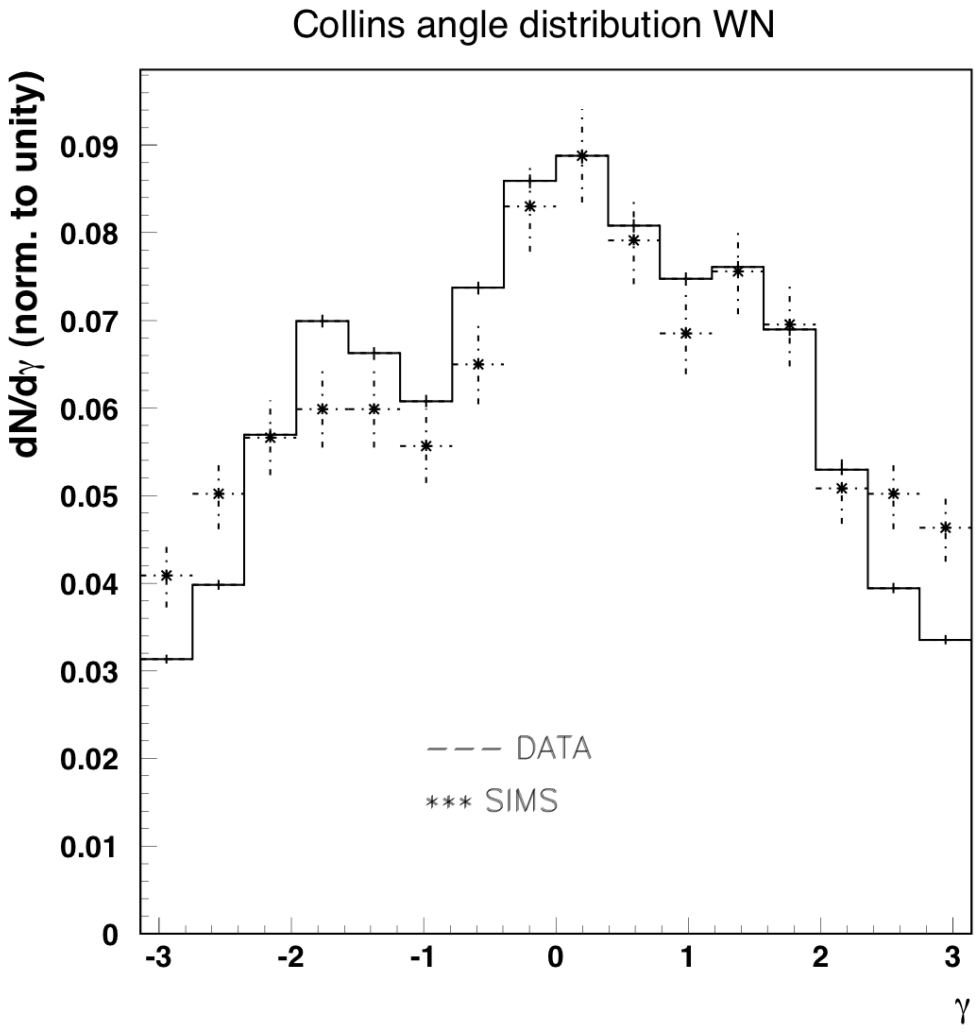

Figure 5.25: The distribution of the calculated Collins angle in the WN detector. The data and simulations show agreement. The distribution is behaving as predicted by the fact that the π^0 carries most of the transverse momentum of the event. The error bars are statistical.

5.3.4. The asymmetry results

In general, all unpolarized quantities show good agreement with the simulated sample of events and are behaving as predicted. The calculation of asymmetry now took place, as described in the Data analysis chapter. The results for each bin have been integrated over all energies for $x_F > 0.3$. The result is given in figure 5.26.

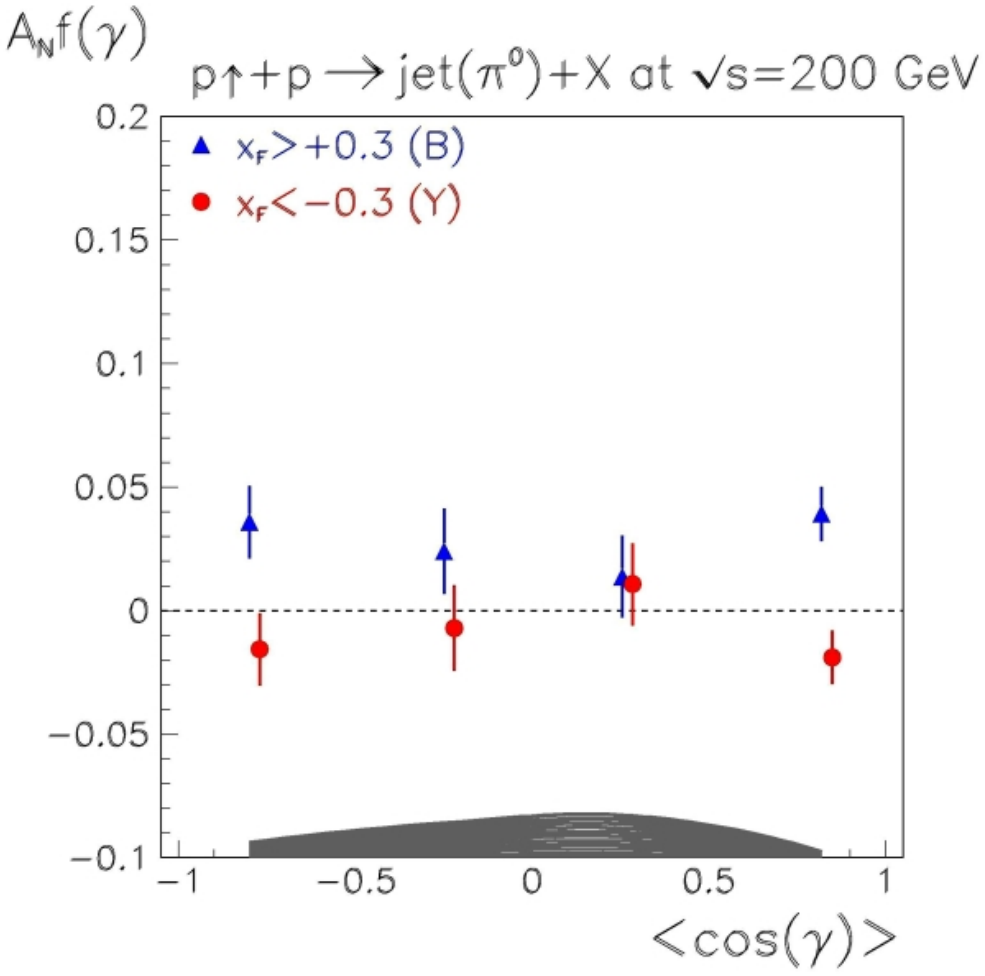

Figure 5.26: The calculated A_N as a function of $\cos(\gamma)$. The blue points correspond to the positive x_F values, the red points to the negative x_F values. The error bars on the points are statistical and the gray shaded area shows the systematical errors. The points for $x_F > 0$ and $x_F < 0$ have been slightly horizontally offset, so that all points are clearly visible.

The results shows that the asymmetry for the negative x_F values is consistent with zero, as expected. The positive x_F asymmetry is greater than zero in all points, with an average of 0.031 ± 0.014. The error bars drawn on the points are purely statistical; the systematical error is given with the gray shaded band. By making the analysis of systematic errors, as described in the "Data analysis" chapter, it was found that the main source of the error lies in the uncertainty of the large cell calibrations. Hence, for the points in the figure, the height of the gray shaded band represents the maximal systematic error obtained by modifying the calibration factors by 10%. The points for $x_F > 0$ and $x_F < 0$ have been slightly horizontally offset, so that all points are clearly visible. All the calculated asymmetries and errors are given in the table 5.2.

Bin	$< \cos(\gamma) >$	$A_N(x_F > 0)$	$A_N(x_F < 0)$	Stat. error	Syst. error
1	-0.80	0.0358	-0.0156	0.0147	0.0061
2	-0.25	0.0241	-0.0071	0.0172	0.0140
3	0.25	0.0137	0.0107	0.0165	0.0172
4	0.82	0.0391	-0.0189	0.0108	0.0024

Table 5.2: The calculated asymmetries and the errors.

There is no linear dependence of the positive x_F asymmetry on the $\cos(\gamma)$ bin. This means that the Collins contribution to the asymmetry is not present, isolating the Sivers effect. The absence of signatures of the Collins effect is not unexpected for neutral pions, in light of what has been found in e^+e^- and in semi-inclusive deep inelastic scattering. A combined analysis of e^+e^- and SIDIS shows that leading Collins functions (up quark fragmenting into a π^+ and down quark into a π^-) have opposite signs to subleading Collins functions (up quark fragmenting into a π^- and down quark into a π^+) [53]. In the Artru model, leading and subleading Collins functions are expected to have the same magnitude. Since π^0 is both leading and subleading (in other words, it is its own antiparticle), it is not at all surprising that the Collins effect vanishes due to cancellations between leading and subleading Collins functions. This result is also consistent with the absence of a Collins signal in SIDIS.

5.3.5. Potential impact of cut selections and imperfections on the polarized results

Just as in the unpolarized results, the imperfections of the detector could influence the results. It is very likely that local non-uniformities in the results for the Collins angle come from detector imperfections, such as noise or calibration non-uniformities. The investigation of noise can be, and was, done with the help of simulations. Many physical observables show better agreement in the data and simulations when there is some simulated noise in the simulation reconstruction procedures. This, in turn, produces more local non-uniformities in the detector and the result it produces. Still, effects of this magnitude won't affect the final conclusion, but possibly only slightly shift the points and influence the error bars.

The other thing that can influence the results is the set of cuts used to obtain them. The parameter space of the cuts is large and was widely explored. Alongside the neutral pion cuts, that were used in previous analyses, such as the published Run 6 analysis, there are the additional sets of cuts that get imposed to get the multiphoton events, as well as the difference cuts that ensure the "jettiness" of the event. The multiphoton cuts were chosen to be the same as used for the FMS analysis, to be able to compare current results with previous results. Also, they isolate the multiphoton events very well. From the multiphoton cut set, the weighted multiplicity cut was looked at in greater detail. It was demonstrated that decreasing it from the usual value of 10 to the value of 9 doesn't visibly change the event properties, but adds significantly to the statistics (order of 20%). The result quoted in the text is given with the cut of 10.

The difference cuts are the ones that still needed exploring. Earlier evidence suggested that the jets containing the neutral pions have on average 2 GeV energy more that the neutral pion itself [50]. So, it is reasonable to impose a difference of energy cut on the reconstructed multiphoton event and the neutral pion. This cut, as well as the cut on the difference of invariant masses, was explored. It was demonstrated that the "mass difference" cut is much stricter than the "energy difference" cuts in terms of statistics, so it was left aside. The difference of energy cut has shown that for every increase of 2 GeV in the cut, the number

of reconstructed events falls by roughly 35%. This cut was set to 1 GeV, which constituted a good compromise between "jettiness" of the event and the statistics of the sample.

Acceptance asymmetries

Another imperfection one should look at are significant differences between the detector modules. An observable that can reveal these differences is the acceptance asymmetry of the detectors. This is defined as the difference of number of events for a given bin (energy or Collins angle) in two detectors divided by their sum. If there is a particular detector in a module that is very specific (for example, with a lot of noise in it) it will be seen in this asymmetry. The asymmetry was looked at as a function of the Collins angle, since this is the natural variable the results will be presented in. The cuts used to obtain the result are the same ones as used for the data analysis.

If there are no acceptance asymmetries, it is expected to get a flat distribution with an average value of around 0.17. The value should be different than zero, since the trigger is such that on average the WN detector will record more events than the WS. The number of 0.17 is obtained from the total number of events on WN and WS. The result is given on figure 5.27.

On figure 5.27, the line represents the average value of the distribution. One can see that there are deviations from the perfect detector. However, they fall within $\pm \approx 5\%$ of the expected value of 0.17, which is acceptable. Still, one has to keep in mind that this should alway be closely observed, since a single non-functioning cell, which appears to be functioning, could greatly affect the final result.

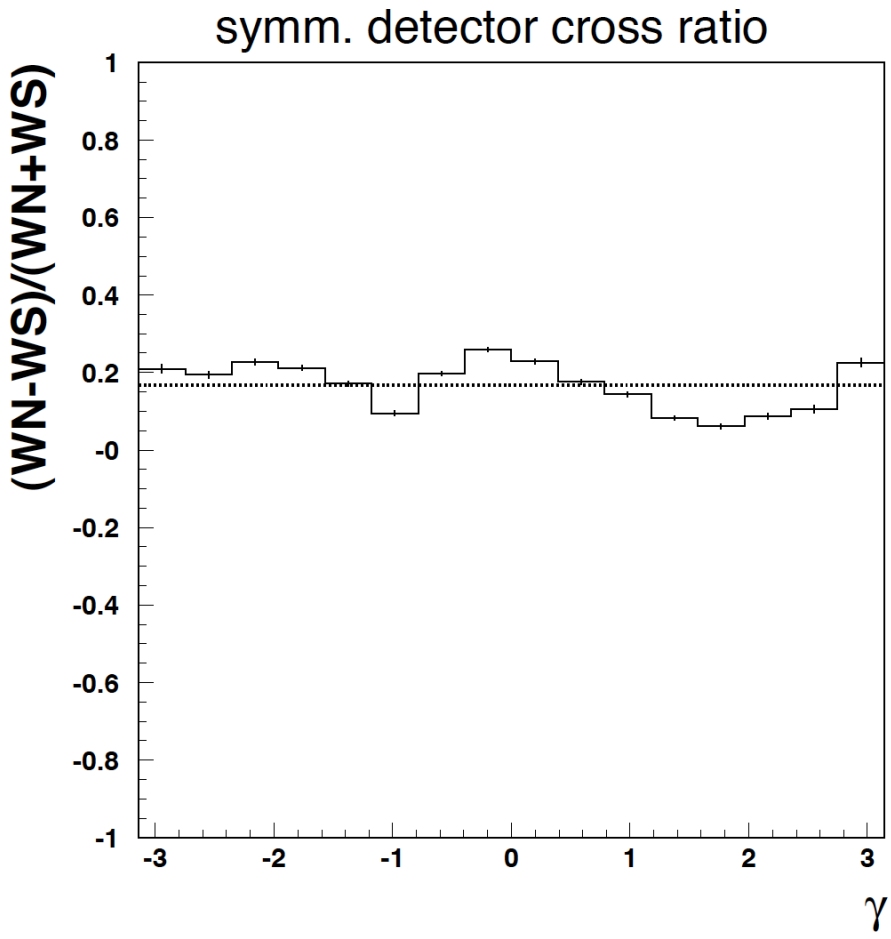

Figure 5.27: The calculated acceptance asymmetry. The cuts used to obtain the result are the same ones as used for the data analysis. The errors bars are calculated from statistical errors of the measurements. The line represents the average value of the distribution.

Chapter 6.

Conclusion and Outlook

So far, there has not been a complete description of the proton spin in terms the spin and orbital motions of quarks and gluons. Polarized deep inelastic scattering experiments have shown that the quarks carry only a fraction of the proton spin [1, 2, 3]. It was suggested that the gluon spin and the orbital motions of quarks and gluons carry the rest of the proton spin. The so-called "spin puzzle" is still not solved, but it is confronted from many sides.

One of the ways of approaching the solution of the puzzle is via the spin asymmetries. The first greatly unexpected result, giving large values of the asymmetry, was observed at Fermilab in the E704 experiment [4]. This spurred large developments in theory and gave reason to conduct experiments that would better measure and explain the effect. Working in an energy regime where the experimental cross section data agree well with the NLOpQCD predictions, the RHIC collider is an ideal place to explore the phenomenon.

Theoretical developments since the E704 results have modelled the asymmetry, with two leading concurrent models being the Sivers effect and the Collins effect. In essence, the Sivers effect relies on the parton distribution functions to produce asymmetry, whereas the Collins effect relies on the fragmentation to produce it. In some experimental aspects, the two models are indistinguishable and can produce nearly the same net results for some observables. One of such is the single spin asymmetry for the neutral pions at forward angles. Precision measurements of this asymmetry at high rapidities have been reported [8], showing that the

asymmetry rises with rising positive x_F and is consistent with zero for negative values of x_F, as models predict. The p_T dependence of the asymmetry was also found, but it was not in accordance with models. In any case, the inclusive neutral pion asymmetry did not allow to distinguish between models, so one had to look beyond them at jets or direct photons.

In the work presented in this thesis, I have looked at forward "jet-like" events to distinguish between two models. In essence, a spin-correlated asymmetrical distribution of particles within a jet would indicate a Collins contribution, whereas an angle-independent distribution would indicate a Sivers contribution. This analysis was done using data obtained with the Forward Pion Detector ++, an electromagnetic calorimeter placed at forward angles in the STAR detector at RHIC. The important thing to note is that the observable in question depends on the azimuthal angle within a jet. This angle is called the Collins angle and is defined as the angle of a produced particle with respect to the fragmenting parton producing the jet. It was shown that the direction of the produced particle (in this case the leading π^0) and the direction of the fragmenting parton are reconstructed well, even though the experimental setup does not allow for a full jet reconstruction, but only emphasizes the electromagnetic contribution. With a good reconstruction of the directions of the leading particle and the fragmenting pion, one can access the Collins angle within these "jet-like" events and look at the dependence of asymmetry on the Collins angle.

Several steps were taken before looking directly at asymmetries. The definition of the "jet-like" multiphoton events was thoroughly explored and all the results obtained for these events were intercompared with results obtained previously with the Forward Meson Spectrometer [52]. After verifying consistency with previously published results, the spin asymmetries were extracted. The asymmetry as a function of x_F for the events used to obtained the result, which are a subset of the data used for the result published in [8], has shown that there are no unwanted detector produced asymmetries and has proven consistency with the published results. Finally, the asymmetry as a function of the Collins angle was calculated. The final result shows that the asymmetry for negative x_F values is consistent with zero, as expected, while the asymmetry for the positive x_F values is consistently greater than zero, and shows no Collins angle dependences. This final result is not totally unexpected. As argued in the

Results chapter, the neutral pion is its own antiparticle, and if the leading and the subleading contributions to the Collins asymmetry are opposite in sign and equal in magnitude, the net Collins contribution to the asymmetry is zero.

The result is another piece of the spin puzzle, hopefully of large interest to the spin community. Pieces are still missing, but the puzzle is getting more and more complete.

The future prospects of the project include many things. First of all, given that RHIC will move to a higher energy ($\sqrt{s} = 500$ GeV), it would be beneficial to exploit existing capabilities to establish if the A_N continues to be large for positive x_F at this energy. The possibility to find pions at these energies depends on the possibility to reconstruct the photons that it fragments to. It has been demonstrated that the photons at these energies can be detected individually with the use of the Shower Maximum Detector (SMD), which is currently placed in front of the FPD.

Further, the next step in jet reconstruction and Collins/Sivers separation would include a full jet reconstruction. This can be done if one introduces a detector that is sensitive to hadronic response, instead of having only an electromagnetic detector. Such a step was carefully planned and is currently under way. Simulations have shown that with the proposed upgrades to the existing electromagnetic detector, combining hadronic and electromagnetic energy does measure the scattered parton energy very well, limited mostly by fragmentation effects. The prediction is that the first jet reconstructions will be looked at during the RHIC Run 11.

Finally, there are more physics goals that will get looked at with time. We would like to test the prediction that A_N for forward photon production will be negative. Detecting direct photons rules out fragmentation functions, so it is also a test of Sivers/Collins contributions. Next, the world is waiting to see if there is a sign change of the asymmetry relative to SIDIS in Drell-Yan. Both of these goals have undergone serious study and have been simulated, to find that they are feasible. It is very likely that we can see these results in the near future.

Chapter 7.

Appendix

7.1. Electromagnetic showers

The overview of electromagnetic showers and passage of radiation through matter was mostly adapted from C. Amsler et al. (Particle Data Group), PL B667, 1 (2008). High-energy electrons (more than a tenth of a GeV) predominantly lose energy in matter by "bremsstrahlung" and high-energy photons by pair production. The characteristic amount of matter traversed for these related interactions is called the radiation length X_0, measured in g/cm^2. This distance is both (a) the mean distance after which the electron energy has dropped to 1/e of its initial energy, and (b) 7/9 of the mean free path for pair production by a high-energy photon [35]. X_0 is also an appropriate scale length for describing high-energy electromagnetic cascades. X_0 is calculated and usually tabulated. One overview can be found in [54]. A compact fit to the data provided there was made by Dahl:

$$X_0 = \frac{716.4\,\mathrm{g/cm^2}\,A}{Z(Z+1)\ln(287/\sqrt{Z})}\,, \tag{7.1}$$

where A stands for the element mass number and Z for its atomic number.

In general, electrons (and positrons) lose energy by ionization and brehmssthralung, although other processes (Moeller scattering, Bhabha scattering, positron annihilation) con-

tribute, as shown in figure 7.1. One can see from the figure that above 100 MeV the only significant contribution comes from brehmssthralung. An electron loses energy by bremsstrahlung at a rate nearly proportional to its energy, while the ionization loss rate varies only logarithmically with the electron energy.

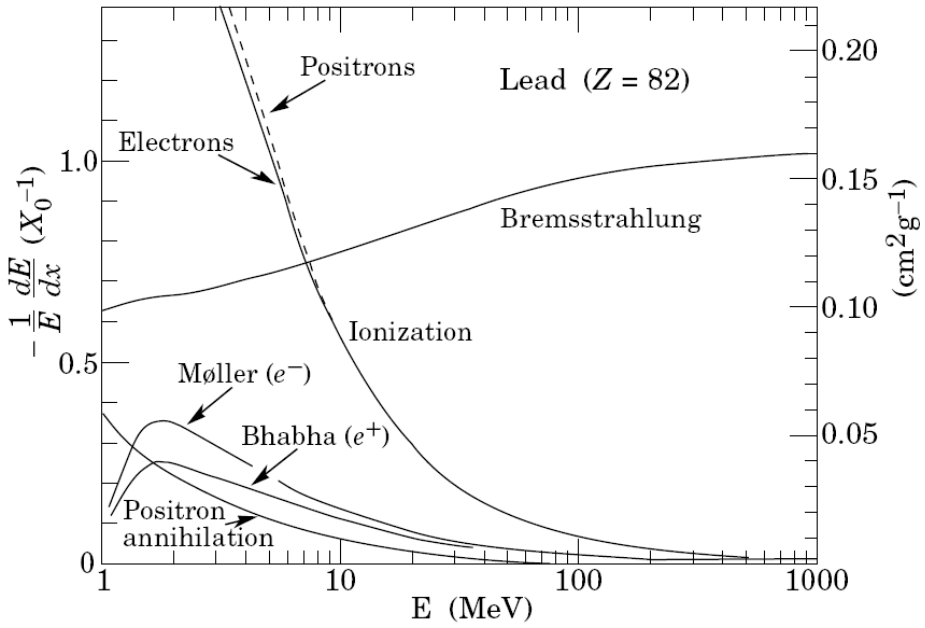

Figure 7.1: The contributions to electron (positron) loss in matter. Figure taken from PDG review.

The critical energy E_c is sometimes defined as the energy at which the two loss rates are equal [55]. The reference gives the approximation of

$$E_c = \frac{800\,\mathrm{MeV}}{Z + 1.2}\,. \tag{7.2}$$

There are alternative definitions of the critical energy, but they don't differ much in numerical values. Among alternate definitions is that of Rossi [56], who defines the critical energy as the energy at which the ionization loss per radiation length is equal to the electron energy. This form has been found to describe transverse electromagnetic shower development more

accurately. In case of lead $Z = 82$, so the critical energy is equal to about $E_c \approx 9.6\,\mathrm{MeV}$.

The photons lose energy in matter in a variety of processes. Contributions to the photon cross section in a light element (carbon) and a heavy element (lead) are shown in figure 7.2. In the image, the following notation is used: $\sigma_{\mathrm{p.e.}}$ stands for the (cross section for the) atomic photoelectric effect, $\sigma_{\mathrm{Rayleigh}}$ stands for the Rayleigh coherent scattering, $\sigma_{\mathrm{Compton}}$ for the Compton scattering off an electron, κ_{nuc} for the pair production in the nuclear field, κ_{nuc} for pair production in the electron field and $\sigma_{\mathrm{g.d.r.}}$ for photonuclear interactions.

At low energies it is seen that the photoelectric effect dominates, although Compton scattering, Rayleigh scattering, and photonuclear absorption also contribute. The photoelectric cross section is characterized by discontinuities (absorption edges) as thresholds for photoionization of various atomic levels are reached. One can see the increasing domination of the pair production mechanism as the energy of the photon increases.

Form these considerations one can see that when a high-energy electron or photon is incident on a thick absorber, it initiates an electromagnetic cascade as pair production and bremsstrahlung generate more electrons and photons with lower energy. The longitudinal shower development is governed by the high-energy part of the cascade, and hence it scales as the radiation length in the material. Eventually, the electron energies fall below the critical energy and then dissipate their energy by ionization and excitation. It is therefore convenient to introduce the scale variables $t = x/X_0$ and $y = E/E_c$. The mean longitudinal profile of the energy deposition in an electromagnetic cascade is well described by a gamma distribution:

$$\frac{\mathrm{d}E}{\mathrm{d}t} = E_0 b \frac{(bt)^{a-1} e^{-bt}}{\Gamma(a)}\,, \tag{7.3}$$

where a and b can be obtained for a specific detector by fitting on this function. The maximum t_{max} occurs on $(a-1)/b$, which is equal to $\ln y + C_{\mathrm{j}}$, with j standing for an electron or a photon. The factor C is equal to -0.5 for electron induced cascades and to 0.5 for photon induced cascades. The transverse development of electromagnetic showers in different materials scales fairly accurately with the Moliere radius R_M, given by $R_M \approx 21$ MeV X_0/E_c. On the average, only 10 % of the energy lies outside the cylinder with radius

R_M. About 99 % is contained inside of 3.5 R_M, but at this radius and beyond composition effects become important and the scaling with R_M fails. The distributions are characterized by a narrow core, and broaden as the shower develops, so they are often represented as the sum of two Gaussians.

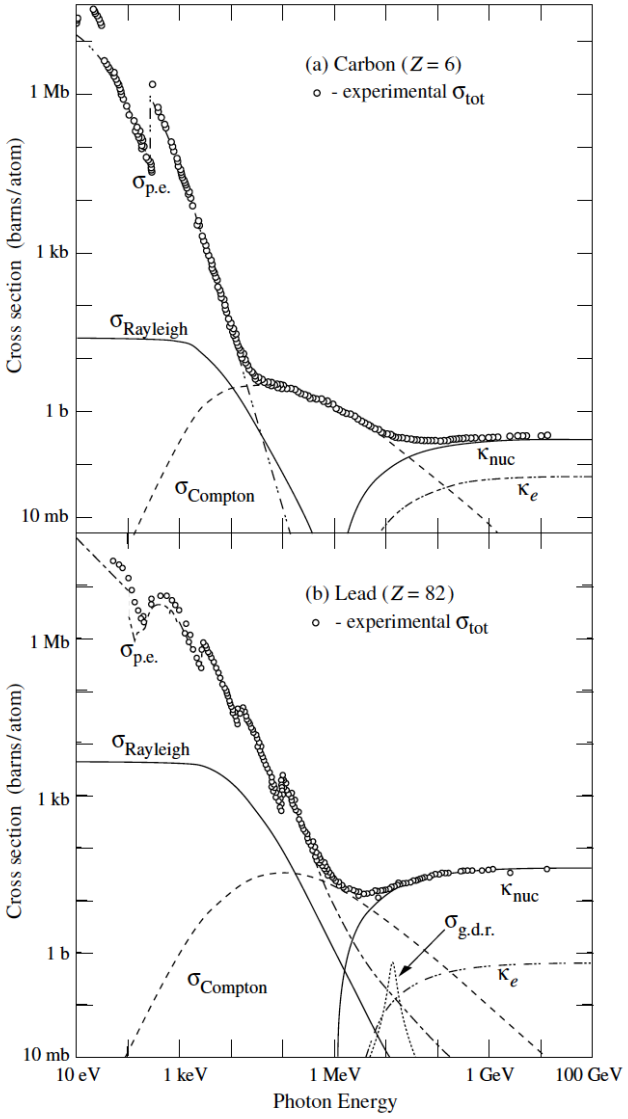

Figure 7.2: The contributions to the photon cross section in a light element (carbon) and a heavy element (lead). Figure taken from PDG review.

7.2. Neutral pion characteristics

$$I^G(J^{PC}) = 1^-(0^{-+})$$

The results printed here for the neutral pion are taken from C. Amsler et al. (Particle Data Group), PL B667, 1 (2008) (URL: http://pdg.lbl.gov). Some results that have been superseded by later experiments are omitted and may be found in Particle Data Group 1988 edition Physics Letters B204 1 (1988).

π^0 MASS

The value is calculated from $m_{\pi^\pm}$ and $(m_{\pi^\pm} - m_{\pi^0})$. The PDG fit gives

$$m_{\pi^0} = 134.9766 \pm 0.0006 \text{ MeV}\,.$$

To see recent revision of the charged pion mass see $\pi^\pm$ mass listings in C. Amsler et al. (Particle Data Group), PL B667, 1 (2008). The measurements of the difference of masses of charged and neutral pion are listed here. Measurements with an error > 0.01 MeV have been omitted.

Value (MeV)	Source
4.5936 ± 0.0005	PDG fit
4.5936 ± 0.0005	PDG average
4.59364 ± 0.00048	J.F.Crawford et al., PR D43 46
4.5930 ± 0.0013	J.F.Crawford et al., PRL 56 1043
4.59366 ± 0.00048	J.F.Crawford et al., PL B213 391
4.6034 ± 0.0052	I.M. Vasilevsky et al., PL 23 281
4.6056 ± 0.0055	J.B. Czirr, PR 130 341

π^0 MEAN LIFE

Measurements with an error $> 1 \cdot 10^{-17}$ s have been omitted. The PDG result error includes a scale factor of 3.0 and can be seen on the image below. The second and the fifth listed result measure π^0 decay widths Γ, and listed here are $\tau = \hbar/\Gamma$.

Value (10^{-17}s)	Source
8.4 ± 0.6	PDG average
$8.97 \pm 0.22 \pm 0.17$	H.W. Atherton et al., PL 158B 81
8.2 ± 0.4	A. Browman et al., PRL 33 1400
5.6 ± 0.6	G. Bellettini et al., NC 66A 243
9 ± 0.68	JV.I. Kryshkin, A.G. Sterligov, Y.P. Usov, JETP 30 1037
$8.4 \pm 0.5 \pm 0.5$	D.A. Williams et al., PR D38 1365

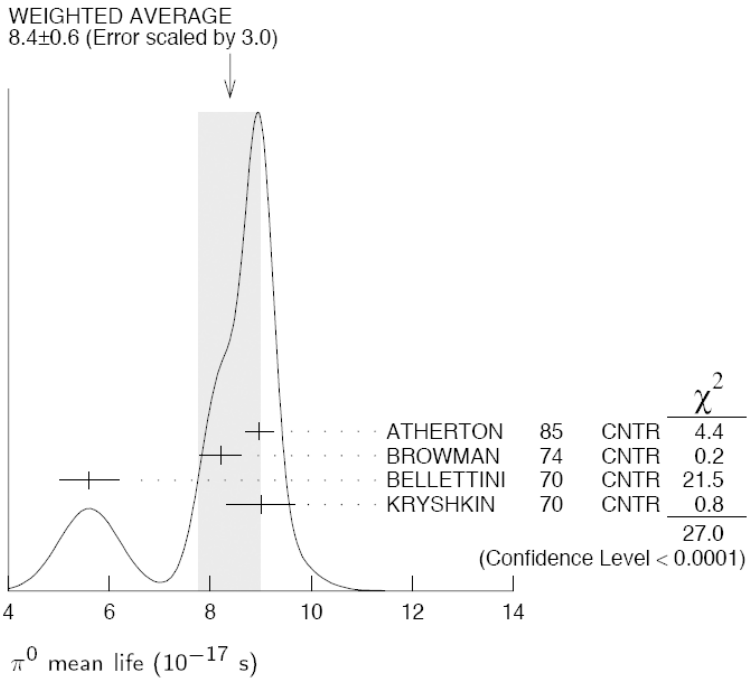

Figure 7.3: Particle Data Group result for the π^0 mean lifetime.

π^0 DECAY MODES

The results listed here for decay modes come from various sources. The references to these sources can be looked up in the Particle Listings of the PDG mentioned at the beginning of the section.

	Mode	Fraction (Γ_i/Γ)	Confidence level
Γ_1	2γ	0.98798 ± 0.00032	Sc.fac.=1.1
Γ_2	$e^+e^-\gamma$	0.01198 ± 0.00032	Sc.fac.=1.1
Γ_3	positronium + γ	$(1.82 \pm 0.29) \cdot 10^{-9}$	
Γ_4	$e^+e^+e^-e^-$	$(3.14 \pm 0.30) \cdot 10^{-5}$	
Γ_5	e^+e^-	$(6.46 \pm 0.33) \cdot 10^{-8}$	
Γ_6	4γ	$< 2 \cdot 10^{-8}$	0.9
Γ_7	$\nu\overline{\nu}$	$< 2.7 \cdot 10^{-7}$	0.9
Γ_8	$\nu_e\overline{\nu}_e$	$< 1.7 \cdot 10^{-6}$	0.9
Γ_9	$\nu_\mu\overline{\nu}_\mu$	$< 1.6 \cdot 10^{-6}$	0.9
Γ_{10}	$\nu_\tau\overline{\nu}_\tau$	$< 2.1 \cdot 10^{-6}$	0.9
Γ_{11}	$\gamma\nu\overline{\nu}$	$< 6 \cdot 10^{-4}$	0.9

Other modes listed in the PDG violate either charge conjugation symmetry or the lepton family number and are not listed here.

7.3. Kinematics of neutral pion decay

As seen earlier, the principal decay mode of a free neutral pion is $\pi^0 \to \gamma\gamma$. For a pion at rest, in order to conserve the 4-momentum, the gamma rays have to be emitted back to back, each with energy $m_{\pi^0}c^2/2$. In all the subsequent equations I will set c=1. So, in the rest frame, one can write:

$$\theta'_1 + \theta'_2 = \pi\,,$$

$$E'_1 = E'_2 = m_{\pi^0}/2\,. \tag{7.4}$$

Further on, since there is no preferred direction in space for the emission of gamma rays, they must be emitted isotropically, i.e.,

$$\frac{\mathrm{d}N}{\mathrm{d}\Omega} = \frac{1}{4\pi} \,. \tag{7.5}$$

To obtain the distributions of energy and angles of gamma rays emitted by a moving pion, one must make a Lorentz transformation from the pion rest frame to the frame where it is moving with velocity β. This gives:

$$E_1 + E_2 = \gamma m_{\pi^0} \,,$$

$$E_1 = \gamma \frac{m_{\pi^0}}{2} \left(1 + \beta \cos\theta_1'\right) \,,$$

$$E_1 \sin\theta_1 = \frac{m_{\pi^0}}{2} \sin\theta_1' \,,$$

$$E_1 \cos\theta_1 = \gamma \frac{m_{\pi^0}}{2} \left(\beta + \cos\theta_1'\right) \,, \tag{7.6}$$

where γ stands for $1/\sqrt{1-\beta^2}$.

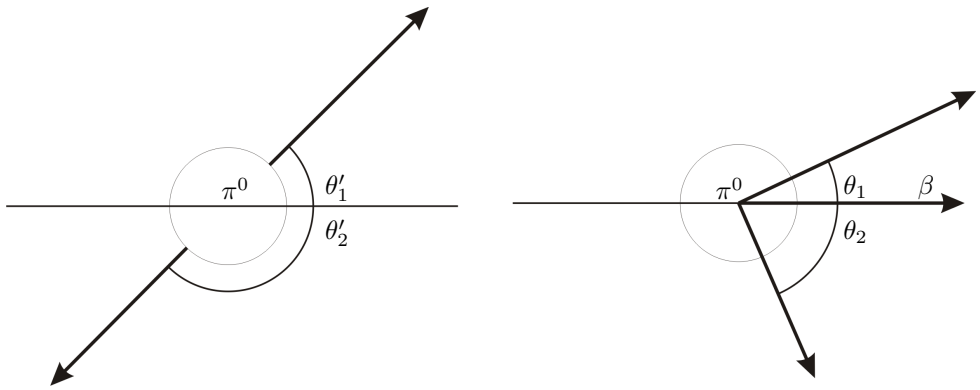

Figure 7.4: Schematic view of a decay of a neutral pion. The left image show the decay in the rest frame of the pion, the right image in the laboratory frame.

One finds that the energy of a photon is related to its angle of emission by the expression

$$E_1 = \frac{m_{\pi^0}}{2\gamma(1-\beta\cos\theta_1)}\,. \tag{7.7}$$

This distribution is shown on a MeV scale on figure 7.5 for various π^0 kinetic energies.

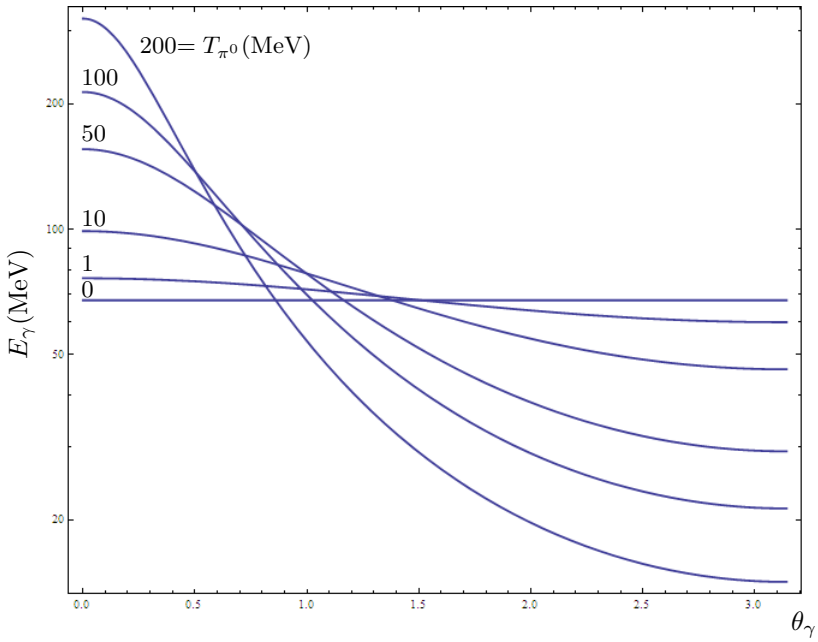

Figure 7.5: Variation of E_γ with θ_γ for various energy π^0 decaying in flight.

In a similar manner, one finds that the angles of emission of photons are related by the expression

$$\cos\theta_2 = \frac{1}{\beta}\left(1 - \frac{1-\beta\cos\theta_1}{2\gamma^2(1-\beta\cos\theta_1)-1}\right)\,. \tag{7.8}$$

The energy distribution of photons emitted by a moving pion is given by:

$$\frac{\mathrm{d}N}{\mathrm{d}E_1} = \frac{\mathrm{d}N}{\mathrm{d}\cos\theta_1'}\frac{\mathrm{d}\cos\theta_1'}{\mathrm{d}E_1} = \frac{1}{\gamma\beta m_{\pi^0}}\,, \tag{7.9}$$

in the limits $(E_{\min}, E_{\max})$ and 0 elsewhere, where

$$E_{\min} = \gamma\frac{m_{\pi^0}}{2}(1-\beta)\,,$$

$$E_{\max} = \gamma \frac{m_{\pi^0}}{2}(1+\beta)\,. \tag{7.10}$$

So, the distribution is flat and broadens with increasing pion energy. This distribution, as well as the energy limits where it is different from zero, are shown on figures 7.6 and 7.7.

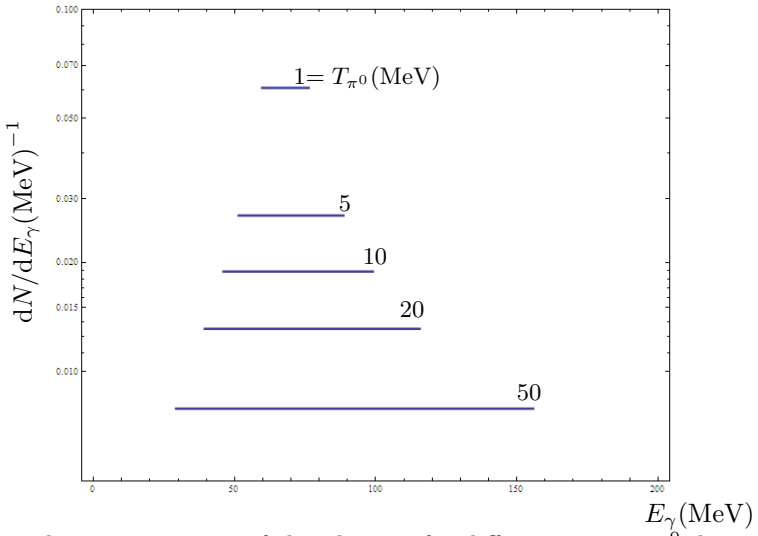

Figure 7.6: Distribution in energy of the photons for different energy π^0 decaying in flight.

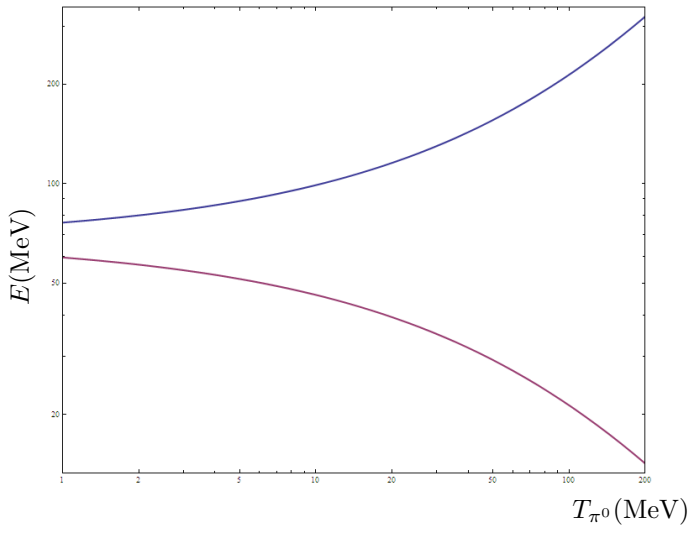

Figure 7.7: Upper and lower energy limits where the distribution of energy of the photons from π^0 decaying in flight is different from zero.

Next, the angular distribution of the emitted photon is given by:

$$\frac{\mathrm{d}N}{\mathrm{d}\Omega_1} = \frac{1}{2\pi}\frac{\mathrm{d}N}{\mathrm{d}E_1}\frac{\mathrm{d}E_1}{\mathrm{d}\cos\theta_1} = \frac{1}{4\pi}\frac{1}{\gamma^2\left(1-\beta\cos\theta_1\right)^2}\,. \tag{7.11}$$

One can see that as the energy of the pion increases, the photon tends to be emitted in a more forward direction. This is shown in figure 7.8.

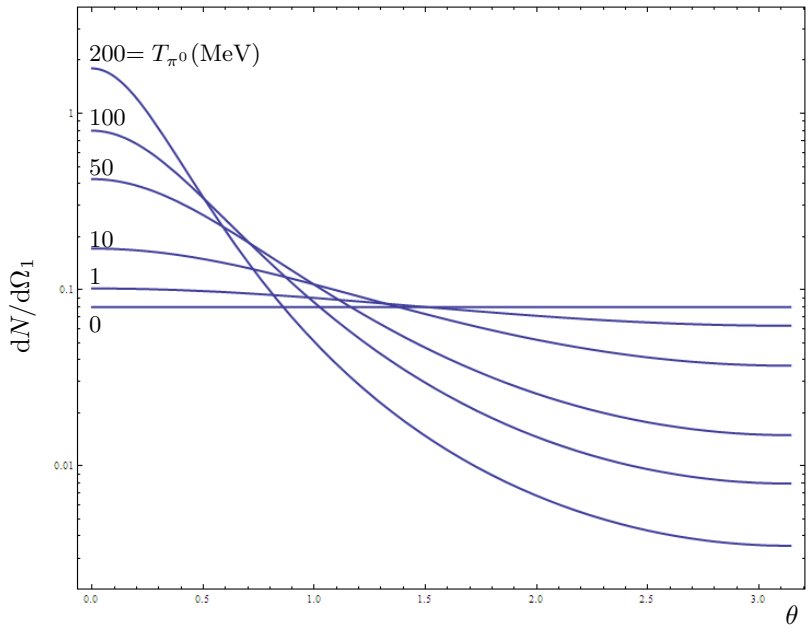

Figure 7.8: The angular distribution of photons for different energy π^0 decaying in flight.

Another quantity that is important in investigating pion production by observing photons is the opening angle between two photons, $\phi = \theta_1 + \theta_2$. If the variation of the opening angle is examined against the emission angle of one photon, one finds that there is a minimum opening angle associated with a pion of a given energy. This angle is given by

$$\phi_{\mathrm{min}} = 2\arcsin\left(\frac{1}{\gamma}\right)\,. \tag{7.12}$$

The distribution of ϕ vs. the outgoing angle of one photon, θ_1, as well as the dependence of the minimal opening angle between the two photons as a function of the energy of the pion

are shown on figures 7.9 and 7.10.

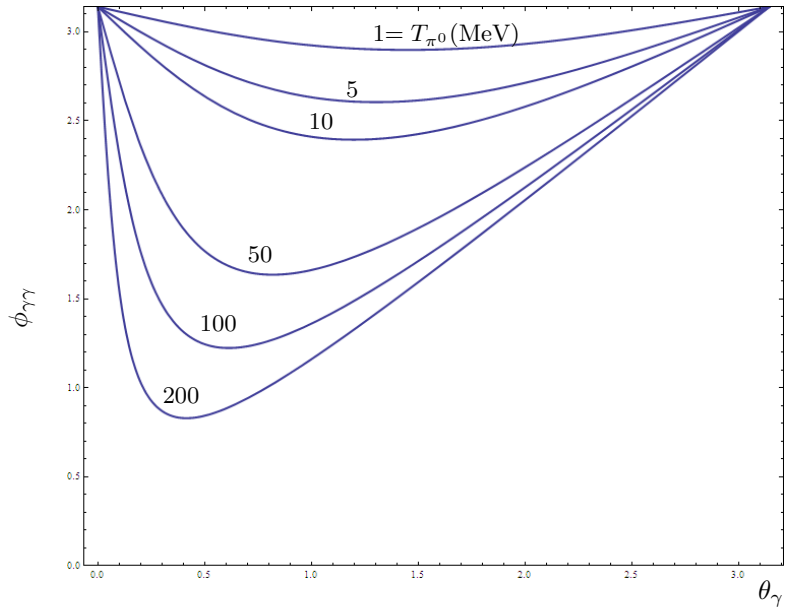

Figure 7.9: The dependence of the opening angle between the two photons as a function of an outgoing angle of one of the photons.

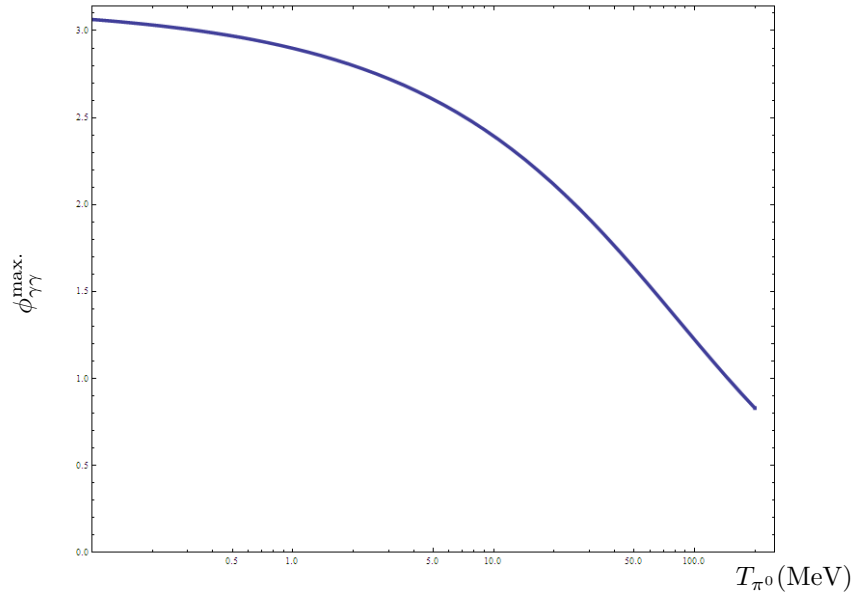

Figure 7.10: The dependence of the minimal opening angle between the outgoing photons as a function of the pion energy.

Also, one can calculate the distribution in opening angle with the result

$$\frac{\mathrm{d}N}{\mathrm{d}\phi} = \frac{1-\beta^2}{2\beta}\frac{\cos(\phi/2)}{\sin^2(\phi/2)}\frac{1}{\sqrt{\beta^2-\cos^2(\phi/2)}}\,, \tag{7.13}$$

for $\phi > \arcsin(1/\gamma)$ and 0 elsewhere.

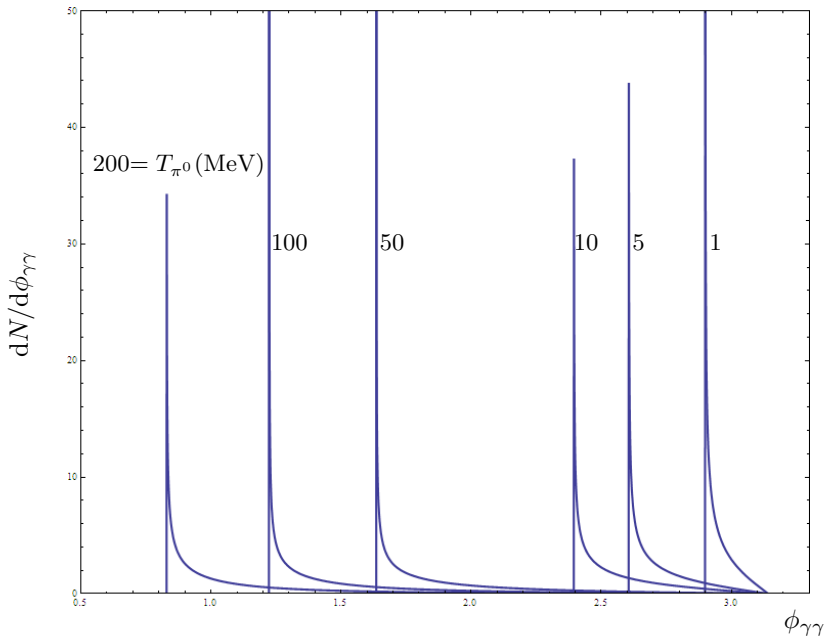

Figure 7.11: Distribution in the opening angle of the photons for different energy π^0 decaying in flight.

From the distribution in the opening angle, one can observe that there is a focusing effect that increases with increasing pion energy. That is, as the pion energy increases, it becomes more and more probable for the photons to be emitted with the minimum opening angle. This configuration is associated with the state where in which the two photons are emitted symmetrically at angles $\phi_{\min}/2$ relative to the direction of the motion of the pion. This focusing effect is of great importance in experiments looking for pions by photon reconstructions.

Another quantity of great importance is the laboratory angle θ between the direction of a photon from π^0 decay and the direction of the π^0. One can get the general connection between the two quantities by writing the relation between the energies of the photon in the

rest frame of the pion and the lab frame, $E' = \gamma E(1 - \beta \cos\theta)$ and squaring it. After some manipulation, this becomes

$$E_{\pi^0}(E_\gamma, \theta) = \frac{m_{\pi^0}\left(E_\gamma^2 \cos^2\theta + \left(\frac{m_{\pi^0}}{2}\right)^2\right)}{E_\gamma\left(\frac{m_{\pi^0}}{2} \pm \cos\theta\sqrt{\left(\frac{m_{\pi^0}}{2}\right)^2 - E_\gamma^2 \sin^2\theta}\right)} \tag{7.14}$$

One can see that for a given angle θ there are in general two values of E_{π^0}. Figure 7.12 shows this dependence for different photon energies.

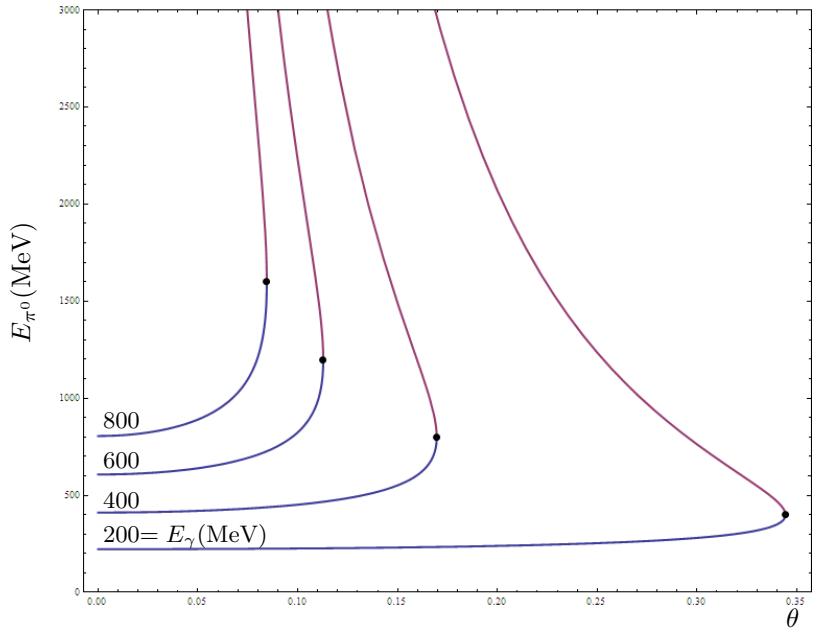

Figure 7.12: The dependence of the energy of the pion on the outgoing angle of the photon. Shown here are distributions for varying photon energies. The lower branch of the curves corresponds to the + sign in the equation governing the distribution, and the upper to the − sign. The solid points indicate where the lines meet and where the angle is maximal.

At the point where the curves meet, the angle reaches it's maximum value. Here I shall show what the value of this upper limit is. To find it, one can look at the transverse momentum of a decay photon with respect to the direction of the π^0:

$$P_\perp = P_\gamma \sin\theta = E_\gamma \sin\theta\,. \tag{7.15}$$

This quantity is invariant with respect to the boost of the π^0 rest frame, so

$$P_\perp = P_\perp^* = P_\gamma^* \sin\theta^* = \frac{m_{\pi^0}}{2} \sin\theta^* \,. \tag{7.16}$$

Comparing the two equations gives

$$\sin\theta = \frac{m_{\pi^0}}{2E_\gamma} \sin\theta^* \,. \tag{7.17}$$

As long as $\theta \leq \pi/2$, it is true that

$$\sin\theta_{\text{max.}} = \frac{m_{\pi^0}}{2E_\gamma} \,. \tag{7.18}$$

However, there are cases when $\theta > \pi/2$, for which $P_{||} < 0$. Recalling the boost formalism, one can show that in such case the minimal value for $P_{||}$ is achieved when $\cos\theta^* = -\beta_{\pi^0}$. In that case it turns out that $E_\gamma < m_{\pi^0}/2$. Thus, the result obtained earlier only holds for the opposite case, $E_\gamma > m_{\pi^0}/2$. One can go further and look at the case when $E_\gamma >> m_{\pi^0}$, as is often the case in high energy experiments. Then the maximal angle condition transforms to

$$\theta_{\text{max.}} \approx \frac{m_{\pi^0}}{2E_\gamma} \,. \tag{7.19}$$

The proper distribution of the maximum angle, as well as it's approximation, can be seen on the figure 7.13.

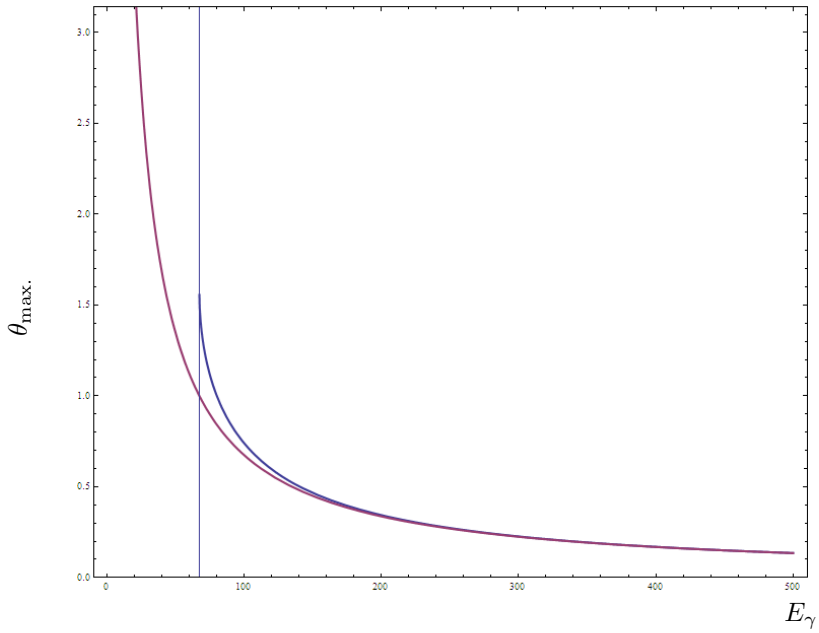

Figure 7.13: The maximum angle between the pion and it's outgoing photon as a function of energy of the photon. The upper line is the proper distribution and the lower it's approximation. The vertical line denotes the limit of $E_\gamma = m_{\pi^0}/2$. At the energy of 128 MeV the proper distribution differs by 5 percent from the approximation, while at 278 MeV the difference becomes 1 percent.

Finally, one can generalize all that has been calculated and suppose that π^0s are produced in some scattering process with distribution $N_{\pi^0}(E_{\pi^0}, \theta_{\pi^0})$, where the angle is measured with respect to the beam direction. A detector is placed at angle θ to the beam and records the energy spectrum $N_\gamma(E_\gamma, \theta)$ of the photons that strike it. Since the maximum angle between the photon and its parent pion is negligibly small, the probability that a photon hits a detector at a given angle is approximately the same as the probability that its parent pion would have hit the detector. Then, according to previous results, the distribution of the energy of photons is the same as that for pions. So, the number of photons $N_\gamma(E_\gamma)$ that appear in an energy interval $\mathrm{d}E_\gamma$ is

$$N_\gamma = \frac{2}{\gamma\beta m_{\pi^0}} \approx \frac{2}{E_{\pi^0}}\,, \tag{7.20}$$

where the factor 2 arises because of the fact that there are two photons. So, if the pions

are produced with an energy spectrum $N_{\pi^0}(E_{\pi^0}, \theta_{\pi^0})$ then the energy spectrum of the decay photons in the detector centered on θ_{π^0} is

$$N_\gamma(E_\gamma, \theta_\gamma = \theta_{\pi^0}) = \int_{E_\gamma}^{\infty} \frac{2}{E_{\pi^0}} N_{\pi^0}(E_{\pi^0}, \theta_{\pi^0}) \mathrm{d}E_{\pi^0} \,. \tag{7.21}$$

Taking the derivative, one finds

$$N_\pi(E_\pi, \theta_\pi) = -\frac{E_\pi}{2} \frac{\mathrm{d}N_\gamma(E_\gamma = E_\pi, \theta_\gamma = \theta_\pi)}{\mathrm{d}E_\gamma} \,. \tag{7.22}$$

So, if one knows the distribution of energies of the photons, it can be directly connected to the distribution of the pions.

7.4. Operational definition of the Collins angle

1. Find the coordinates of the multiphoton intercept point and the pion intercept point in the STAR coordinates. Image given here is the STAR coordinate system along with the STAR angle ϕ definition from the function atan2(yy,xx). Left is South (S), right is North (N).

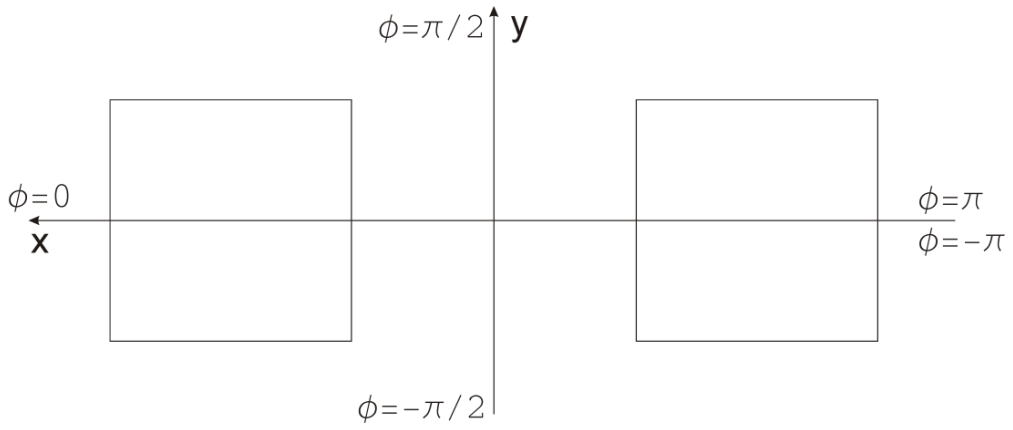

Figure 7.14: View of the detector faces in the STAR coordinate system

2. Put all the x coordinates in absolute values; this will insure mirror symmetry. Leave the STAR angle as it is.

3. From the found coordinates, form vectors from the beamline to the MP intercept point (p), and from the intercept point to the pion point (d). The vectors connecting the beam line and the pion (MP) are the STAR angles ϕ_π and ϕ_{MP}.

   The angle between p and d is the Collins angle, designated here by γ. The next illustration shows the calculated Collins angle if the MP intercept point is in the center of a detector. The angle is found with acos(y,x), so it only takes on values from 0 to π.

4. Finally, a further set of conditions is placed on the Collins angle, to define which are negative, which not:

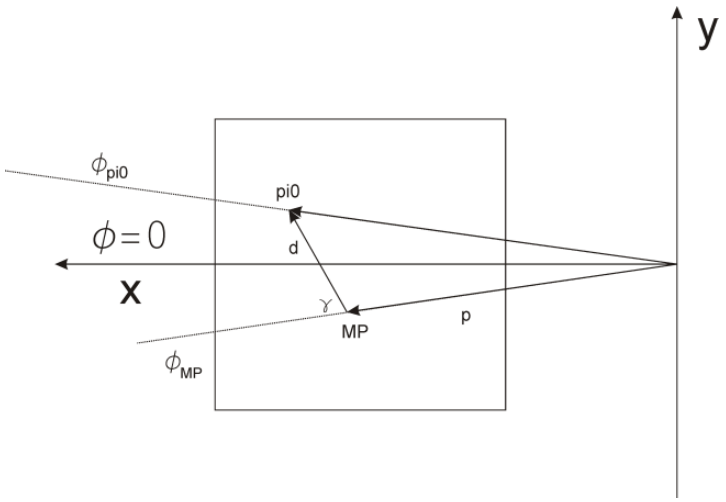

Figure 7.15: Definition of the vectors in the Collins angle definition.

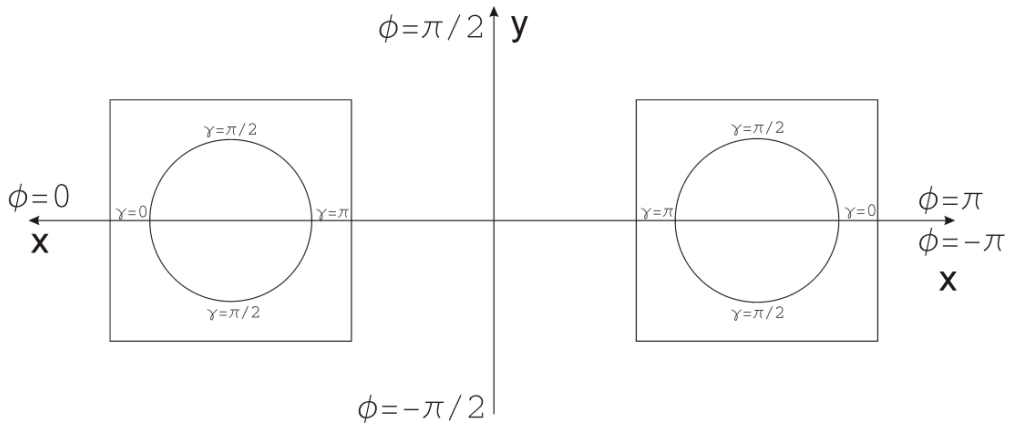

Figure 7.16: The calculation of the Collins angle with acos(y,x).

(a) In the S detector there is a single case since the STAR angle is continuous: If $\phi_\pi < \phi_{MP}$, the Collins angle is declared negative. This corresponds to all the pions that are below the "beam pipe - MP intercept" line.

(b) In the N detector there are more cases due to discontinuity of the ϕ at $\pm\pi$:

- If $\phi_{MP} > 0$, as in the image, then the negative Collins angles will be all $\phi_\pi > \phi_{MP}$ (up to π), as well as all $\phi_\pi < 0$.

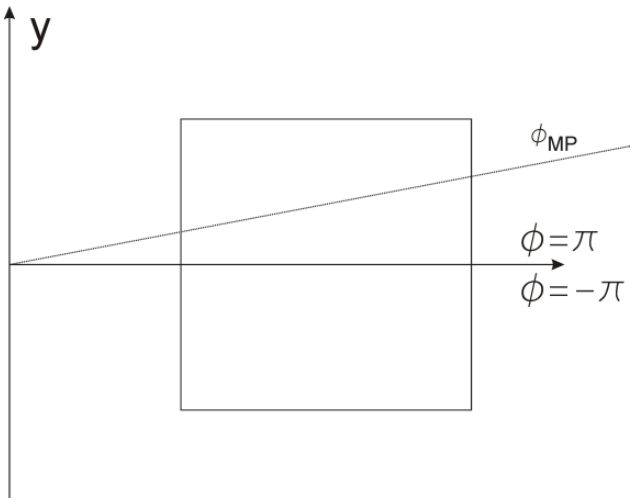

Figure 7.17: The WN detector scheme for evaluating the sign of the Collins angle.

- If $\phi_{MP} < 0$ then the negative Collins angles will be all $\phi_\pi > \phi_{MP}$, but with the condition that $\phi_\pi < 0$ (less negative STAR angles)

5. This way the bins are mirror symmetrical, with $\gamma = 0$ being further from the beam and $\gamma < 0$ being the angles below the "beam pipe - MP intercept" line.

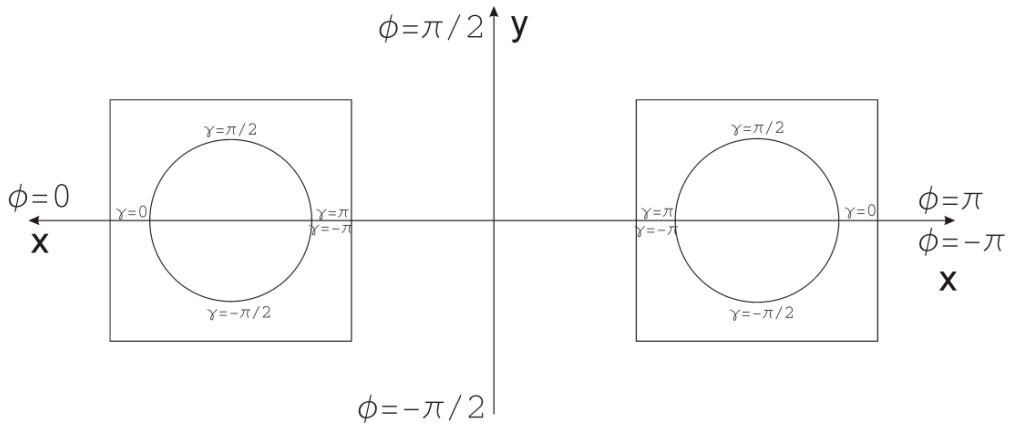

Figure 7.18: The final result for the Collins angle calculation if the MP intercept point is in the center of the detectors.

7.5. Calculated asymmetries

Published Run 6 results

$< x_F >$	A_N	statistical error	$< x_F >$	A_N	statistical error
0.20	0.00087	0.00130	-0.2	-0.00039	0.00127
0.23	0.00213	0.00157	-0.23	0.00032	0.00153
0.27	0.01021	0.00174	-0.27	0.00229	0.00170
0.32	0.02726	0.00315	-0.32	-0.00454	0.00307
0.37	0.03917	0.00579	-0.37	0.00390	0.00566
0.43	0.05333	0.01015	-0.43	-0.01457	0.00990
0.50	0.05989	0.02630	-0.5	0.01008	0.02574

Table 7.1: Published Run 6 results for the West detectors

$< x_F >$	A_N	statistical error	$< x_F >$	A_N	statistical error
0.24	0.00571	0.00579	-0.24	-0.00442	0.00538
0.28	0.00192	0.00122	-0.28	-0.00030	0.00123
0.32	0.00909	0.00093	-0.27	-0.00098	0.00095
0.37	0.02343	0.00144	-0.32	0.00150	0.00147
0.43	0.03859	0.00228	-0.37	0.00131	0.00233
0.50	0.06916	0.00478	-0.50	-0.00547	0.00489
0.60	0.10345	0.01369	-0.60	-0.00381	0.01405

Table 7.2: Published Run 6 results for the East detectors

Results obtained with the "large cell live readout" condition

$< x_F >$	A_N	statistical error	$< x_F >$	A_N	statistical error
0.20	-0.00069	0.00225	-0.20	0.00099	0.00219
0.23	0.00178	0.00253	-0.23	-0.00085	0.00246
0.27	0.01062	0.00249	-0.27	-0.00174	0.00242
0.32	0.02410	0.00403	-0.32	-0.00346	0.00390
0.37	0.04292	0.00705	-0.37	-0.00764	0.00685
0.43	0.05315	0.01208	-0.43	-0.01685	0.01172
0.50	0.07953	0.03132	-0.50	-0.02079	0.03029

Table 7.3: Results for the West detectors with the "large cell live readout" condition

$< x_F >$	A_N	statistical error	$< x_F >$	A_N	statistical error
0.28	-0.00176	0.00185	-0.28	0.00203	0.00188
0.32	0.00921	0.00106	-0.27	-0.00099	0.00108
0.37	0.02112	0.00156	-0.32	0.00187	0.00159
0.43	0.03663	0.00244	-0.37	0.00061	0.00249
0.50	0.07121	0.00511	-0.50	-0.00336	0.00522
0.60	0.09546	0.01440	-0.60	-0.01528	0.01473

Table 7.4: Results for the East detectors with the "large cell live readout" condition

7.6. The STAR collaboration

M. M. Aggarwal, A. K. Bhati, and N. K. Pruthi
Panjab University, Chandigarh 160014, India

Z. Ahammed, X. Dong, O. Grebenyuk, E. Hjort, P. Jacobs, D. P. Kikola, J. Kiryluk, S. R. Klein, H. Masui, H. S. Matis, M. Naglis, G. Odyniec, D. Olson, M. A. Ploskon, A. M. Poskanzer, C. B. Powell, H. G. Ritter, A. Rose, S. Sakai, I. Sakrejda, A. M. Schmah, E. P. Sichtermann, X. M. Sun, T. J. M. Symons, J. H. Thomas, V. N. Tram, H. Wieman, N. Xu, and Y. Zhang
Lawrence Berkeley National Laboratory, Berkeley, California 94720, USA

A. V. Alakhverdyants, G. S. Averichev, I. Bunzarov, T. G. Dedovich, L. G. Efimov, J. Fedorisin, A. Kechechyan, V. Kizka, R. Lednicky, Y. Panebratsev, O. V. Rogachevskiy, E. Shahaliev, M. Tokarev, S. Vokal, R. Zoulkarneev, and Y. Zoulkarneeva
Joint Institute for Nuclear Research, Dubna, 141 980, Russia

I. Alekseev , L. Koroleva, B. Morozov, and D. N. Svirida
Alikhanov Institute for Theoretical and Experimental Physics, Moscow, Russia

J. Alford, B. D. Anderson, J. Bouchet, J. Joseph, D. Keane, L. Kumar, S. Margetis, Y. Pandit, N. L. Subba, J. A. Vanfossen, Jr., and W. M. Zhang
Kent State University, Kent, Ohio 44242, USA

C. D. Anson, Z. Chajecki, T. J. Humanic, and M. A. Lisa
Ohio State University, Columbus, Ohio 43210, USA

D. Arkhipkin, D. R. Beavis, L. C. Bland, T. P. Burton, W. Christie, R. R. Debbe, L. Didenko, J. C. Dunlop, V. Fine, Y. Fisyak, A. Gordon, W. Guryn, M. A. C. Lamont, J. M. Landgraf, J. Lauret, A. Lebedev, J. H. Lee, M. J. LeVine, T. Ljubicic, R. S. Longacre, W. A. Love, A. Ogawa, P. Pile, L. Ruan, P. Sorensen, A. H. Tang, T. Ullrich, G. Van Buren, F. Videbæk, J. C. Webb, Z. Xu, and K. Yip
Brookhaven National Laboratory, Upton, New York 11973, USA

J. Balewski, M. J. Betancourt, R. Corliss, J. P. Hays-Wehle, W. Leight, R. Milner, R. Redwine, T. Sakuma, J. Seele, S. G. Steadman, B. Surrow, G. van Nieuwenhuizen, and M. Walker
Massachusetts Institute of Technology, Cambridge, MA 02139-4307, USA

R. Bellwied, L. C. De Silva, M. Elnimr, S. LaPointe, C. Pruneau, M. Sharma, L. H. Tarini, A. R. Timmins, and S. A. Voloshin
Wayne State University, Detroit, Michigan 48201, USA

R. R. Betts, O. Evdokimov, D. J. Hofman, K. Kauder, H. Pei, and M. C. Suarez
University of Illinois at Chicago, Chicago, Illinois 60607, USA

A. Bhasin, S. M. Dogra, A. Gupta, L. K. Mangotra, and B. V. K. S. Potukuchi
University of Jammu, Jammu 180001, India

H. Bichsel, J. G. Cramer, D. Kettler, D. Prindle, and T. A. Trainor
University of Washington, Seattle, Washington 98195, USA

J. Bielcik, O. Hajkova, M. Krus, and M. Pachr
Czech Technical University in Prague, FNSPE, Prague, 115 19, Czech Republic

J. Bielcikova, P. Chaloupka, P. Chung, J. Kapitan, V. Kouchpil, J. Rusnak, M. Sumbera, and D. Tlusty
Nuclear Physics Institute AS CR, 250 68 Řež/Prague, Czech Republic

B. Biritz, R. Cendejas, D. R. Gangadharan, S. M. Guertin, H. Z. Huang, G. Igo,
P. Kurnadi, D. Staszak, S. Trentalange, O. D. Tsai, G. Wang, C. Whitten Jr., and W. Xu
University of California, Los Angeles, California 90095, USA

W. Borowski, M. Estienne, A. Geromitsos, and S. Kabana
SUBATECH, Nantes, France

E. Braidot, A. Mischke, and T. Peitzmann
NIKHEF and Utrecht University, Amsterdam, The Netherlands

A. V. Brandin, L. Kotchenda, P. Kravtsov, E. V. Lukashov, V. Okorokov, and M. Strikhanov
Moscow Engineering Physics Institute, Moscow Russia

A. Bridgeman, K. Krueger, H. M. Spinka, and D. G. Underwood
Argonne National Laboratory, Argonne, Illinois 60439, USA

S. G. Brovko, M. Calderón de la Barca Sánchez, D. Cebra, J. E. Draper,
B. Haag, H. Liu, O. I. Mall, R. Reed, J. L. Romero, S. Salur, and E. Sangaline
University of California, Davis, California 95616, USA

E. Bruna, H. Caines, A. Chikanian, E. Finch, J. W. Harris, M. Heinz,
A. G. Knospe, R. Majka, Ohlson, J. Putschke, J. Sandweiss, and N. Smirnov
Yale University, New Haven, Connecticut 06520, USA

S. Bueltmann, I. Koralt, and D. Plyku
Old Dominion University, Norfolk, VA, 23529, USA

X. Z. Cai, J. H. Chen, L-X. Han, F. Jin, W. Li, G. L. Ma, Y. G. Ma,
J. Tian, L. Xue, S. Zhang, J. Zhao, C. Zhong, and Y. H. Zhu
Shanghai Institute of Applied Physics, Shanghai 201800, China

M. C. Cervantes, M. J. M. Codrington, P. Djawotho, J. L. Drachenberg,
C. A. Gagliardi, A. Hamed, L. Huo, S. Mioduszewski, and R. E. Tribble
Texas A&M University, College Station, Texas 77843, USA

S. Chattopadhyay, M. R. Dutta Mazumdar, P. Ghosh, B. Mohanty, M. M. Mondal,
T. K. Nayak, S. K. Pal, R. N. Singaraju, Tribedy, and Y. P. Viyogi
Variable Energy Cyclotron Centre, Kolkata 700064, India

H. F. Chen, B. Huang, C. Li, Y. Lu, X. Luo, M. Shao, Y. Sun, Z. Tang, X. L. Wang, Y. Xu, and Z. P. Zhang
University of Science & Technology of China, Hefei 230026, China

J. Y. Chen, N. Li, Z. M. Li, F. Liu, S. S. Shi, Y. F. Wu, and J. B. Zhang
Institute of Particle Physics, CCNU (HZNU), Wuhan 430079, China

J. Cheng, K. Kang, Y. Li, Y. Wang, Q. Yue, X. P. Zhang, and X. Zhu
Tsinghua University, Beijing 100084, China

M. Cherney, Y. N. Gorbunov, T. S. McShane, and J. Seger
Creighton University, Omaha, Nebraska 68178, USA

K. E. Choi, Oh, and I-K. Yoo
Pusan National University, Pusan, Republic of Korea

H. J. Crawford, J. Engelage, E. G. Judd, M. J. Ng, and C. Perkins

University of California, Berkeley, California 94720, USA

S. Dash, C. Jena, D. P. Mahapatra, and S. C. Phatak
Institute of Physics, Bhubaneswar 751005, India

A. Davila Leyva, G. W. Hoffmann, L. Li, C. Markert, E. W. Oldag, R. L. Ray, J. Schambach, D. Thein, and M. Wada
University of Texas, Austin, Texas 78712, USA

A. A. Derevschikov, Yu. A. Matulenko, A. Meschanin, N. G. Minaev,
D. A. Morozov, L. V. Nogach, S. B. Nurushev, and A. N. Vasiliev
Institute of High Energy Physics, Protvino, Russia

R. Derradi de Souza, J. Takahashi, and G. M. S. Vasconcelos
Universidade Estadual de Campinas, Sao Paulo, Brazil

G. Eppley, F. Geurts, J. Liu, W. J. Llope, D. McDonald, J. B. Roberts, and P. Yepes
Rice University, Houston, Texas 77251, USA

L. Eun and S. Heppelmann
Pennsylvania State University, University Park, Pennsylvania 16802, USA

R. Fatemi, R. G. Fersch, W. Korsch, G. Webb, and W. Witzke
University of Kentucky, Lexington, Kentucky, 40506-0055, USA

D. Grosnick, D. D. Koetke, R. Manweiler, and T. D. S. Stanislaus
Valparaiso University, Valparaiso, Indiana 46383, USA

A. Hirsch, J. Konzer, X. Li, P. K. Netrakanti, R. P. Scharenberg,
M. J. Skoby, B. Srivastava, B. Stringfellow, F. Wang, Q. Wang, and W. Xie
Purdue University, West Lafayette, Indiana 47907, USA

W. W. Jacobs, B. S. Page, I. Selyuzhenkov, J. R. Stevens, and S. W. Wissink
Indiana University, Bloomington, Indiana 47408, USA

A. Kisiel, T. Pawlak, W. Peryt, J. Pluta, M. Zawisza, and H. Zbroszczyk
Warsaw University of Technology, Warsaw, Poland

T. Kollegger, M. K. Mitrovski, T. R. Schuster, and R. Stock
University of Frankfurt, Frankfurt, Germany

X. Li, Q. H. Xu, and W. Zhou
Shandong University, Jinan, Shandong 250100, China

M. G. Munhoz, A. A. P. Suaide, and A. Szanto de Toledo
Universidade de Sao Paulo, Sao Paulo, Brazil

B. K. Nandi, P. R. Pujahari, and R. Varma
Indian Institute of Technology, Mumbai, India

M. Planinic and N. Poljak
University of Zagreb, Zagreb, HR-10002, Croatia

H. Qiu, Z. Sun, J. S. Wang, H. Xu, Y. Yang, and W. Zhan
Institute of Modern Physics, Lanzhou, China

R. Raniwala and S. Raniwala
University of Rajasthan, Jaipur 302004, India

N. Schmitz, P. Seyboth, and F. Simon
Max-Planck-Institut für Physik, Munich, Germany

T. Tarnowsky, H. Wang, and G. D. Westfall
Michigan State University, East Lansing, Michigan 48824, USA

R. Witt
United States Naval Academy, Annapolis, MD 21402, USA

Bibliography

[1] E. Hughes and R. Voss. Spin dependent quark forces and the spin content of the nucleon. *Annual review of nuclear and particle science*, 49:303, 1999. 1, 145

[2] B. Adeva et al. Spin asymmetries a_1 and structure functions g_1 of the proton and the deutron from polarized high energy muon scattering. *Physical review D*, 58:112001, 1998. 1, 145

[3] B. Adeva et al. Next-to-leading order qcd analysis of the spin structure function g_1. *Physical review D*, 58:112002, 1998. 1, 145

[4] D. Adams et al. Analyzing power in inclusive π^+ and π^- production at high x_f with a 200 gev polarized proton beam. *Physics letters B*, 261:462, 1991. 1, 2, 145

[5] I. Alexeev et al. Polarized proton collider at rhic. *Nuclear instruments and methods A*, 499:392–414, 2003. 3, 25

[6] A. Sokolov and L. Ternov. On polarization and spin effects in synchrotron radiation theory. *Soviet physics doklady*, 8:1203, 1964. 3

[7] J. Adams et al. Forward neutral pion production in p+p and d+au collisions at $\sqrt{s}$ = 200gev. *Physical review letters*, 97:152302, 2006. 3

[8] B.I.Abelev et al. Forward neutral pion transverse single spin asymmetries in p+p collisions at $\sqrt{s}$=200 gev. *Physical review letters*, 101:222001, 2008. 3, 55, 86, 102, 106, 107, 131, 132, 145, 146

[9] D. Sivers. Single-spin production asymmetries from the hard scattering of pointlike constituents. *Physical review D*, 41:83, 1990. 3, 19

[10] D. Sivers. Hard scattering scaling laws for single-spin production asymmetries. *Physical review D*, 43:261, 1991. 3

[11] J. Collins. Fragmentation of transversely polarized quarks probed in transverse momentum distributions. *Nuclear Physics B*, 396:161, 1993. 3, 21

[12] V. Barone, A. Drago, and P. G. Ratcliffe. Transverse polarisation of quarks in hadrons. *Physics reports*, 359:1, 2002. 5

[13] S. Weinberg. *Quantum theory of fields vol.1.* Cambridge University press, 1995. 8

[14] J. Collins and D. Soper. Parton distribution and decay functions. *Nuclear physics B*, 194:445, 1982. 10

[15] D.J. Gross and S.B. Treiman. Light-cone structure of current commutators in the gluon-quark model. *Physical review D*, 4:1059–1072, 1971. 13

[16] J.C.Collins, D.E.Soper, and G. Sterman. Transverse momentum distribution in drell-yan pair and w and z boson production. *Nuclear physics B*, 250:199–224, 1985. 16

[17] D. de Florian. Next-to-leading order qcd corrections to one-hadron production in polarized pp collisions at rhic. *Physical review D*, 67:054004, 2003. 17

[18] B. Jaeger et al. Next-to-leading order qcd corrections to high-p_t pion production in longitudinally polarized pp collisions. *Physical review D*, 67:054005, 2003. 17

[19] S. Kretzer. Fragmentation of partons. *Acta physica polonica B*, 36:179–186, 2005. 17

[20] U. DAlesio and F. Murgia. Parton intrinsic motion in inclusive particle production: unpolarized cross sections, single spin asymmetries, and the sivers effect. *Physical review D*, 70:074009, 2004. 19, 108

[21] J. Qiu and G. Sterman. Single transverse spin asymmetries. *Physics review letters*, 67:2264, 1991. 19, 23, 108

[22] J. Qiu and G. Sterman. Single transverse spin asymmetries in direct photon production. *Nuclear physics B*, 378:52, 1992. 19, 23, 108

[23] J. Qiu and G. Sterman. Single transverse-spin asymmetries in hadronic pion production. *Physical review D*, 59:014004, 1999. 19, 23

[24] Y. Kanazawa and Y. Kioke. Chiral-odd contribution to single-transverse spin asymmetry in hadronic pion production. *Physics letters B*, 478:121, 2000. 19, 23

[25] Y. Kanazawa and Y. Kioke. Estimate of a chiral-odd contribution to single transverse-spin asymmetry in hadronic pion production. *Physics letters B*, 490:99, 2000. 19, 23

[26] M. Anselmino, M. Boglione, and F. Murgia. Single spin asymmetry for pp to πx in perturbative qcd. *Physics letters B*, 362:164, 1995. 20

[27] M. Anselmino and F. Murgia. Single spin asymmetries in pp and $\overline{\text{p}}$p inclusive processes. *Physics letters B*, 442:470, 1998. 20

[28] M. Anselmino, M. Boglione, and F. Murgia. Phenomenology of single spin asymmetries in pp to πx. *Physical review D*, 60:054027, 1999. 20

[29] X. Ji et al. A unified picture for single transverse-spin asymmetries in hard processes. *Physical review letters*, 97:082002, 2006. 23

[30] N. Makins. Transverse spin and momentum: Experimental overview. In *SPIN08 conference, Virginia, USA*, http://faculty.virginia.edu/spin2008/, 2008. 23

[31] W. MacKay et al. Commissioning and future plans for polarized protons in rhic. *Particle accelerator conference proceedings, BNL-67938*, 2001. 26

[32] T. Roser et al. First polarized proton collisions at rhic. In *Workshop on Increasing the AGS Polarization, U. of Michigan*, 2002. 27

[33] H. Huang et al. Polarized proton acceleration at the brookhaven ags and rhic. *Particle Accelerator Conference proceedings, Portland, Oregon*, 2003. 27

[34] M. Bai et al. Rhic polarized proton new working point commissioning. In *16th International Spin Physics Symposium proceedings, Trieste, Italy*, 2004. 27

[35] V. Ptitsyn et al. Rhic performance as polarized proton collider in run-6. *2006 European Particle Accelerator Conference proceedings, Edinburgh, Scotland*, 2006. 27, 47

[36] C. Montag et al. Rhic polarized proton performance in run-8. *2008 European Particle Accelerator Conference proceedings, Genoa, Italy*, 2008. 27

[37] A. Zelensky et al. On optically-pumped polarized h- ion source for rhic spin physics. *Review of Scientific Instrumetation*, 73:888–891, 2002. 27

[38] Y. S. Derbenev et al. Radiative polarization: obtaining, control, using. *Particle Acceleration*, 8:115–126, 1978. 29

[39] T. Roser. Properties of partially excited siberian snakes. *AIP conference proceedings*, 187:1442–1446, 1989. 29

[40] A. Zelensky et al. Absolute polarized h-jet polarimeter development for rhic. *Nuclear instruments and methods A*, 536:248–254, 2005. 29

[41] H. Okada et al. Measurement of the analyzing power a_n in pp elastic scattering in the cni region with a polarized atomic hydrogen gas jet target. *Physics letters B*, 638:450, 2006. 30

[42] K. H. Ackermann et al. Star detector overview. *Nuclear instruments and methods A*, 499:624–632, 2003. 31

[43] H. S. Matis et al. Integration and conventional systems at star. *Nuclear instruments and methods A*, 499:802–813, 2003. 31

[44] F. Bergsma et al. The star detector magnet subsystem. *Nuclear instruments and methods A*, 499:633–639, 2003. 33

[45] A. Drees and Z. Xu. Results from luminosity scans during the rhic 2000 run. In *Presented at IEEE Particle Accelerator Conference*, 2001. 35

[46] T. Sjostrand and P.Eden et al. High-energy-physics event generation with pythia 6.1. *Computer physics communications*, 135(2):238–259, 2001. 35, 53

[47] CERN. *Geant manual*. wwwinfo.web.cern.ch/wwwinfo/asd/geant/, 2010. 35, 53

[48] Y. Wang. *Measurement of inclusive forward neutral pion production in 200GeV polarized proton-proton collisions at RHIC*. PhD thesis, University of Texas, Austin, 2004. 59, 80

[49] C. Bourelly and J. Soffer. Do we understand the single-spin asymmetry for π^0 inclusive production in pp collisions? *European physics journal C*, 36:371–374, 2004. 84

[50] J. Adams et al. Cross sections and transverse single-spin asymmetries in forward neutral pion production from proton collisions at $\sqrt{s}$= 200 gev. *Physical review letters*, 92:171801, 2004. 84, 141

[51] RHIC. *http://www4.rcf.bnl.gov/ cnipol/*. pcCNI polarimetry group, 2007. 100

[52] N. Poljak for the STAR collaboration. Spin-dependent forward particle correlations in p+p collisions at $\sqrt{s}$= 200 gev. *SPIN08 conference proceedings*, 2009. 110, 121, 130, 131, 132, 146

[53] M. Anselmino et al. Transversity and collins functions from sidis and e+e- data. *Physical review D*, 75:054032, 2007. 140

[54] Y.-S. Tsai. Pair production and bremsstrahlung of charged leptons. *Review of modern physics*, 46:815–845, 1974. 149

[55] M.J. Berger and S.M.Seltzer. Tables of energy losses and ranges of electrons and positrons. *National Aeronautics and Space Administration Report NASA-SP-3012*, 1964. 150

[56] B. Rossi. *High energy particles*. Prentice-Hall Inc, NJ., 1952. 150